An Improved Understanding of Aerosol Processes using Satellite Observations of Aerosol Optical Properties

Claire E. Bulgin

A thesis submitted for the degree of Doctor of Philosophy
The University of Edinburgh

October, 2010

Declaration

This thesis is an account of research undertaken between October 2006 and May 2010 in The School of Geosciences at The University of Edinburgh, Edinburgh, Scotland, United Kingdom. Except where explicitly stated, this thesis and the material presented in it is my own work and has not been submitted in whole or part for a degree in any university.

Claire E. Bulgin
October, 2010

Acknowledgements

There are a number of people who have played key roles in supporting me as I completed the research presented in this thesis. Firstly I would like to thank my supervisors Paul Palmer, Chris Merchant and Richard Siddans for their advice and help particularly during the early stages of my research. I would also like to thank Paul who read and re-read numerous versions of my thesis before submission, providing many useful comments on its content and structure. I also thank my dad, Denis Bulgin, for proof reading the entire thesis often over short time scales, for persevering with a subject in which he has little interest, and for providing comments under surreal circumstances including over the phone with poor signal at the bottom of a munro! I would also like to thank my examiners David Stevenson and Helen Brindley for the time they spent reading my thesis and their insightful comments.

Most of all I thank God for the opportunity He gave me to do this PhD, for the people He put in place to support me in Edinburgh, and for all of the things that he taught me along the way. I thank my friends Niki Martin and Claire Peacock and others at MBC for all their prayer and support especially during the final stages of my write up when I spent every waking hour working on my thesis!

Abstract

Atmospheric aerosols are the largest remaining uncertainty in the Earth's radiative budget and it is important that we improve our knowledge of aerosol processes if we are to understand current radiative forcing and accurately project changes in future climate. Aerosols affect the radiation balance directly through the absorption and scattering of incoming solar radiation and indirectly through the modification of cloud microphysical properties. Understanding aerosol forcing remains challenging due to the short atmospheric residence time of aerosols resulting in large spatial and temporal heterogeneity in aerosol loading and chemical composition. Satellite retrievals are becoming increasingly important to improving our knowledge of aerosol forcing. They provide regular global data at finer spatial and temporal resolution than available through sparse ground-based point measurements or localised aircraft campaigns, but cannot unambiguously determine aerosol speciation, relying heavily on *a priori* assumptions. In this thesis I use data from two satellite instruments: the Along Track Scanning Radiometer 2 (ATSR-2) and the Spinning Enhanced Visible and InfraRed Imager (SEVIRI) interpreted using the Oxford-RAL Aerosol and Cloud (ORAC) retrieval scheme in three pieces of interrelated work.

First I use satellite observations of aerosol optical depth τ_a and cloud particle effective radius r_e from the ATSR-2 instrument in 1997 to investigate the Twomey indirect effect (IE, -∂ ln r_e /∂ ln τ_a) in regions of continental outflow. I generally find a negative correlation between τ_a and r_e with the strongest inverse relationships downwind of Africa. North America and eastern Asian continental outflow exhibits a strong seasonal dependence, as expected. Global values for IE range from 0.10 to 0.16, consistent with theoretical predictions. Downwind of Africa, I find that the IE is unphysically high but robust ($r = -0.85$) during JJA associated with high aerosol loading, and attribute this tentatively to the Twomey hypothesis accounting only for a limited number of physical properties of aerosols.

Second, I test the response of the Oxford-RAL Aerosol and Cloud (ORAC) retrieval algorithm for MSG SEVIRI to changes in the aerosol properties used in the dust aerosol model, using data

from the Dust Outflow and Deposition to the Ocean (DODO) flight campaign in August 2006. I find that using the observed DODO free tropospheric aerosol size distribution and refractive index compared with the dust aerosol properties from the Optical Properties of Aerosol and Cloud (OPAC) package, increases simulated top of the atmosphere radiance at 0.55 μm assuming a fixed aerosol optical depth of 0.5, by 10–15%, reaching a maximum difference at low solar zenith angles. This difference is sensitive to changes in AOD, increasing by $\sim$2–4% between AOD of 0.4–0.6. I test the sensitivity of the retrieval to the vertical distribution of the aerosol and find that this is unimportant in determining simulated radiance at 0.55 μm. I also test the ability of the ORAC retrieval when used to produce the GlobAerosol dataset to correctly identify continental aerosol outflow from the African continent and I find that it poorly constrains aerosol speciation. I develop spatially and temporally resolved prior distributions of aerosols to inform the retrieval which incorporates five aerosol models: desert dust, maritime, biomass burning, urban and continental. I use a Saharan Dust Index and the GEOS-Chem chemistry transport model to describe dust and biomass burning aerosol outflow, and compare AOD using my speciation against the GlobAerosol retrieval during January and July 2006. I find AOD discrepancies of 0.2–1 over regions of biomass burning outflow, where AOD from my aerosol speciation and the GlobAerosol speciation can differ by as much as 50 - 70 %.

Finally I use satellite observations of aerosol optical depth and cloud fraction from the MSG SEVIRI instrument to investigate the semi-direct effect of Saharan dust aerosol on marine stratocumulus cloud cover over the Atlantic during July 2006. I first use these data to study the spatial autocorrelation of aerosol optical depth and find that it is correlated over a lag of 0.1° (approximately 10 km at low latitudes), beyond which it rapidly decorrelates. I find a 15 % higher cloud fraction in regions with high dust loading (AOD $>$ 0.5), compared with scenes with a lower dust loading (AOD $<$ 0.5), which for high dust scenes increases with local static stability. I attribute this tentatively to aerosol solar shielding enhancing longwave cloud top radiative cooling which drives marine stratocumulus convection.

Glossary of Terms

Aerosol: Airborne atmospheric particles released either directly through primary emission from both natural and anthropogenic sources, or generated through secondary chemical formation pathways.

Aerosol Optical Depth (τ_a, AOD): A measure of light extinction caused by aerosols via scattering and absorption of radiation. Often used as a proxy for aerosol amount in studies using satellite data. Aerosol optical depth can be expressed as:

$$\tau_a = \int_0^\infty K dz \tag{1}$$

where K is the extinction coefficient and dz the length of the atmospheric pathway. τ_a at the top of the atmosphere is zero, increasing towards the Earth's surface.

A priori: A 'first or best guess' dataset used to describe the state of a system or system component for modelling purposes.

Cloud Effective Radius (r_e. CER): Weighted mean cloud droplet effective radius calculated using:

$$r_e = \frac{\int_0^\infty r^3 n(r) dr}{\int_0^\infty r^2 n(r) dr} \tag{2}$$

where r = particle radius, and n(r) = particle size distribution.

Extinction coefficient, K: A measure of total column light extinction (K) caused by aerosol scattering (K_a) or absorption (K_s).

$$K = K_a + K_s \tag{3}$$

Forward model (F): Model of atmospheric radiative transfer used to simulate satellite radiance observations.

Radiance, L: Signal measured by satellite instruments, comprised of reflected and scattered solar radiation and longwave thermal radiation. Radiant flux (L) is measured in $Wm^{-2}sr^{-1}$ and can be defined as:

$$L = \frac{dF}{cos\theta d\omega} \tag{4}$$

where dω is a solid angle θ the angle to the surface and F the radiant flux density.

Scattering angle, θ_s: The angle between the direction of incident radiation and the detector in relation to the scatterer defined as:

$$\theta_s = \theta_i + \theta_r \tag{5}$$

where θ_s is the scattering angle, θ_i the incident angle of the radiance and θ_r is the reflection angle of the radiance.

Contents

List of Figures

List of Tables

Chapter 1

Introduction

Atmospheric aerosols are the largest remaining uncertainty in the Earth's radiative budget [Forster et al., 2007]. They impact the radiation balance directly by scattering and absorbing both long and shortwave radiation, and indirectly by altering the radiative properties of clouds. Our understanding of aerosol forcing and processes remains incomplete due to the challenge of studying atmospheric aerosols which exhibit short atmospheric lifetimes and a large range of sources resulting in significant spatial and temporal heterogeneity in loading and chemical composition. The issue is further compounded by numerous meteorological regimes across the globe making classification of aerosol cloud interaction a non-trivial problem.

Aerosol science is a rapidly expanding field of research motivated by the need to close the radiative budget when modelling the Earth system, which is becoming increasingly important as we try to predict future climate response to anthropogenically induced climate forcing, through greenhouse gas and aerosol emissions. Global warming is occurring primarily through the water vapour feedback stimulated by the absorption of incoming solar radiation by greenhouse gases from anthropogenic emissions eg. CO_2, CH_4, emitted by the domestic, industrial and transport sectors. The key role of aerosols means that modelling future climate response to anthropogenic perturbation requires a comprehensive understanding of microphysical aerosol processes. This is critical to making an accurate representation of the effect of both natural and anthropogenic aerosol on radiation in global models, unable to resolve processes at these scales. Remote sensing is the key link in this process, allowing us to apply our knowledge of aerosols and aerosol-cloud interaction observed through ground-based networks and intensive aircraft campaigns to aerosol forcing on the global scale.

Satellite remote sensing, although advantageous in its ability to provide global data on relatively

short temporal scales, is unable to fully constrain aerosol type and relies heavily on *a priori* assumptions. In this thesis I focus on data derived using the Oxford-RAL Aerosol and Cloud (ORAC) optimal estimation retrieval scheme, applied to retrievals from two satellite instruments: the Along-Track Scanning Radiometer (ATSR-2) and the Spinning Enhanced Visible and Infrared Imager (SEVIRI). I test the ability of the retrieval used first with ATSR-2 data to reproduce observations of aerosol-cloud interactions observed by instruments on other platforms (chapter 2). I then focus on aerosol outflow from the African continent, mainly consisting of dust from the Saharan desert and biomass burning emissions. I use SEVIRI, providing data at higher temporal resolution than ATSR-2 in this region. I test the sensitivity of the retrieval to changes in *a priori* aerosol assumptions (chapter 3), and to investigate the effect of Saharan dust aerosol on cloud cover over the tropical Atlantic (chapter 4).

In the remainder of this chapter I give a general introduction to aerosols, radiative forcing and aerosol-cloud interaction as well as an overview of the current research methods used to study aerosols. I also give an overview of the data, methods and tools used in this thesis and outline the work undertaken which is presented in the format of three journal articles in chapters two to four. In chapter five I draw together the outcomes of the three interrelated pieces of research and present my conclusions.

1.1 What are aerosols?

Atmospheric aerosols are defined as any liquid or solid particle held in suspension within the atmosphere. Aerosols have a range of sources both natural and anthropogenic including wind blown desert dust, sea salt, biomass burning and industrial emissions. Aerosol chemical composition is source dependent. Some aerosols are naturally absorbing for example biomass burning or industrial emissions containing black carbon, whilst others are more effective at scattering radiation including dust and sulphates. Aerosols are classified in three modes: nucleation, accumulation and coarse mode, although in satellite retrieval schemes, the focus of much of the work in this thesis, they are often divided into only two classes: fine or coarse mode aerosol with a class boundary at 2.5 μm radius. As aerosols age, their chemical composition and size distribution changes as large

particles are deposited through gravitational settling and smaller particles coagulate.

1.2 Why study aerosols?

Aerosols have been the topic of extensive research since the 1950s. Aerosols have a direct impact on the Earth's radiative budget, causing light attenuation through absorption and scattering of incoming solar radiation at ultra violet and visible wavelengths and outgoing terrestrial radiation in the infrared. Aerosols also have an indirect impact on the radiation budget, interacting with clouds and modifying their radiative properties [Twomey, 1974; Albrecht, 1989]. Aerosol effects on the radiation budget are dependent on local aerosol loading, chemical composition and meteorology making it difficult to extrapolate results from localised studies to other geographical regions. Only recently with the development of satellite technology and climate models and our ability to identify causes of discrepancies between the two has the task of quantifying global aerosol forcing become possible [Myhre, 2009]. Aerosol radiative forcing as defined with the IPCC figures discussed below refers to perturbations in the Earth's equilibrium temperature caused by changes in anthropogenic aerosol emissions since 1750. The term aerosol radiative forcing is used more widely in this thesis to describe the difference between the forcing from a given aerosol component and the comparative forcing in the absence of that component. The various definitions and components of aerosol radiative forcing are discussed in more detail in section 1.4.

The first aerosol research was prompted following the industrial revolution which saw a dramatic increase in fossil fuel combustion within the domestic, transport and industrial sectors causing dense winter smog in urban areas. A severe smog event in London during December 1952 associated with many deaths from cardiovascular and respiratory disease resulted in the UK Clean Air Act which came into force in 1956 [Seaton et al., 1995]. Inhalation of airborne particles can cause respiratory distress and absorption of these particles into the blood stream can result in cardiovascular complications. Health implications are dependent on atmospheric particle concentration, particle size, chemical composition and exposure time. The reader is referred to Pope III and Dockery [2006] for a detailed review of aerosol health effects as they are not the focus of this research. Smog events also indicated that aerosols can significantly reduce visibility by increasing

the extinction of light between the observer and the observed object [Horvath, 1981]. Visibility can change as a function of both atmospheric aerosol loading and relative humidity which dictates particle size [Doyle and Dorling, 2002].

More recently research into the climatic impact of aerosols has become more important. Net aerosol radiative forcing from changes in anthropogenic aerosol emissions since 1750 is negative [Forster et al., 2007] and some research has suggested that this atmospheric cooling is presently compensating in part for the warming induced by greenhouse gases and may continue to do so in the "short term" [Wigley, 1991; Andreae et al., 2005], a period of time that will be determined by future emissions. Future temperature increase can be calculated using the concept of climate sensitivity – the equilibrium temperature response of the atmosphere to a doubling of CO_2 concentrations, and this will be dependent on atmospheric composition and climate feedbacks [Andreae et al., 2005; Raynaud et al., 1993]. Reductions in fossil fuel emissions could rapidly change the ratio of aerosol to greenhouse gas concentrations due to the significantly shorter atmospheric lifetime of aerosol in comparison with greenhouse gas species. In this situation climate sensitivity may be higher than our current estimates [Andreae et al., 2005]. Further related to this discussion is the concept of "tipping points" in the climate system where large scale elements of the earth system reach the point where changes are irreversible, for example melting of the Arctic, Greenland or West Antarctic ice sheets, which may have significant and potentially abrupt impacts on future climate [Lenton et al., 2008]. Further work is needed to identify these points, and establish an early warning system. For this it is critical that we understand aerosol forcing and are able to determine climate response to changes in aerosol loading or transport resulting from future emission reductions or climate feedbacks.

Aerosols have also been proposed as a possible geoengineering solution to global warming. One suggestion is to force the climate by injecting sulphate aerosol into the stratosphere [Crutzen, 2006; Wigley, 2006], which will increase the Earth's albedo and reflect incoming solar radiation in a similar way to that observed following the major eruption of Mount Pinatubo in 1991 [Parker et al., 1996; Stowe et al., 1992]. A second suggestion is to increase cloud albedo by injecting aerosol particles into the marine boundary layer where they can act as cloud condensation nuclei (section 1.4.2) [Latham et al., 2008; Salter et al., 2008]. Despite the significant gaps in our

understanding of aerosol impacts on climate [Forster et al., 2007] these proposals have sparked extensive discussion on their feasibility, risk assessment and the vulnerability of the earth system [Brovkin et al., 2009; Shepherd, 2009]. At present both aerosol "solutions" to the climate warming problem have significant safety concerns in connection with the potential feedbacks on regional climate. Geoengineering poses a complex interdisciplinary problem which will require some element of unanimity in relation to global politics, economics, science and technology before implementation [Keith, 2000] and cannot be undertaken until we more fully understand aerosol climate forcing.

1.3 Scientific Background

1.3.1 Aerosol Properties

Aerosol sources can be natural or anthropogenic including both primary particles, and atmospheric gases (eg. volatile organic compounds (VOCs)) which can generate aerosol through secondary processes. Primary particles are predominantly mechanically produced through the action of wind, waves, volcanic eruptions or from biogenic sources, and larger in size than secondary particles which tend to have a chemical origin [Buseck and Pósfai, 1999]. Table 1.1 (adapted from Seinfeld and Pandis [2006]) gives a summary of different aerosol sources estimated from a number of modelling studies. The single largest aerosol source is sea salt [Gong et al., 2002] with an estimated flux of 10,100 Tg yr^{-1}, followed by desert dust with an estimated total flux across all size bins (0.1 - 10 μm) of 1490 +/- 160 Tg yr^{-1} [Zender et al., 2003]. Natural aerosol fluxes are estimated at 11,693 Tg yr^{-1} which far outweigh the anthropogenic flux estimates of 262.9 Tg yr^{-1}. Despite contributing only a small fraction of the total global aerosol load, anthropogenic aerosol is important as it represents an external forcing on the natural climate system (discussed in section 1.4).

Aerosol chemical composition is important in determining aerosol radiative forcing. Figure 1.1, gives a breakdown of aerosol forcing from changes in anthropogenic emissions since 1750 by aerosol type [Forster et al., 2007]. Sea salt, the most significant aerosol source by mass, is predominantly scattering but also provides a large surface area for heterogeneous chemical reactions [Buseck and Pósfai, 1999]. Over the oceans dimethyl sulphide emitted by phytoplankton forms

Table 1.1: Global Emission Estimates for Major Aerosol Classes [Seinfeld and Pandis, 2006]

Source	Estimated Flux (Tg yr^{-1})[d]	Reference
Natural		
Primary		
Mineral Dust		Zender et al. [2003]
0.1 - 1.0 μm	48	
1.0 - 2.5 μm	260	
2.5 - 5.0 μm	609	
5.0 - 10.00 μm	573	
0.1 - 10.00 μm	1490 +/- 160	
Seasalt	10,100	Gong et al. [2002]
Volcanic Dust	30	Kiehl and Rodhe [1995]
Biological Debris	50	Kiehl and Rodhe [1995]
Secondary		
Sulfates from DMS	12.4	Liao et al. [2003]
Sulfates from volcanic SO_2	20	Kiehl and Rodhe [1995]
Organic aerosol from biogenic VOC	11.2	Chung and Seinfeld [2002]
Anthropogenic		
Primary		
Industrial dust (except black carbon)	100	Kiehl and Rodhe [1995]
Black Carbon	12[a]	Liousse et al. [1996]
Organic aerosol	81[a]	Liousse et al. [1996]
Secondary		
Sulfates from SO_2	48.6[b]	Liao et al. [2003]
Nitrates from NO_x	21.3[c]	Liao et al. [2003]

[a] Tg C.
[b] Tg S.
[c] Tg NO_3^-
[d] Most estimates are model means not reported with error bounds.

non-sea salt sulphate and methane sulphonate aerosol, and these particles act as the primary cloud condensation nuclei (CCN) [Charlson et al., 1987] important in terms of aerosol-cloud interactions. Dust aerosol particle size is often similar to the wavelength of incoming solar radiation and it can have a dual radiative effect both absorbing and scattering radiation [Buseck and Pósfai, 1999] although the net forcing is thought to be negative [Boucher et al., 2001]. Black carbon emitted from anthropogenic sources of incomplete combustion in the transport, industrial and domestic sectors and also from biomass burning is the most absorbing atmospheric aerosol, with a positive radiative forcing particularly over land surfaces with a high albedo [Forster et al., 2007]. Black carbon from fire emissions also readily acts as CCN leading to indirect aerosol forcing [Kaufman and Fraser, 1997] (discussed in section 1.4.2).

The diverse range of aerosol sources means that different aerosol types often become mixed during atmospheric transport. Any given aerosol 'type' will consist of a number of aerosol components, for example biomass burning emissions are a mixture of black carbon, plant fibres, soil dust, ash, organics and inorganic species [Jacobson, 2005]. Secondary organic aerosol can form through many chemical pathways, creating new particles or condensing onto pre-existing primary particles. At present, these formation pathways are not well characterised given their sheer number but are important in determining aerosol forcing and aerosol-cloud interaction [Hallquist et al., 2009; Fuzzi et al., 2006]. Mixing within an aerosol 'type' and between aerosols from different sources can either be external where the different aerosol components are mixed spatially but not within each particle, or internal where the aerosols react chemically to produce particles that include a number of different aerosol components. Mixing type influences the aerosol size distribution, chemical reactivity, and ability of the aerosol to act as CCN [Lesins et al., 2002], which is fundamental to determining aerosol radiative forcing. Negative aerosol radiative forcing is predicted as more likely in external than internal mixtures at all relative humidities [Lesins et al., 2002].

Despite the importance of aerosol chemical composition in determining the overall sign of the radiative forcing, research focused on a particular aerosol type has concluded that within these types, aerosol size accounts for 84 - 96 % of the variation in CCN concentration [Dusek et al., 2006]. Aerosol particles cover a large size range, from a few nanometres to tens of microns depending on emission sources and chemical processes. Critical supersaturation of aerosol particles,

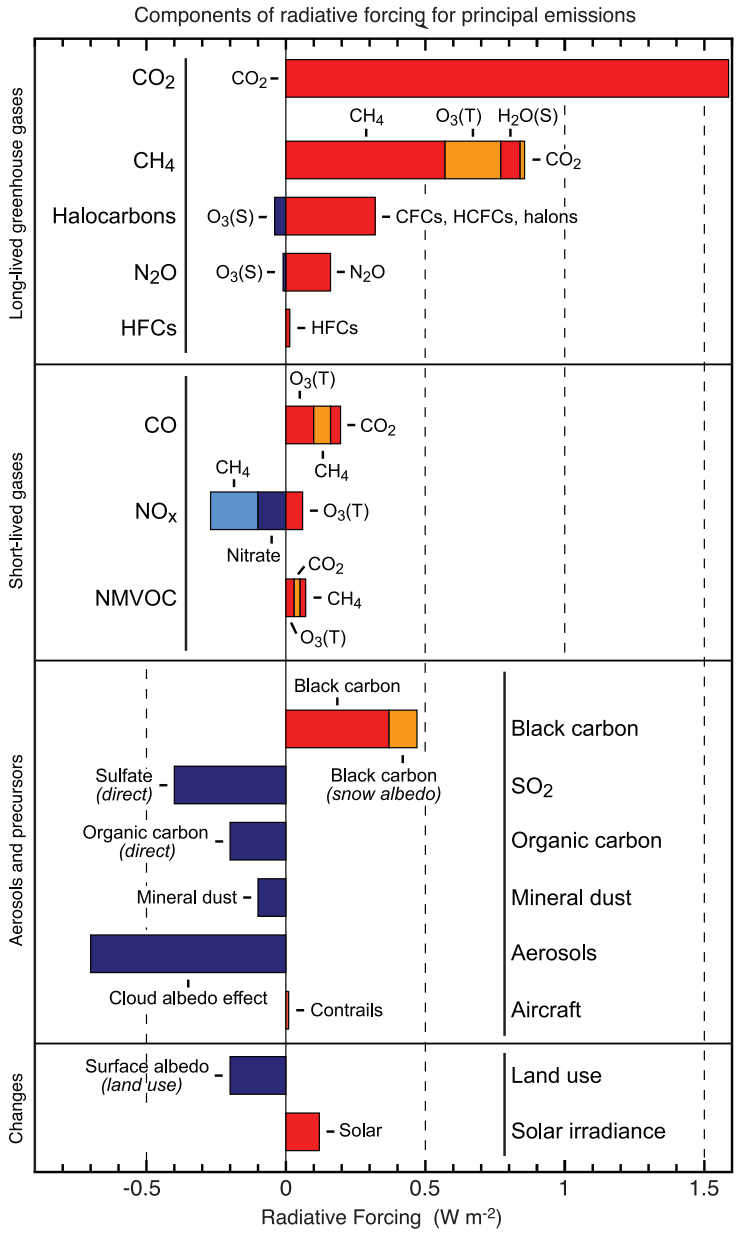

Figure 1.1: Components of radiative forcing for emissions of principal gases, aerosols and aerosol precursors and other changes. Values represent radiative forcing in 2005 due to emissions and changes since 1750. (S) and (T) next to gas species represent stratospheric and tropospheric changes, respectively [Forster et al., 2007].

which governs their ability to act as CCN, is linearly related to the soluble mass fraction determined by chemical composition, but related by the third power to the electrical mobility diameter governed by particle size [Dusek et al., 2006; Hudson, 2007]. This relationship may be less useful in insoluble particles where the addition of small amounts of soluble material significantly affects the critical supersaturation [Dusek et al., 2006], and some characterisation of the relation-

ship between mean dry particle size of different aerosol types and critical supersaturation may be necessary before size alone can be used to determine CCN availability [Hudson, 2007]. Typically when discussing atmospheric processes particles are split into the fine or coarse mode with a threshold diameter of 2.5 μm. The primary deposition mechanism for coarse mode particles is gravitational settling and for fine mode particles rain or wash out through interaction with clouds.

1.4 Radiative Effects of Atmospheric Aerosols

Figure 1.2 shows a summary of the different radiative forcing components from the fourth IPCC assessment report. Aerosol radiative forcing as defined here refers to changes in the radiation budget induced by differences in anthropogenic aerosol emissions between 1750 and the present day. The IPCC identify anthropogenic aerosols as the largest remaining uncertainty in the radiation budget, contrasting our relatively comprehensive knowledge of greenhouse gas induced warming against the poorly understood aerosol forcing. Net anthropogenic aerosol radiative forcing is thought to be negative (a cooling), split between the direct effects (scattering and absorption of solar and terrestrial radiation) accounting for a cooling of -0.5 W m^{-2}, and indirect effects (aerosol modification of cloud properties) accounting for a cooling of -0.8 W m^{-2}. At present, the associated uncertainty in these values is substantial, as large as the magnitude of the forcing, with direct aerosol forcing estimates ranging between -0.1 and -0.9 W m^{-2}, and indirect forcing estimates between -0.5 and -1.8 W m^{-2}. Aerosol direct (section 1.4.1), indirect (section 1.4.2) and semi-direct (section 1.4.3) effects are discussed in detail below and shown schematically in Figure 1.3. Figure 1.2b shows the radiative forcing probability distribution for three cases: a) aerosol only, b) greenhouse gas only and c) total anthropogenic combining aerosol and greenhouse gas forcing. This indicates that given our current understanding of the radiative forcing components, net anthropogenic forcing is thought to be positive with the majority of estimates falling within the range of 0.5-2.5 Wm^{-2}. As explained above the term aerosol radiative forcing within the context of the IPCC report refers only to changes in radiation budget induced by anthropogenic aerosol emissions since 1750. However, all aerosol, both natural and anthropogenic, interacts with incoming and outgoing radiation through the same mechanisms as those described below. The focus of the work is on desert dust and biomass burning emissions from the African continent which are

only in part anthropogenic from land use change and fires. In this thesis the term radiative forcing is therefore applied to the theoretical situation describing the difference between the forcing induced by a given aerosol component and the forcing in the absence of that component. This enables us to understand the radiative effect of natural aerosol to more accurately model aerosol processes in climate simulations.

1.4.1 Direct Radiative Forcing

Direct aerosol forcing is the scattering or absorption of incoming solar or outgoing terrestrial radiation, by aerosol perturbing radiative energy transfer through the atmosphere. This can be measured either at the Earth's surface or at the top of the atmosphere (TOA) [Pilewskie, 2007]. Predominantly scattering aerosol, for example sulphate species, will give similar TOA and surface forcing whilst absorbing aerosol, for example black carbon, will induce local atmospheric warming resulting in different surface and TOA forcing [Seinfeld and Pandis, 1998]. Large-scale direct aerosol forcing was observed following the eruption of Mount Pinatubo in 1991, where injection of sulphur dioxide into the stratosphere generated 30 Tg of sulphate aerosol [McCormick et al., 1995]. The aerosol was transported across a significant portion of the globe over a period of several months, increasing the Earth's albedo [McCormick et al., 1995] and reducing surface temperature by ~ 0.5 K [Parker et al., 1996]. Aerosol in the stratosphere has a much longer residence time than in the troposphere and changes in surface temperature were recorded for two years after the eruption [Parker et al., 1996]. Whether an aerosol is predominantly scattering or absorbing is dependent on aerosol size, chemical composition, shape and the observation wavelength [Collaud Coen et al., 2004] as discussed in detail in section 1.3.1.

1.4.2 Indirect Radiative Forcing

Indirect aerosol forcing in warm clouds occurs through aerosol modification of cloud microphysical properties and is explained schematically in Figure 1.3. Twomey [1974] first proposed this idea, speculating that as aerosols act as CCN around which cloud droplets form, increasing aerosol concentrations would increase cloud droplet number. Making the assumption that there was no change in the liquid water content of the cloud, these droplets would be smaller in size, increasing

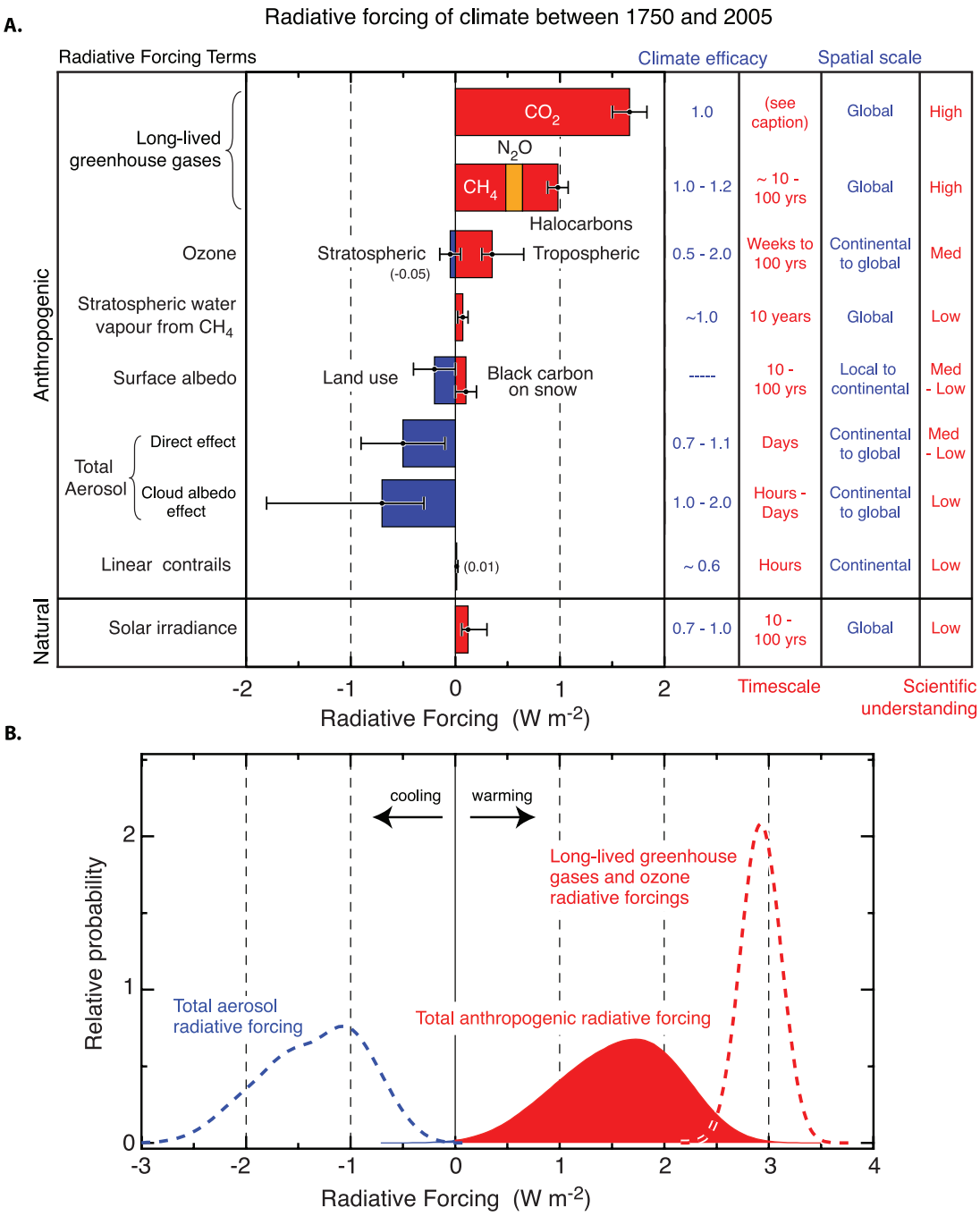

Figure 1.2: (A) Global mean radiative forcing by agent. Time scales represent the length of time that a given radiative forcing term would persist in the atmosphere after the associated emissions ceased. No CO_2 timescale is given, as its removal from the atmosphere involves a range of processes that can span long time scales, and thus cannot be expressed accurately with a narrow range of lifetime values. (B) Probability distribution functions from combining anthropogenic radiative forcing components in (A). Three cases are shown: the total of all anthropogenic radiative forcing terms (block filled red curve), long lived greenhouse gases and ozone radiative forcings only (dashed red curve); and aerosol direct and cloud albedo radiative forcings only (dashed blue curve) [Forster et al., 2007].

cloud albedo. This is now commonly referred to as the first aerosol indirect effect. This relationship between aerosol concentration and cloud albedo is non-linear as increased particle number tends to lower the maximum relative humidity, giving a dependence of albedo (A) on aerosol concentration (n) of $A \propto n^{0.8}$ [Twomey, 1974]. This may also be offset by the aerosol dispersion effect; increased aerosol droplets reduce cloud supersaturation which increases competition for water droplets and broadens the cloud droplet size distribution at the lower end [Liu and Daum, 2002].

The second indirect effect was proposed by Albrecht [1989] and is an extension of the first. Increasing cloud droplet number, reducing cloud droplet size can result in a reduction of drizzle production through collision-coalescence, prolonging cloud lifetime and increasing cloud radiative forcing [Albrecht et al., 1995b]. Indirect aerosol forcing is particularly important in marine stratocumulus clouds as they cover one third of the world's oceans [Ackerman et al., 2000b]. This type of cloud typically has an albedo of 30-40 % in contrast with the $\sim$ 10 % albedo of the underlying ocean [Albrecht et al., 1995b]. The second indirect effect is not included in the anthropogenic forcing shown in the IPCC Figure 1.2 as the radiative forcing occurs as a result of changes in the hydrological cycle and climate feedbacks [Forster et al., 2007].

The discussion so far has focused on aerosol effects in warm clouds. Aerosol can also be important in ice clouds for example in the formation of contrails from aircraft exhaust emissions [Schröder et al., 2000]. In this case the Twomey effect works in the same way as in water clouds as aerosols act as ice nuclei (IN) [Boucher, 1999]. A change in the ice water content of cirrus cloud could also have a radiative impact in the infrared [Lohmann and Feichter, 2005], although research in this area is limited.

1.4.3 Semi-Direct Effects

The semi-direct effect, a mechanism by which aerosol may reduce cloud cover was first suggested by Ackerman et al. [2000a]. In stratocumulus cloud decks, convection is maintained by cloud top radiative cooling. Absorbing aerosols can warm the atmosphere locally preventing radiative cooling and decreasing relative humidity. Both of these mechanisms result in a reduction in cloud

cover [Ackerman et al., 2000a]. This effect is distinct from the aerosol indirect effects and not included in the radiative forcing component diagram (Figure 1.2) for the same reasons as the second indirect effect. Modelling studies excluding indirect forcing have shown this effect to be comparable to direct aerosol forcing [Johnson et al., 2004].

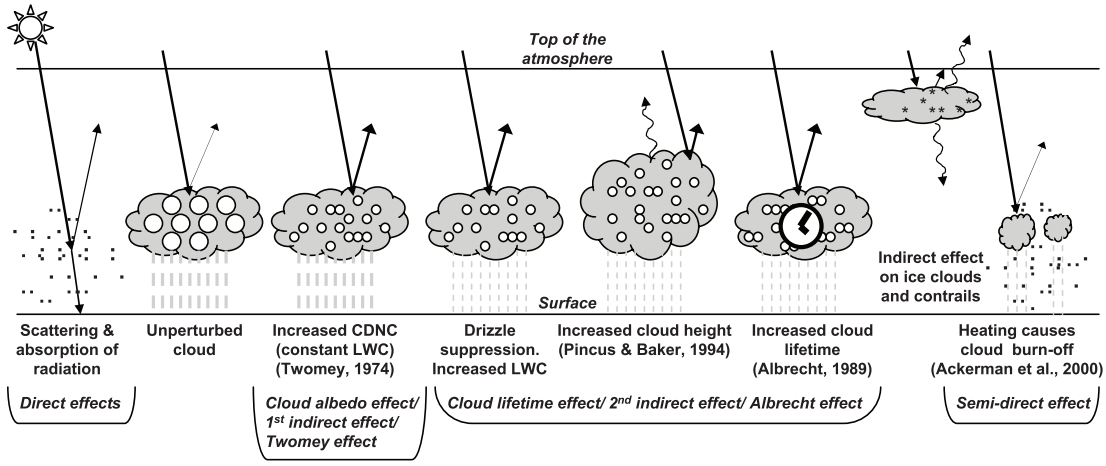

Figure 1.3: Schematic diagram showing the various radiative mechanisms associated with cloud effects that have been identified as significant in relation to aerosols. The small black dots represent aerosol particles; the larger open circles cloud droplets. Straight lines represent the incident and reflected solar radiation, and wavy lines represent terrestrial radiation. The filled white circles indicate cloud droplet number concentration. The unperturbed cloud contains larger cloud drops as only natural aerosol are available as CCN, while the perturbed cloud contains a greater number of smaller cloud drops as both natural and anthropogenic aerosols are available as CCN. The vertical grey dashes represent rainfall, and LWC refers to the liquid water content [Forster et al., 2007].

When discussing aerosol radiative forcing it is important to consider the relative aerosol and cloud altitude, dependent on aerosol injection height and local meteorology. The Twomey and Albrecht effects modifying cloud microphysics will occur only where cloud and aerosols are co-located. Aerosols located above cloud may exert direct or semi-direct radiative forcing perturbing the atmospheric circulation and the hydrological cycle redistributing clouds and precipitation [Takemura et al., 2007]. Local atmospheric conditions will also determine cloud feedback in response to the Albrecht effect. Precipitation suppression can result in enhanced air entrainment above the cloud. If this air is dry it will decrease the liquid water content of the cloud, thus reducing its indirect forcing Ackerman et al. [2000a]. This highlights the importance of studying aerosol forcing of different aerosol types under different meteorological regimes to be able to quantify global aerosol forcing.

1.5 Research Methods

Aerosol radiative forcing is estimated using measurements of aerosol optical properties. The most commonly used parameter is the aerosol optical depth (AOD), a measure of column light extinction attributed to aerosols (occurring through either scattering or absorption), which can be used as a proxy for aerosol abundance. Other optical properties include aerosol effective radius, refractive index and the aerosol phase function which may be measured directly or calculated using code describing aerosol scattering. Mie code is often used for this purpose, describing the scattering properties of particles in the Mie regime, of a similar diameter to the wavelength of incident radiation. Mie scattering is based on the assumption that the aerosol particles are spherical and this may not be the best approximation for some aerosol types, particularly dust. This topic is discussed in more detail in Chapter 3 (section 3.4.2).

There are four widely used platforms for studying atmospheric aerosol: ground-based networks, aircraft campaigns, satellite observation and climate and/or chemistry transport models. These cover different spatial scales and can be used individually or as complementary resources. Below I give a brief introduction to each research platform before giving a more detailed description of the data and tools that I use. Throughout this thesis I make extensive use of satellite, aircraft and chemistry transport model data. These data are also described more briefly in each results chapter (2–4) alongside each individual piece of research for clarity.

1.5.1 Ground-Based Measurements

Ground-based measurements of atmospheric aerosols can give detailed long-term records of aerosol loading, size distribution and chemical composition at a given location. These records can be used to determine long-term changes in local direct radiative forcing. Conversely, these records are localised and sparse in global terms and may not be representative of the wider spatial domain in which they are located, making them difficult to scale up to determine regional and global forcing. Aerosol measurements are also only possible in the absence of cloud cover.

The most extensive ground-based aerosol observation network is the AErosol RObotic NETwork (AERONET) which was initially established by NASA as part of PHOTONS in 1996 [Smirnov et al., 2009] and then extended across the globe by other collaborators [NASA, 2009]. This is a network of sun photometers distributed across 400 continental sites [NASA, 2010] measuring AOD, precipitable water and inversion products including aerosol size distribution, and the percentage of spherical particles [NASA, 2008]. Direct sun measurements are made in eight channels: 340, 380, 440, 500, 670, 870, 940 and 1020 nm, to determine aerosol optical properties [NASA, 2007]. These ground-based data are heavily weighted towards continental regions although some information is collected from remote oceanic regions using sensors aboard ships [Smirnov et al., 2009]. The global distribution of AERONET sites is shown in Figure 1.4.

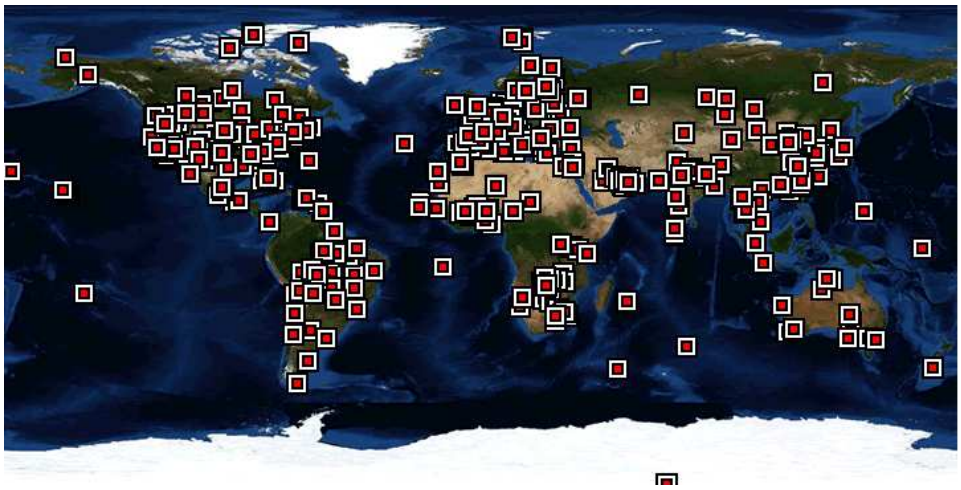

Figure 1.4: Global distribution of AERosol RObotic NETwork ground-based observation sites in May 2010 [Giles and Holben, 2010].

1.5.2 Aircraft Campaigns

There have been a number of recent campaigns in which aircraft data on aerosol and cloud optical properties have been collected and used in conjunction with satellite data, ground-based observations and global models to characterise aerosol and cloud processes. Campaigns have been based across the globe including RICO in the Caribbean from November 2004 - January 2005 [Rauber et al., 2007], INTEX-A over North America during July and August 2004 [Singh et al., 2006] and MASE off the Californian coast in July 2005 [Lu et al., 2007].

The most significant continental aerosol outflow in terms of aerosol mass and ariel extent is seen from the African continent [Bulgin et al., 2008] and a number of campaigns have observed dust and biomass burning emissions both over the continent and the Atlantic including ASTEX in June 1992 [Albrecht et al., 1995a], DABEX in 2006 [Johnson et al., 2008] [Osborne et al., 2007], DODO in 2006 [McConnell et al., 2008] and GERBILS in June 2007 [Christopher et al., 2009]. I make extensive use of data from the Dust Outflow and Deposition to the Ocean (DODO) campaign during August in 2006 in this thesis (chapter 3). The campaign was based in Dakar, Senegal and made detailed observations of aerosol size distribution and optical properties in order to quantify seasonal deposition of iron from Saharan dust into the Atlantic ocean [McConnell et al., 2008]. I use these data to test the sensitivity of the ORAC satellite retrieval of aerosol optical depth to the *a priori* assumptions made about the aerosol size and vertical distribution. Full details of this work are given in chapter 3.

Aircraft campaigns provide a unique opportunity to study in-cloud processing of aerosols. Data can be much more closely co-located than is possible with air column observations made by either ground-based or satellite instruments, as detailed measurement of cloud properties, and aerosol both above and below cloud can be made. As with ground-based observations these measurements are very localised with observations made over several to tens of kilometres and it may be difficult to apply the findings to other aerosol types or meteorological regimes.

1.5.3 Satellite Observations

Remote sensing of cloud and aerosol properties is becoming increasingly important to aerosol research as it enables the study of aerosol distributions and aerosol-cloud interactions across the globe and is the focus of the research in this thesis. I make use of data from both the ATSR-2 instrument onboard ERS-2, a polar orbiting satellite achieving global coverage every three days, [Bulgin et al., 2008] and the SEVIRI instrument onboard MSG-2 which is in geostationary orbit centred over Africa and has a temporal resolution of fifteen minutes. In both cases the retrieved satellite radiances are interpreted using the ORAC algorithm [Thomas et al., 2005]. Details of the retrieval are given in section 1.6.3.

One major criticism of using satellite data to study aerosol indirect effects is that the spatial footprint of the observations is often quite large and aerosol and cloud retrievals are not co-incident and therefore cannot be co-located [Avey et al., 2007]. A number of approaches have been taken to address this problem, including co-locating retrievals using back trajectories [Bréon et al., 2002], using a tracer-transport model [Avey et al., 2007], or comparing long-term averages over appropriate spatial scales [Bulgin et al., 2008]. Each approach has its merits and disadvantages and a further discussion of these is undertaken in chapter 5.

1.5.4 Models

The need to accurately represent aerosol processes in both climate and chemistry transport models (CTMs) is becoming increasingly important as we use them to predict future climate under different emission scenarios. We can use them to test our understanding of atmospheric processes and to interpret observations from other platforms. We make use of the GEOS-Chem CTM driven using assimilated meteorology from the NASA Global Modelling and Assimilation Office [Le Sager et al., 2008]. When testing the sensitivity of the ORAC retrieval to aerosol *a priori* assumptions we use the model to describe biomass burning aerosol outflow from the African continent and constrain the ORAC SEVIRI retrieval in which there is at present no prior information about aerosol location (chapter 3). The biggest challenge in using CTMs to accurately model aerosol processes is the difficulty in scaling up aerosol processes at the microphysical scale to the resolution of the model, 2 x 2.5 degrees in the case of GEOS-Chem. In order to do this some parameterisation of the processes involved is necessary and there is a trade off between model detail and speed dependent on the computing facilities available.

1.6 Retrieval Schemes, Satellite Instruments and Tools

All of the work in this thesis is based on satellite data retrieved using the Oxford-RAL Aerosol and Cloud (ORAC) retrieval scheme. The individual studies are presented in the form of papers where typically only a limited description of the retrieval is given, and consequently a detailed overview

of the scheme is provided here. In chapter 2 this retrieval is used to generate the Global Retrieval of ATSR cloud Parameters and Evaluation (GRAPE) dataset, using data from the second Along Track Scanning Radiometer (ATSR-2). In chapters 3 and 4 this retrieval scheme is used to derive aerosol properties using data from the Spinning Enhanced Visible and InfraRed Imager (SEVIRI). A full description of the algorithm used with the SEVIRI instrument is given in Thomas et al. [2009a]. Here I describe the instruments, retrieval and tools used in each of the results chapters.

1.6.1 ATSR-2

ATSR-2 is aboard the second European Research Satellite (ERS-2) which is in a near-polar sun synchronous orbit with an equator overpass time of 10.30 in the descending node. It makes observations in seven spectral channels covering the visible and infrared spectrum centred at 0.55, 0.67, 0.87, 1.6, 3.7, 11 and 12 μm [Mutlow et al., 1999]. ATSR-2 is a dual view instrument making an observations at an incidence angle of 55° and close to the nadir [Mutlow et al., 1999]. ATSR-2 was launched in 1995 and succeeded by the Advanced Along Track Scanning Radiometer (AATSR) in 2002. It has a swath width of 512 km and achieves global coverage every 3 days [Mutlow et al., 1999].

1.6.2 SEVIRI

SEVIRI is aboard the Meteosat Second Generation (MSG-2) platform which is in geostationary orbit centered over the African continent and the Atlantic ocean. It has a temporal resolution of 15 minutes and makes observations in eleven spectral channels centred near 0.6, 0.8, 1.6, 3.9, 6.2, 7.3, 8.7, 9.7, 10.8, 13 and 13.4 μm. SEVIRI makes observations at a spatial resolution of 3×3 km in the nadir and this gets coarser towards the edges of the observation disk. SEVIRI also has a high resolution visible channel covering wavelengths between 0.5 - 0.9 μm, providing data at a spatial resolution of 1×1 km in the nadir [Schmetz et al., 2002].

Table 1.2: ATSR-2 and SEVIRI Instrument Characteristics

Instrument	ATSR-2	SEVIRI
Satellite	ERS-2	MSG-2
Orbit	Near polar sun-synchronous, 10.30 equator overpass in the descending node.	Geostationary
Viewing Angles	Dual View: 55° forward view and nadir.	Nadir at the sub-satellite point with viewing zenith angle increasing towards the edge of the disk.
Spatial Resolution	1×1 km at the swath centre in the nadir and 1.5×2 km at the swath centre in the forward view.	3×3 km in the nadir.
Temporal Resolution	3 days for global coverage.	15 minutes
Observation Channels	0.55, 0.67, 0.87, 1.6, 3.7, 11 and 12 μm.	0.6, 0.8, 1.6, 3.9, 6.2, 7.3, 8.7, 9.7, 10.8, 12, 13.4 μm and HRV (0.5–0.9 μm).

1.6.3 The ORAC Retrieval Scheme

A satellite instrument measures top of the atmosphere (TOA) radiance which is comprised of a mixture of scattered and reflected shortwave radiation, and thermal longwave radiation emitted from the Earth's surface, atmospheric gases, aerosols and clouds. Figure 1.5 shows the complex interactions of short and longwave radiation within the Earth's atmosphere which contribute to the signal observed by the satellite.

There is not enough information in the observed satellite radiance to unambiguously determine cloud or aerosol properties and consequently this signal is interpreted through the use of a forward model describing atmospheric radiative transfer. The ORAC forward model uses the Discrete Ordinances Radiative Transfer (DISORT) model [Stammes et al., 1988] to model radiance as a function of the properties of a plane parallel aerosol or cloud layer with an assumed vertical distribution . Within the GRAPE dataset from ATSR-2 cloud properties are derived using the 0.67, 0.87, 1.6, 11 and 12 μm channels. Aerosol properties derived from both ATSR-2 and SEVIRI use data from the 0.67, 0.87 and 1.6 μm channels.

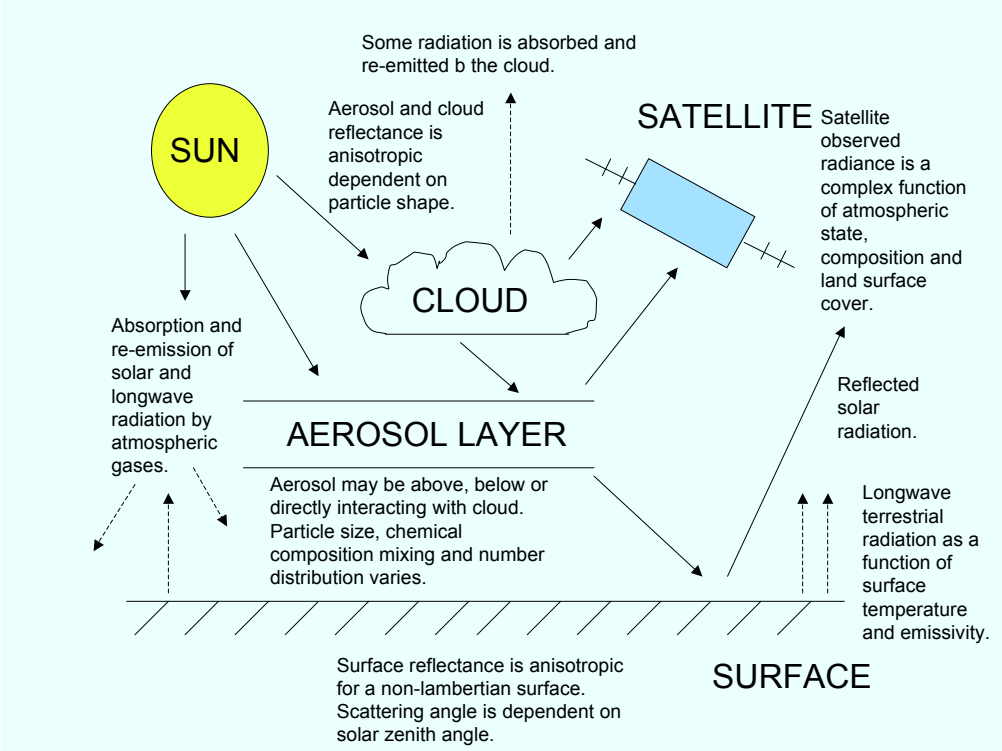

Figure 1.5: Radiative transfer pathways of solar shortwave and terrestrial longwave radiation within the atmosphere. Solid arrows represent solar radiation and dashed arrows terrestrial radiation.

The retrieval scheme was originally developed for clouds [Watts et al., 1998] and later extended to include aerosol retrievals [Marsh et al., 2004]. Clouds are identified using a number of threshold tests. Over the ocean this is based on the observed thermal radiance, whilst over the land additional tests based on surface reflectance are used to identify low, warm clouds [Birks, 2007]. Retrieved cloud properties within the GRAPE dataset include cloud effective radius, liquid water path, cloud fraction, cloud top height, pressure and temperature.

The ORAC forward model for aerosol observations applied to cloud-free scenes contains four separate elements: 1) a model of atmospheric radiative transfer, 2) a model of atmospheric gas absorption, 3) a model of aerosol absorption and scattering and 4) a model of surface reflectance. In order to make an aerosol retrieval, some assumptions about the aerosol size and chemical composition have to be made to model aerosol forcing. The ORAC retrieval uses aerosol properties taken from the Optical Properties of Aerosol and Cloud (OPAC) database [Hess et al., 1998]. Within the GRAPE retrieval a simple global climatology is used to allocate continental, maritime, desert,

Arctic or Antarctic aerosol as shown in Figure 1.6. For the SEVIRI retrieval, the algorithm is run five times for each pixel assuming desert dust, maritime, urban, continental and biomass burning aerosol. Aerosol type is selected using the retrieval with the lowest cost function after quality control tests have been performed. From the size distribution and refractive indices specified for each aerosol class within the OPAC database, Mie scattering code is used to determine the aerosol optical properties which are used within the ORAC forward model, including the aerosol phase function, scattering and extinction coefficients, which are placed in look-up tables (LUTs).

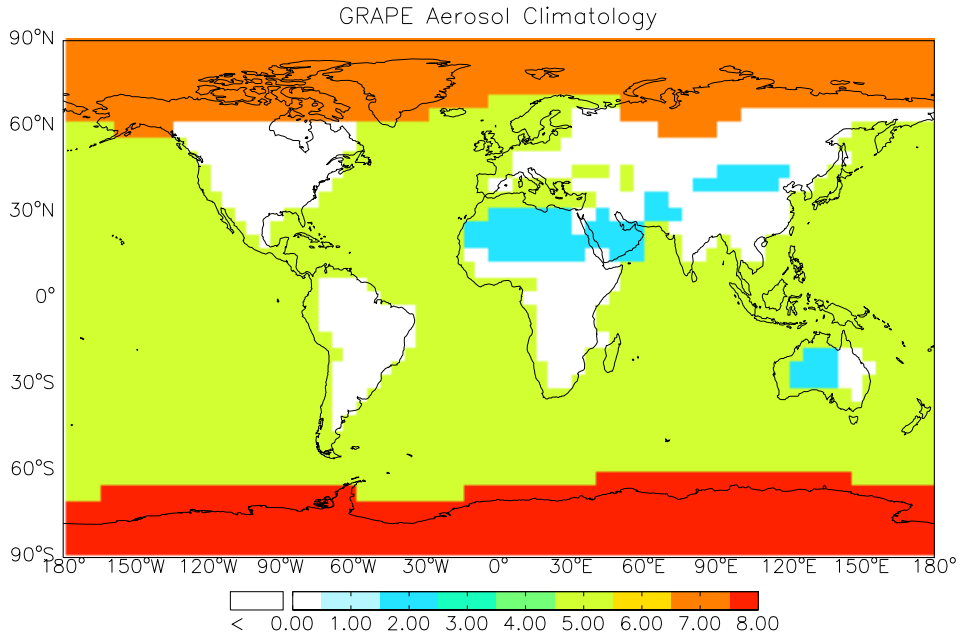

Figure 1.6: Climatology used to assign aerosol type within the GRAPE retrieval. Aerosol is classified as follows, 0 = Continental, 2 = Desert, 5 = Maritime, 7 = Arctic, and 8 = Antarctic.

Simulated and observed radiances are fitted using an optimal estimation retrieval scheme enabling all retrieved parameters (aerosol optical depth, aerosol effective radius and surface albedo) to vary simultaneously, to calculate the retrieved state with the maximum probability whilst accounting for the measurements and the *a priori* aerosol properties and the uncertainties in both [Rodgers, 2000]. The forward model, **F**, is fitted to the observed radiances by minimising the cost function, J(**x**) using the Levenberg-Marquardt algorithm [Thomas et al., 2009a]. This describes the fit between the measurement vector **y** (the observed radiances), the modelled radiances, the state vector **x** and the *a priori* state vector $\mathbf{x_a}$. $\mathbf{S_y}$ and $\mathbf{S_a}$ are the error covariance matrices for the measurement

and state vector respectively.

$$\boldsymbol{J}(x) = (\mathbf{F}(x) - \mathbf{y})\mathbf{S}_y^{-1}(\mathbf{F}(x) - \mathbf{y})^{\mathrm{T}} + (\mathbf{x} - \mathbf{x}_a)\mathbf{S}_a^{-1}(\mathbf{x} - \mathbf{x}_a)^{\mathrm{T}} \tag{1.1}$$

The stages of this retrieval are also described schematically in Figures 1.7 and 1.8.

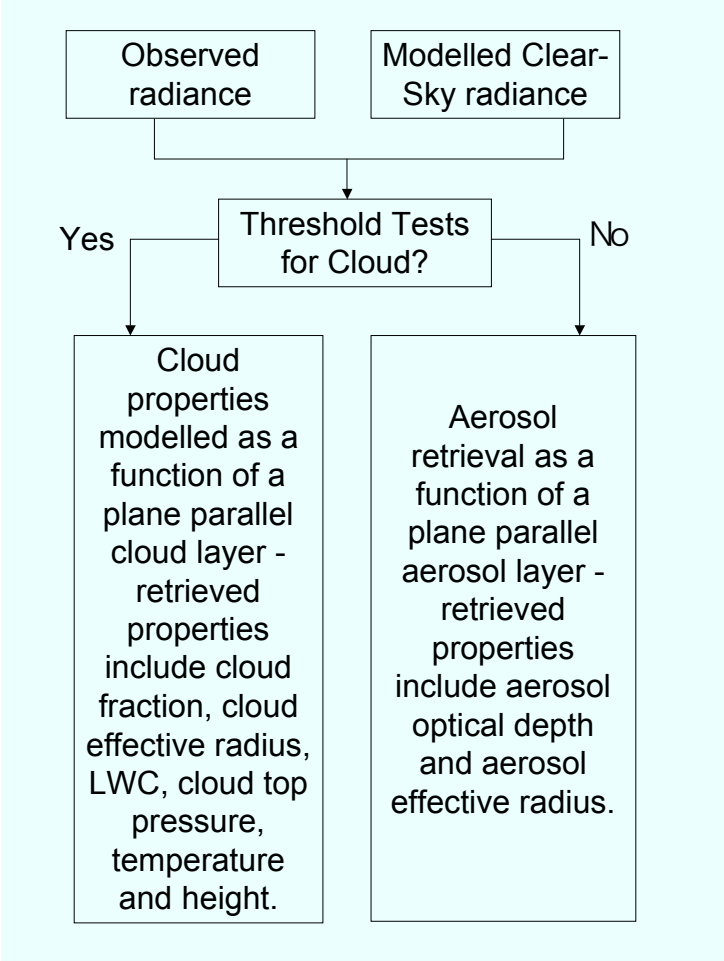

Figure 1.7: Schematic of the decision making process to decide whether to perform an aerosol or cloud retrieval.

Figures 1.9 and 1.10 from the GlobAerosol Validation report show a monthly comparison of SEVIRI AOD from the ORAC against MODIS AOD, in January and July of 2006 [Poulsen et al.,

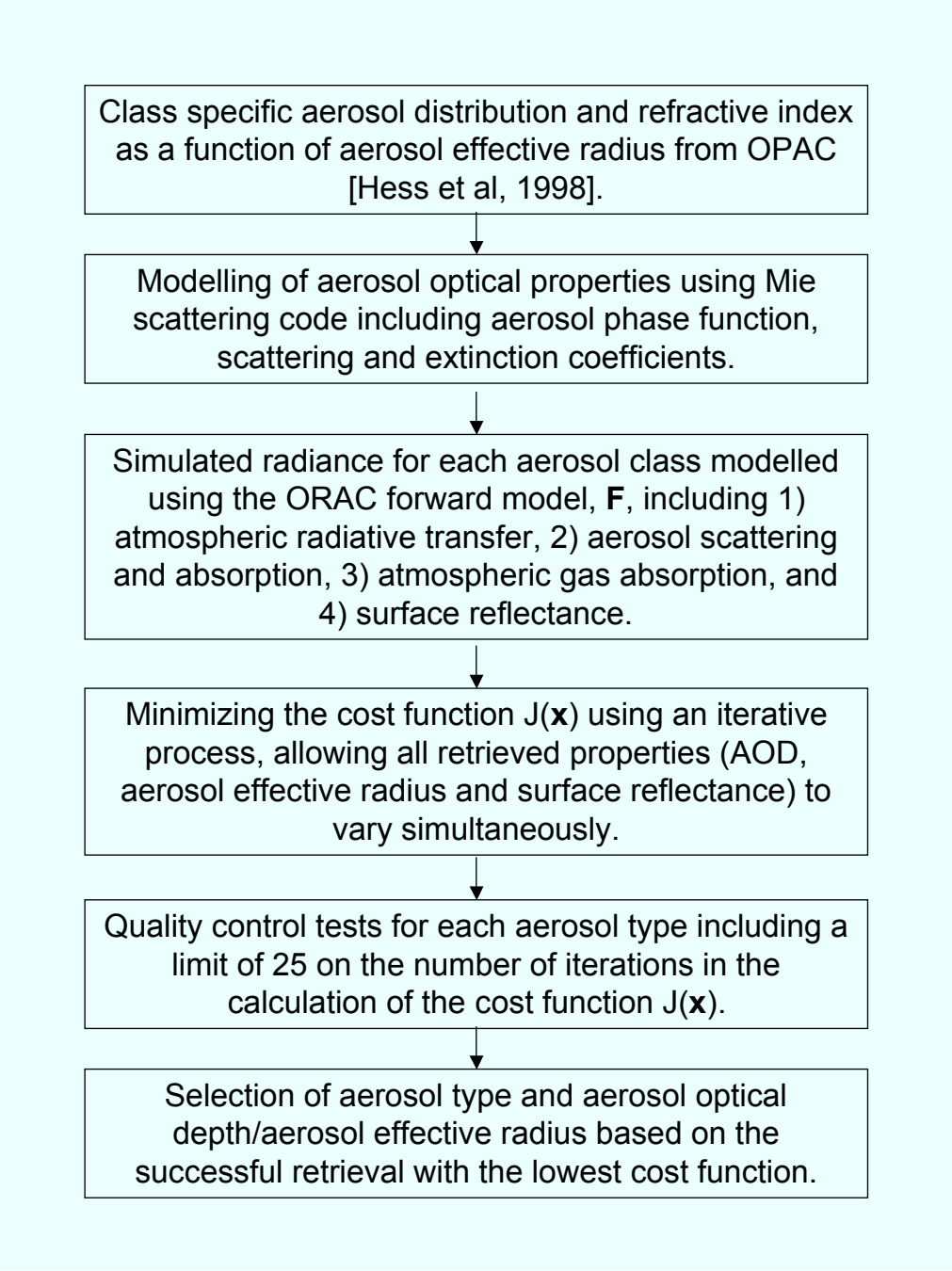

Figure 1.8: Schematic of the ORAC optimal estimation retrieval scheme.

2009]. In both months the ORAC retrieval algorithm performs better over ocean than over the land and the spatial extent of the aerosol outflow across the Atlantic is similar in both retrievals. Al-

though this agreement is encouraging, both retrieval schemes are dependent on some assumptions about the observed aerosol properties and therefore neither can be considered as 'truth' against which to make a comparison (for further discussion on the sensitivity of aerosol retrievals to *a priori* assumptions please refer to chapter 3).

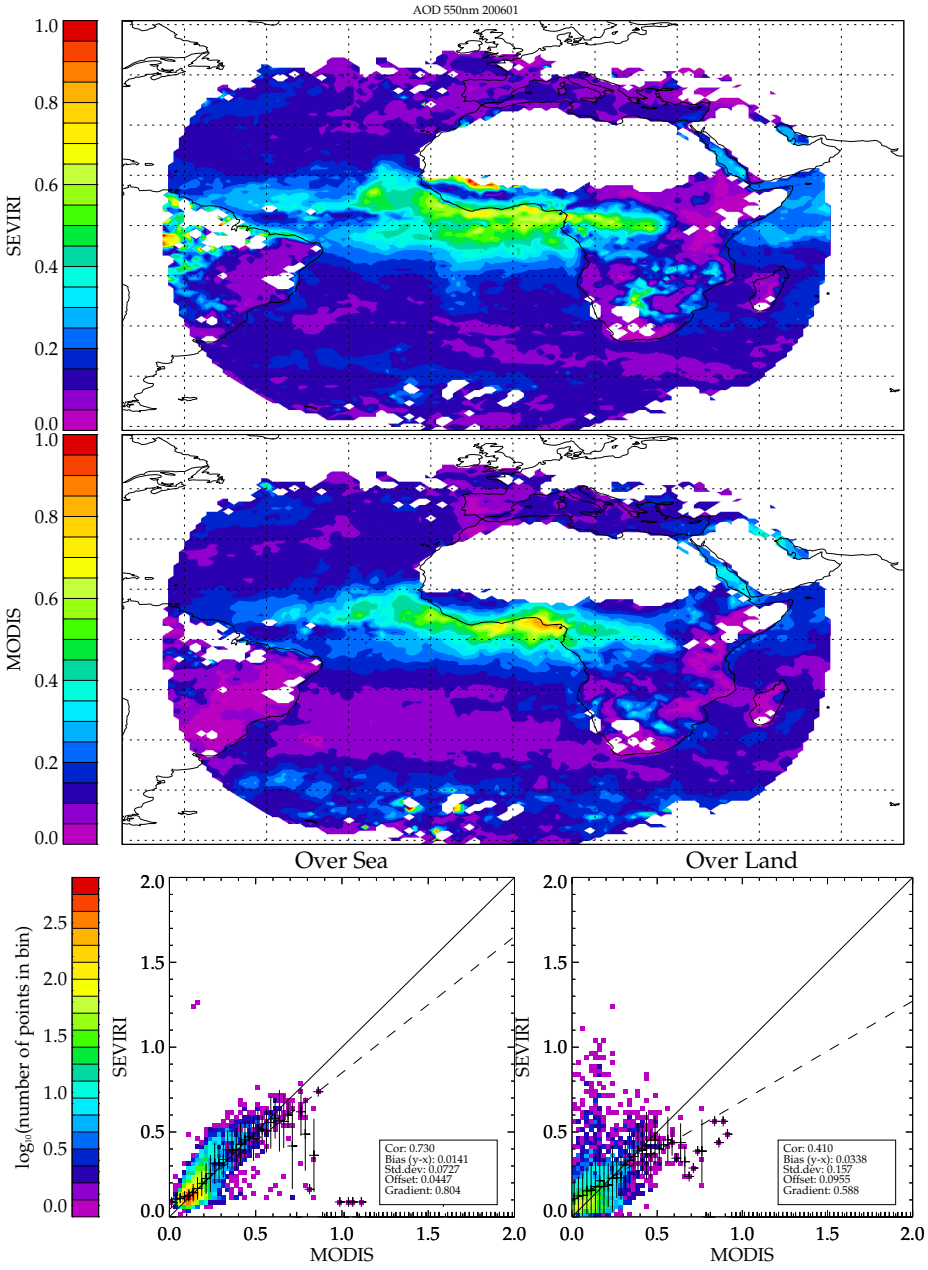

Figure 1.9: Comparison of MODIS and SEVIRI ORAC AOD for January 2006 [Poulsen et al., 2009].

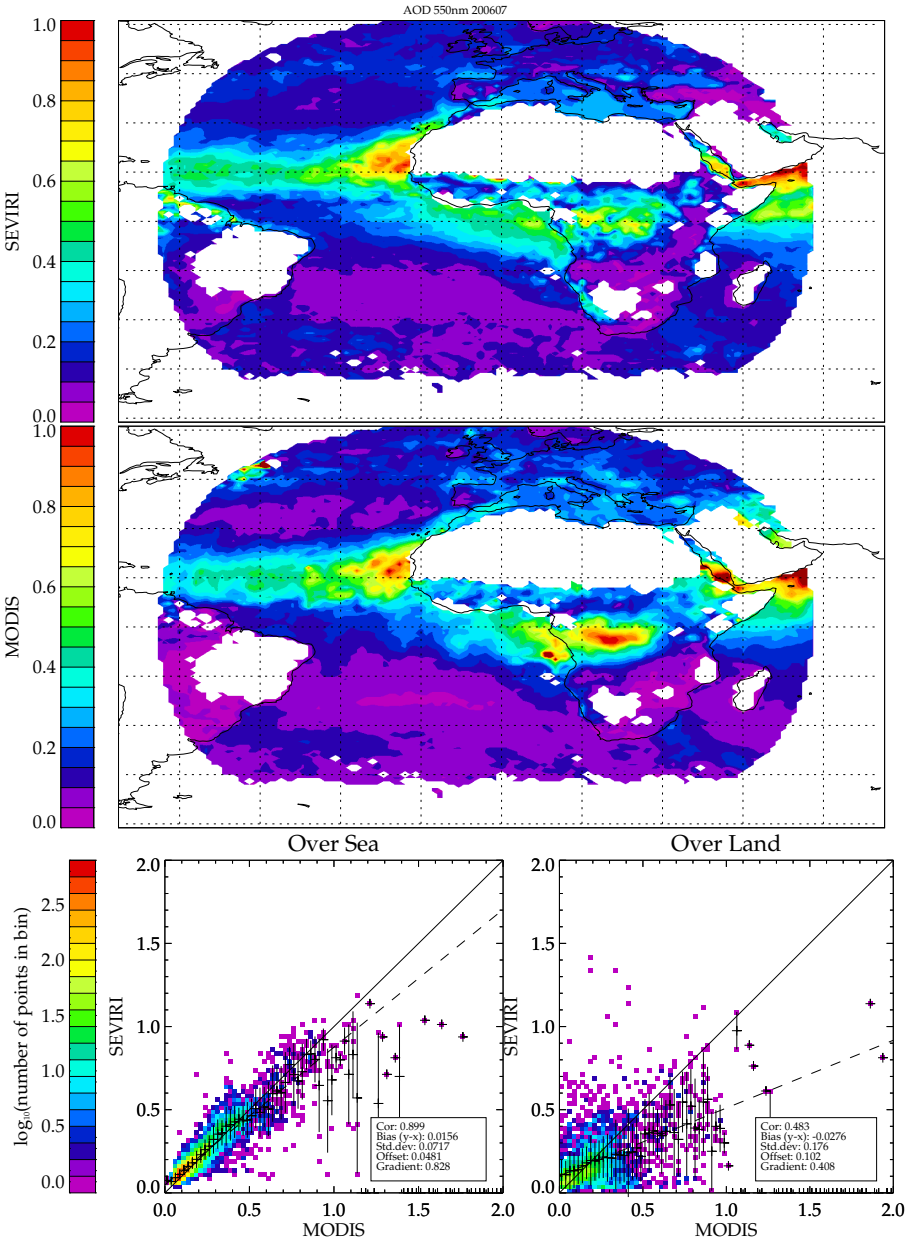

Figure 1.10: Comparison of MODIS and SEVIRI ORAC AOD for July 2006 [Poulsen et al., 2009].

Given the difficulties in validating satellite data using data from other satellite instruments, AERONET ground based observations are often used as 'truth' against which to compare satellite retrievals. Figure 1.11 shows a daily validation of SEVIRI ORAC observations agains AERONET measurements during 2006. As with the inter-satellite comparison, the best agreement is seen at coastal and marine sites and use of these data in this thesis is limited to these regions.

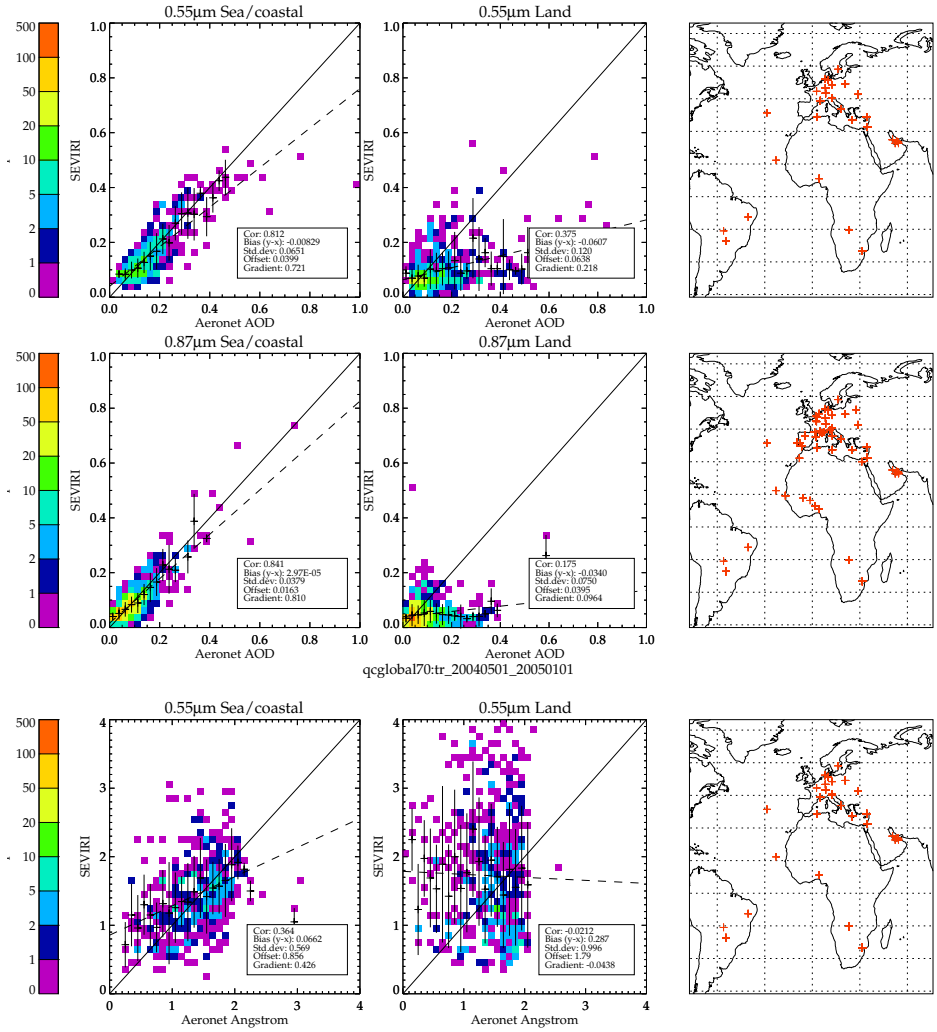

Figure 1.11: Comparison of Aeronet with SEVIRI retrievals over sea and over land. The map shows the AERONET stations used. [Poulsen et al., 2009].

1.6.4 Saharan Dust Index (SDI)

The SDI is a a tool originally developed by Merchant et al. [2006] to identify dust aerosol contamination of nighttime sea-surface temperature retrievals, using observations at infrared wavelengths. In chapters 3 and 4 I apply the detection method to the SEVIRI data at the native spatial resolution of 3×3 km. The SDI identifies dust using variance in 3D brightness temperature difference space between different infrared channels (3.9 - 8.7 μm, 3.9 - 12 μm and 11 - 12 μm). SDI values are calculated using principle component analysis (PCA). Variance caused by changing atmospheric variables including water vapour are identified along PC1, whilst aerosol induced variance is observed along PC2 [Merchant et al., 2006]. SDI values are scaled to be comparable to aerosol optical depth and dust is identified when the SDI is in the range 0.25 - 2. The equation defining

the nighttime SDI (nsdi) is as follows:

$$nsdi = 0.531781 \times (\mathrm{BT}_{3.9} - \mathrm{BT}_{8.7}) - 0.846882 \times (\mathrm{BT}_{10.8} - \mathrm{BT}_{12}) + 1.46460 \qquad (1.2)$$

where $\mathrm{BT}_{3.9}$ denotes brightness temperatures in the 3.9 μm channel with the same notation used for the other channels.

This algorithm was originally developed to work at night and was later adapted to work during the day when the 3.9 μm channel was contaminated by solar radiation. To calculate daytime SDI values a local regression is performed between daytime radiance in the three available channels and the nighttime SDI values. Merchant [2006] found these regression coefficients for estimating daytime SDI to be valid over a length scale of $\sim$ 200 km and a timescale of one day. In my application of this index I perform the regression using nighttime SDI observations from midnight on both the preceding and following day and apply a linear weighting to the results according to time of day.

Figure 1.12 gives an example of the nighttime SDI calculated using data from SEVIRI for both a dust plume across the Mediterranean, and dust over the Atlantic. It also shows the corresponding daytime estimator of the SDI for the same scene. The daytime SDI shows good agreement with the nighttime SDI values although there is some dampening of the SDI signal during the day [Merchant, 2006]. The SDI standard deviation using a moving 3×3 pixel window can be used to identify contamination by sub-pixel cloud. I take into account the dampened signal in the daytime estimator in chapter 3 by lowering the threshold for discarding scenes with a high standard deviation during the day.

1.6.5 EUMETSAT cloudmask

In chapters 3 and 4 I use data from the SEVIRI instrument cloud screened using the EUMETSAT cloudmask. The EUMETSAT cloudmask performs a basic classification of pixels into three categories: clear sky over water, clear sky over land and cloud. All of the SEVIRI channels are used in the cloud masking algorithm with the exception of the high resolution visible and the 9.7 μm

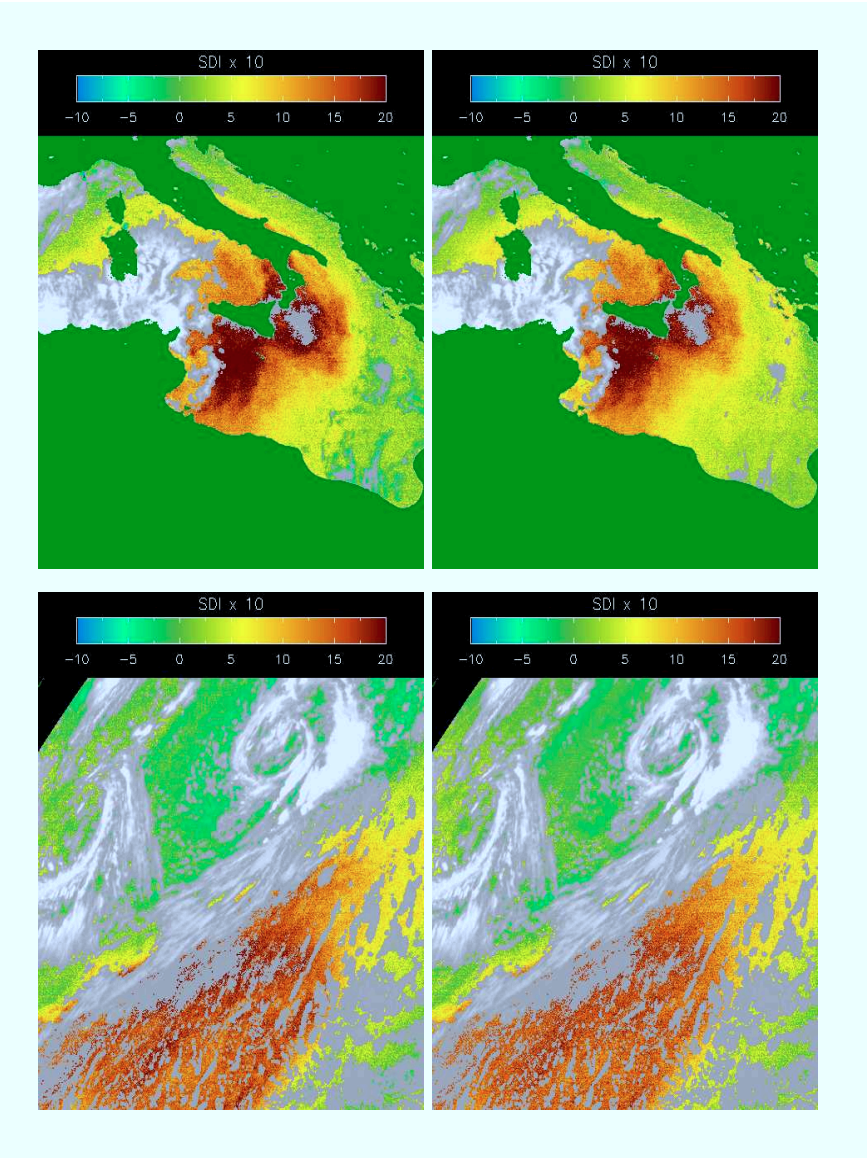

Figure 1.12: Nighttime (left) and daytime (right) SDI from SEVIRI data calculated at full satellite resolution. Top: SDI over the central Mediterranean. Bottom: SDI over the Atlantic. [Merchant, 2006].

channel. Six groups of threshold tests are performed using these data: 1) reflectance tests using data from the solar channels, 2) reflectance difference tests from combinations of solar channels, 3) temperature tests using infrared channels, 4) temperature difference tests using infrared channels, 5) standard deviation tests using infrared channels on a moving 3×3 pixel target and 6) snow and ice tests giving a total of 34 tests [Lutz, 1999a]. Each test is performed independently

and the selection of tests used is tailored to the pixel location, viewing geometry and solar zenith angle [Lutz, 1999a].

Cloud masking is not done without difficulty, and some cloud types are harder to identify than others, for example thin cirrus, sub-pixel cloud, cloud over snow and ice and cloud over heterogeneous land surfaces. Typically, high aerosol loading may also be flagged as cloud. Figures 1.13 and 1.14 taken from the EUMETSAT Cloud Detection Algorithm Theoretical Basis Document (ATBD) give an indication of how well the EUMETSAT cloudmask performs. The AOD retrieval (in Figure 1.14) which is particularly sensitive to mis-classified cloud gives some insight into where erroneous classification has been made. The high AOD shown in red in Figure 1.14 is a dust storm over the Atlantic but the purple coloured pixels with AOD > 1 are likely to be mis-classified cloud [Lutz, 1999a]. In regions of lower AOD a similar effect can also be seen. This is an inherent problem with all current cloud detection algorithms and can limit the suitability of these data for use in aerosol and cloud studies. In the work I have presented in chapters 3 and 4 I address this problem by extending the cloudmask by one pixel in each direction to eliminate erroneously classified cloud edges.

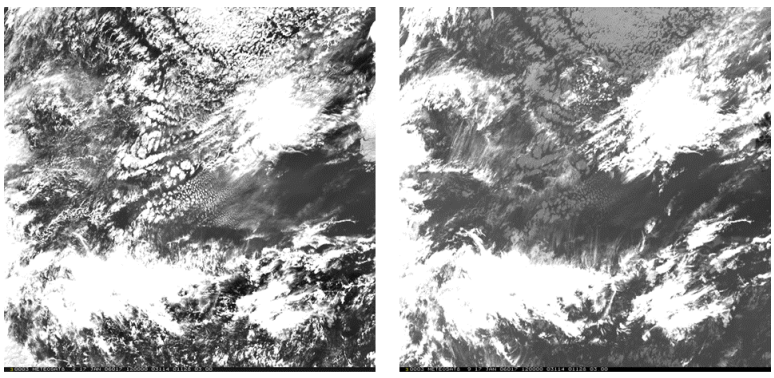

Figure 1.13: MSG SEVIRI imagery over the mid-Atlantic on 17th January 2006 at 1200 UTC from the 0.8 μm(left) and 10.8 μm (right) channels [EUMETSAT, 2007]

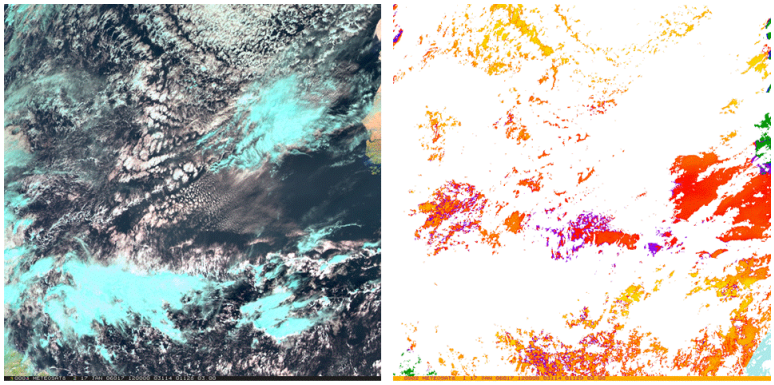

Figure 1.14: MSG SEVIRI RGB image using the 1.6, 0.8 and 0.6 μm channels (left). AOD retrieval (right). Colours are as follows: white = cloud, green = land, cyan = sunglint, yellow - orange - red - purple corresponds to AOD of 0.1 - 0.4 - 0.7 - 1 [EUMETSAT, 2007].

1.7 Thesis Outline

1.7.1 Research Questions

I set out below three research questions which I aim to address in this thesis, to which each results chapter corresponds. In chapter 5 I critically examine whether the research undertaken has succeeded in answering the questions posed and whether further research is necessary to increase our understanding of the arising issues.

1. Increases in global temperatures as a response to anthropogenic greenhouse gas emissions have prompted attempts to model future climate under a number of different emission scenarios. One of the largest remaining uncertainties in this process is modelling the aerosol component of the radiative budget. The problem is two-fold, arising from an incomplete understanding of direct aerosol forcing and aerosol-cloud interaction, and the inability of global models to resolve aerosol processes which occur on a microphysical scale. Of the two major types of aerosol forcing, indirect effects are the least well understood. **The Twomey [1974] hypothesis outlines aerosol forcing through the cloud albedo effect but is this sufficient to parameterise aerosol forcing via the first indirect effect on a global scale?**

2. Satellite data are becoming increasingly important in aerosol research as they provide a global view of aerosol forcing. Satellite radiances do not contain enough information to uniquely determine aerosol optical properties and have to be interpreted using a forward

model simulating radiative transfer. The aerosol element of this forward model has to be constrained by data describing aerosol characteristics which are often poorly defined on a global scale and show significant spatial and temporal heterogeneity. **To what extent can we rely on satellite retrievals to give accurate measures of aerosol optical properties?**

3. Satellite observations show that Saharan dust plumes extend over the northern tropical Atlantic during summer months, over a region characterised by low-level stratocumulus clouds. These type of clouds are particularly sensitive to aerosol forcing as their albedo is significantly higher than that of the underlying ocean. **Dust is widely considered as hydrophobic and consequently does not readily act as cloud condensation nuclei but to what extent does it exert a radiative forcing through semi-direct aerosol-cloud interactions?**

1.7.2 Outline

The research in this thesis is presented in the format of three research papers. The paper in chapter 2 is presented in its published form in Geophysical Research Letters, the paper in chapter 3 is accepted for publication by the Journal of Geophysical Research, and the paper in chapter 4 is in preparation for submission. Consequently, each chapter includes its own methodology, results and discussion and is a complete piece of research in and of itself. In chapter 5 I draw together all of the results presented in chapters 2–4 in a detailed discussion of the research methodology, the collective findings of the research, the implications that these have for the field of aerosol research and recommended future work.

Chapter 2

Regional and seasonal variations of the Twomey indirect effect as observed by the ATSR-2 satellite instrument[1]

2.1 Declaration

All of the work done in this chapter is my own. This has been published as a paper in Geophysical Research Letters with the exception of the extended discussion section at the end. The contribution of the other authors is as follows; Paul Palmer was my PhD supervisor at Edinburgh and Richard Siddans my supervisor at the Rutherford Appleton Laboratory. All of the other authors are based either at RAL or the University of Oxford and were involved with the development of the ORAC algorithm or its application to the ATSR-2 data to form the GRAPE dataset.

2.2 Abstract

[1] We use satellite observations of aerosol optical depth τ_a and cloud effective radius r_e from the ATSR-2 instrument in 1997 to investigate the Twomey indirect effect (IE, -∂ ln r_e /∂ ln τ_a) in regions of continental outflow. We generally find a negative correlation between τ_a and r_e with the strongest inverse relationships downwind of Africa. North America and eastern Asian continental outflow exhibits a strong seasonal dependence, as expected. Global values for IE range from 0.10 to 0.16, consistent with theoretical predictions. Downwind of Africa, we find that the IE

[1]Citation: Bulgin, C. E., P. I. Palmer, G. E. Thomas, C. P. G. Arnold, E. Campmany, E. Carboni, R. G. Grainger, C. Poulsen, R. Siddans, and B. N. Lawrence (2008). Regional and Seasonal variations of the Twomey indirect effect as observed by the ATSR-2 satellite instrument, *Geophys. Res. Lett., 35*, L02811, doi:10.1029/2007GL031394.

is unphysically high but robust ($r = -0.85$) during JJA associated with high aerosol loading, and attribute this tentatively to the Twomey hypothesis accounting only for a limited number of physical properties of aerosols.

2.3 Introduction

[2] Atmospheric aerosols represent one of the largest uncertainties in current understanding of Earth's climate [Forster et al., 2007]. Aerosols affect the atmospheric radiation balance by absorbing and scattering solar radiation (direct effect), the magnitude of which depends on a number of factors including chemical composition, size distribution, and mixing state. Aerosols also affect cloud radiative properties by acting as cloud condensation nuclei (CCN) (indirect effects, IE), also depending on size and chemical composition. Assuming a constant liquid water path, elevated concentrations of aerosols effectively increase the cloud droplet number and subsequently reduce the mean cloud droplet size, leading to an increase in cloud albedo [Twomey, 1974]. Reduced cloud droplet size suppresses precipitation and increases cloud lifetime [Albrecht, 1989]. Accurate modelling of these indirect effects involves detailed aerosol microphysics, and is therefore difficult to use in large-scale chemistry-climate models [Forster et al., 2007].

[3] There are a number of anthropogenic and natural sources of aerosols [Seinfeld and Pandis, 1998]. The main sinks of aerosols are gravitational settling and wet deposition, the relative importance of which depends on the aerosol physical and chemical properties, leading to lifetimes of typically a few days. Such short lifetimes give rise to rapid spatial and temporal variations in loading and chemical composition, not well suited for study by sparse ground-based measurement networks. Satellite observations offer a global perspective but currently they only measure a small number of aerosol and cloud optical properties, e.g. optical depth and single scattering albedo [Forster et al., 2007]. A number of previous studies using data from satellite sensors have inversely correlated high aerosol optical depths (used as a proxy for aerosol number) and cloud droplet properties in continental outflow eg. [Avey et al., 2007] or globally [eg. [Bréon et al., 2002]].

[4] Here, we use satellite observations of aerosol and cloud optical properties from the Global

Retrieval of ATSR Cloud Parameter and Evaluation (GRAPE) dataset [Watts et al., 1998; Marsh et al., 2004], to quantify the Twomey Indirect Effect (IE), as discussed below. In this analysis we use cloud droplet effective radius, r_e, the area weighted mean radius of cloud droplets, and aerosol optical depth, τ_a, a measure of total column light extinction due to scattering and absorption of aerosol particles.

2.4 Data

[5] The second Along-Track Scanning Radiometer (ATSR-2), aboard the ERS-2 satellite, observes reflected solar radiation and terrestrial and atmospheric emission in seven spectral channels spanning the visible and infrared. ERS-2 is in a near-polar, sun-synchronous orbit with an equator overpass time of 10:30 local time in the descending node. ATSR-2 has a 512 km swath width in the nadir [Mutlow et al., 1999], achieving global coverage every three days.

[6] Aerosol and cloud properties are derived using the Oxford-RAL Aerosol and Cloud (ORAC) optimal estimation retrieval scheme that was developed for clouds [Watts et al., 1998] and extended to aerosols [Marsh et al., 2004]. The retrieval scheme averages a block of 12 ATSR-2 pixels to achieve an effective resolution of 2.6 km across-track and 3.5 km along-track. The scheme uses the Discrete Ordinates Radiative Transfer model [Stammes et al., 1988] to calculate the top of atmosphere radiance as a function of the properties of a plane parallel cloud or aerosol layer with an assumed height distribution. ORAC fits the radiance in all channels by varying all retrieved parameters simultaneously, while accounting for *a priori* information. The scheme also provides error estimates on all retrieved quantities.

[7] Cloud flagging is performed prior to retrieval. Over the ocean the difference between the observed thermal radiance and a clear sky (cloud and aerosol free) value predicted by radiative transfer calculation is used. We also employ an additional test to detect low, warm clouds over the ocean and clouds over land based on surface reflectance at 0.67 and 0.87 μm [Birks, 2007]. Cloud properties are retrieved using the 0.67, 0.87, 1.6, 11 and 12 μm channels and the derived products are optical depth at 0.55 μm, effective radius, liquid water path (LWP), cloud top height, pressure

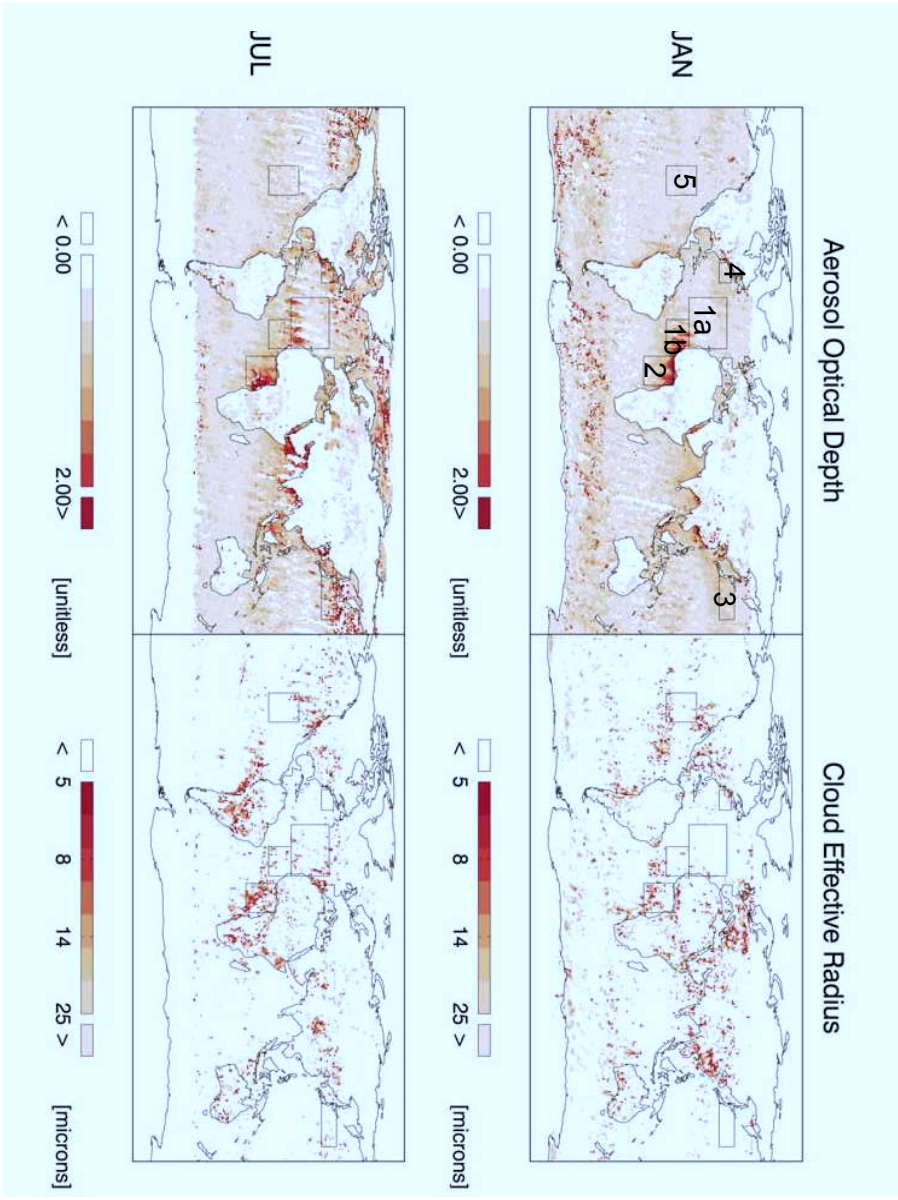

Figure 2.1: Monthly mean τ_a (unitless) at 0.55 μm and r_e (μm) observed by ATSR-2 onboard ERS-2 during January and July 1997. Data are averaged on a regular $1^\circ \times 1^\circ$ grid with cloud data filtered for cloud top heights $<$3 km, with an error associated with this measure $<$200 m, and for 2 μm $< r_e <$ 25 μm. Aerosol data are filtered according to τ_a error $<$0.25. The striped structure in the plots is an artefact of ATSR-2 sampling. The boxes indicate the regions defined in Table 1 where 1a) South Atlantic (Sahara) in MAM, JJA, SON, 1b) South Atlantic (Sahara) in DJF, 2) eastern equatorial Atlantic (north Africa), 3) western north Pacific (Asia), 4) western mid-latitude north Atlantic (North America) and 5) south Pacific (control case).

and temperature and cloud fraction. Aerosol optical depth at 0.55 μm and aerosol effective radius are retrieved using the 0.67, 0.87 and 1.6 μm channels. The Optical Properties of Aerosol and Clouds (OPAC) inventory provides the *a priori* information on aerosol optical properties [Hess et al., 1998], with the aerosol type used in each pixel being assigned from aerosol climatology.

[8] Validation of both cloud and aerosol properties derived using the ORAC algorithm in the GRAPE dataset is ongoing [Poulsen and Watts, 2002; Kokhanovsky et al., 2007; Thomas et al., 2007a]. We use only retrieved aerosol and cloud data where the retrieval algorithm converged within 10 iterations. For cloud data we use retrievals that have cloud top heights below 3 km (with an error of $<$ 200m), ensuring that we use only low-level clouds that are most likely to be influenced by boundary layer outflow [Keil and Haywood, 2003]. Measurements of r_e below 2 μm are removed to prevent contamination of cloud retrievals with erroneously flagged aerosol; r_e values above 25 μm representing $< 10\%$ of data, are unrealistic for low-level cloud and have also been filtered from the data [Han et al., 1998]. We only consider aerosol retrievals that have τ_a errors < 0.25.

2.5 Results

[9] Figure 2.1 shows monthly mean values of τ_a and r_e in January and July 1997 averaged on a regular 1°x1° grid. Observed τ_a values are typically 0-0.8 with the highest values reaching 2 over the eastern Atlantic downwind of Africa. During January there are elevated values of τ_a over the western Pacific, the Arabian Sea, the Bay of Bengal, the South China Sea, the eastern tropical Atlantic, and the Southern Ocean. There are similar distributions of elevated τ_a during July but with smaller values over the western Pacific and higher values over the mid-latitude western Atlantic downwind of North America. Values of r_e range from 5 to 25 μm with the smallest values observed over the oceans in regions of continental outflow.

[10] We quantify the Twomey IE over four regions of continental outflow, ensuring a fresh supply of aerosol for cloud droplet formation: eastern equatorial Atlantic (North Africa), eastern South Atlantic (southern Africa), western mid-latitude North Atlantic (North America), and western North Pacific (eastern Asia) which correspond to the boxes in Figure 2.1. We also consider data

over the remote Pacific (used as a control), and over the globe. Table 2.1 defines the geographical regions shown in Figure 2.1. We find the largest τ_a values over the eastern South Atlantic, downwind of Africa (Figure 2.1). The southward migration of elevated τ_a over that region during 1997 (not shown) reflects the burning season in Africa, and is consistent with the spatial distribution of ATSR-2 firecounts. In DJF analysis for the eastern South Atlantic is in a box just below the Saharan region (shown in Figure 2.1) in order to capture this seasonal variation in biomass burning.

[11] Previous studies have argued that aerosol index (AI), a measure of the wavelength dependence of aerosol extinction, is a better quantity to test the Twomey hypothesis because it is sensitive to the fine fraction of aerosol that is more likely to serve as CCN [Bréon et al., 2002; Quaas et al., 2004]. AI is not directly retrieved in the GRAPE algorithm but can be approximated by the product of τ_a and the Angström exponent (A). The Angström exponent varies inversely with particle size, the difference between extinction coefficients at two wavelengths being greater with respect to smaller particles as determined by Mie scattering. We approximate A using $A \approx \log(b_{ext1}/b_{ext2})/\log(\lambda_1/\lambda_2)$, where λ represents wavelength and b_{ext} represents an extinction coefficient related to a particular aerosol class and effective radius in two spectral bands ($_1$ and $_2$) [Seinfeld and Pandis, 1998]. Here, we evaluate A at two wavelengths, 0.55 and 0.67μm. OPAC classifications give values of b_{ext} according to wavelength, dependent on the mixing ratio of each aerosol component in the aerosol class [Hess et al., 1998]. This mixing ratio is then varied in order to calculate b_{ext} as a function of aerosol effective radius [Thomas et al., 2007].

[12] A major criticism of using satellite data to test relationships between aerosol and cloud properties has been that these properties are not measured coincidently [Avey et al., 2007]. Previous studies have used back-trajectories to link cloud and aerosol properties eg. [Bréon et al., 2002], or co-located cloud retrievals and trace gas measurements using a tracer transport model [Avey et al., 2007]. *Breon et al*, [2002] used back-trajectories to couple aerosol and cloud retrievals and found that the distance between measurements is typically less than 100 km. We argue here that analysis of aerosol and cloud properties derived from multi-day and seasonal mean averages at $1^\circ \times 1^\circ$ resolution (approximately 100 x 100 km^2 at low and mid-latitudes) negates the need to couple individual measurements.

Table 2.1: Seasonal Mean Twomey IE ($-\partial \ln r_e / \partial \ln \tau_a$) and Associated Correlations Between r_e and τ_a During 1997

	Globe [a]		Eastern S. Atlantic [b] (Africa)		Western N. Pacific [c] (Asia)		Western N. Atlantic [d] (North America)		Eastern Equatorial Atlantic [e] (Sahara)		S.Pacific [f]	
Month	IE[g]	r	IE	r	IE	r	IE	r	IE	r	IE	r
DJF	0.13±0.01[h]	-0.75	0.20±0.13[hkl]	-0.36	0.12±0.05[h]	-0.68	-0.56±0.13	0.92	0.10±0.02[h]	-0.88	-0.37±0.08	0.65
MAM	0.13±0.01[h]	-0.87	-0.48±0.03	0.38	-0.14±0.01	0.56	0.11±0.11[j]	-0.44	-0.06±0.03	0.74	0.001±0.09[j]	-0.54
JJA	0.16±0.01[h]	-0.99	0.51±0.16[ik]	-0.85	-0.04±0.05[j]	-0.13	0.16±0.08[h]	-0.78	0.16±0.04[h]	-0.48	-0.16±0.09	-0.50
SON	0.10±0.01[h]	-0.98	0.27±0.05[h]	-0.85	0.23±0.06[h]	-0.94	-0.16±0.19[i]	0.70	-0.03±0.03[j]	0.64	-0.37±0.07	0.85

[a] Region defined:180W - 180E, 45S - 60N; τ_a:r_e correlation = 0.38; AI: r_e correlation = 0.68.
[b] Region defined: 10W - 10E, 15S - 5N; τ_a:r_e correlation = -0.39; AI:r_e correlation = -0.64.
[c] Region defined: 140E - 170E, 35N - 45N; τ_a:r_e correlation = -0.47; AI:r_e correlation = -0.36.
[d] Region defined: 60W - 74W, 35N - 43N; τ_a:r_e correlation = 0.23; AI:r_e correlation 0.37.
[e] Region defined: 15W - 50W, 15N - 40N; τ_a:r_e correlation = -0.33; AI:r_e correlation = 0.13.
[f] Region defined: 120W - 140W, 0N - 20N; τ_a:r_e correlation = -0.17; AI:r_e correlation = 0.16.
[g] To obtain the gradient, r_e was averaged over τ_a size bins of 0.03, between 0.13 and 0.4 in the given region over the period of each season.
[h] An IE consistent with theory assuming $\alpha < 1$.
[i] Regions where $N_d \approx (N_a)^{\alpha}$ cannot be assumed.
[j] Regions where the retrieved IE value is not significant.
[k] The gradient IE was calculated for τ_a values of 0.35-1.5.
[l] Region defined: 15W - 35W, 0N - 15N.

[13] Figure 2.2 shows time series of τ_a, AI and r_e from 1st December 1996 to 31st January 1998, averaged individually across the six regions defined in Table 1. Standard deviations for daily mean τ_a (AI) range from 0.04-0.06 (0.01-0.05), but can reach up to 0.2 for τ_a and AI in strong continental outflow. Standard deviations for r_e typically range from 4 to 6 μm. The 28-day rolling mean reduces the random noise on the daily means. All regions that include continental outflow show coherent variations in aerosol and cloud properties. The timing of the maximum values of τ_a and AI are consistent with prior knowledge of outflow patterns, eg. outflow over the western Atlantic is at a maximum between June and August [Quinn and Bates, 2003]. There is little variation in τ_a or AI over the remote Pacific, with values much less than those observed in continental outflow, as expected.

[14] The differences between τ_a and AI provide an indication of whether aerosol are present mainly in the coarse ($> 1\mu m$) or fine ($< 1\mu m$) mode as the AI is sensitive to the aerosol fine mode fraction whilst AOD is more sensitive to coarse mode aerosol, as explained above. $AI = AOD \times A$, so where AOD equals AI, A equals 1, and fine mode aerosols dominate. Figure 2.2 shows that τ_a is elevated above AI over the western Pacific in late spring when there is strong outflow from the Asian continent that typically includes mineral dust transport events [Kim et al., 2007; NOAA, 2007]. A similar discrepancy between τ_a and AI occurs over the equatorial Atlantic downwind of the Sahara throughout the year but is most pronounced between February and April, consistent with measurements of the aerosol index at UV wavelengths made by the Total Ozone Mapping Spectrometer (TOMS). In contrast, North American outflow over the Atlantic shows similar values for τ_a and AI, suggesting the fine aerosols dominate that outflow. Variation of r_e depends on region. The smallest $r_e$values occur over the eastern Atlantic coincident with large increases in τ_a. In general, regions that include continental outflow show a negative relationship between τ_a or AI and r_e consistent with the Twomey IE. The region downwind of southern Africa shows the strongest anti-correlation between AI and r_e (r = -0.64). For other regions the correlation between τ_a or AI and r_e over 1997 is much weaker (Table 1), partly due to the seasonal nature of continental outflow from many regions.

[15] Similar anti-correlations could be generated from systematic sampling errors. Erroneous cloud flagging, identifying high aerosol loading as cloudy pixels, would result in very low values

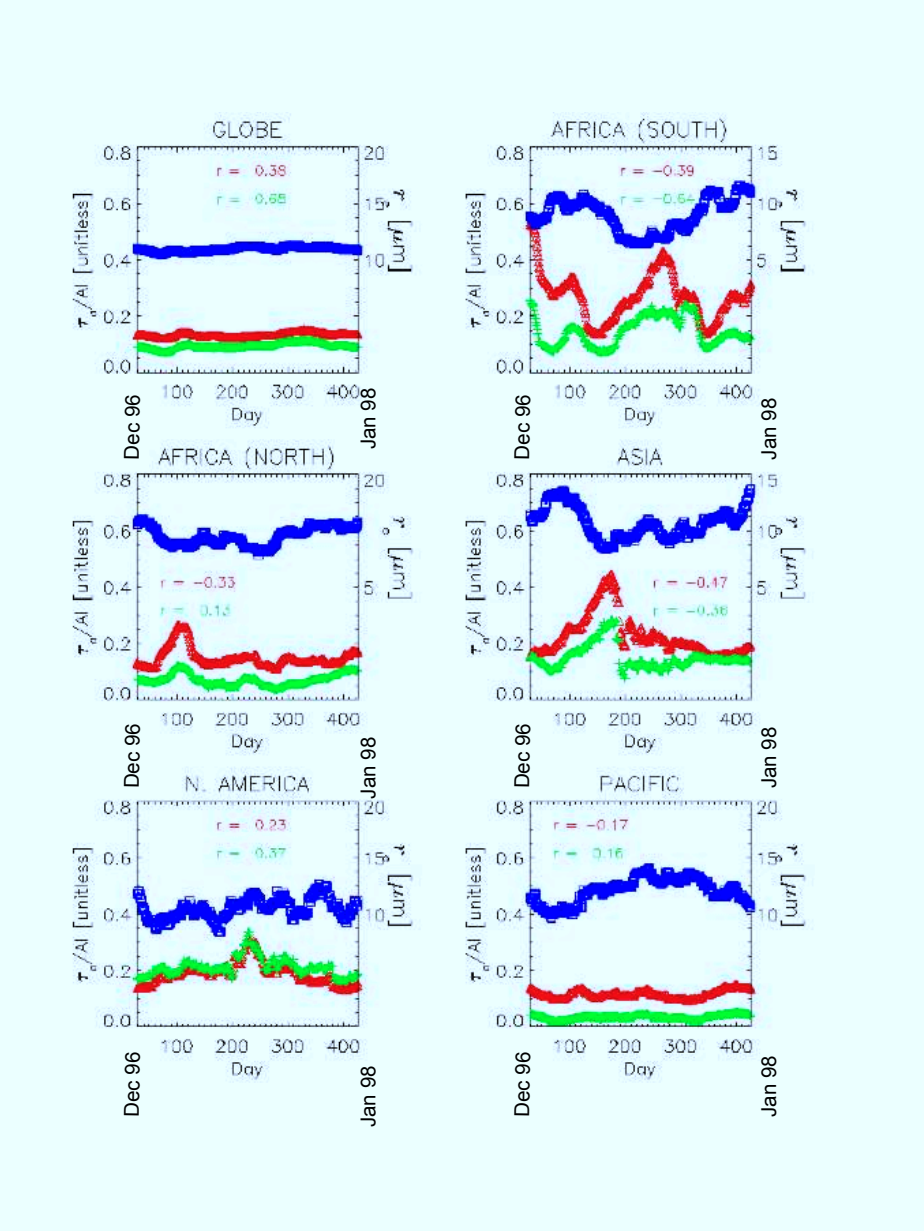

Figure 2.2: 28-day rolling mean of τ_a at 0.55 μm (red) and r_e (μm, blue) observed by ATSR-2 between 1st December 1996 and 31st January 1998 over the globe, eastern South Atlantic (Africa (South)), eastern equatorial Atlantic (Africa (North)), western North Pacific (Asia), western North Atlantic (North America), and the South Pacific (control case). AI (green) is calculated using offline extinction coefficients at 0.55 μm and 0.67 μm. Standard errors ($\sigma/\sqrt{(n-2)}$) are superimposed on the time series but are close to zero. Correlation coefficients between τ_a/AI (red/green) and r_e are given in each panel.

of r_e with elevated τ_a. It is likely that such a situation would be identified by a bi-modal distribution in r_e measurements, with a secondary peak at low r_e generated by erroneously classified aerosol data, which is not observed in the GRAPE data. Aerosol and cloud layers may be decoupled across a frontal system or if the atmosphere is vertically stable [Sinha et al., 2003] and in such situations anti-correlations between τ_a and r_e do not signal a causal relationship. However, coastal regions, the focus of this study, are typified by low-level cloud and experience cycling between stratiform and cumuliform cloud layers [Paluch and Lenschow, 1991] so we expect aerosol and cloud properties to be related over the spatial scales studied.

[16] The Twomey IE can be described as the relative change in r_e associated with a relative change in τ_a [Feingold et al., 2001]: $-\partial ln\, r_e / \partial ln\, \tau_a$. Assuming a homogeneous cloud with a constant LWP, the relationship between cloud droplet number (N_d) and the aerosol number concentration (N_a) is nonlinear: $N_d \propto N_a^{\alpha}$, where α is a unitless parameter that provides an indication of particle hygroscopicity, with low values corresponding to low hygroscopicity. A characteristic α value adopted by several previous studies is 0.7 [Bréon et al., 2002; Feingold et al., 2003]; below, we look at the sensitivity of α to the interpretation of our results. As previously discussed, AI may provide a better proxy for N_a [Bréon et al., 2002; Quaas et al., 2004], but our analysis concentrates on τ_a because AI is not a GRAPE retrieval product. It can be shown that $r_e \propto \tau_a^{-\alpha/3}$ [Feingold et al., 2003] so using $\alpha = 0.7$ gives IE $= \alpha/3 \approx 0.23$.

[17] Table 2.1 shows the seasonal mean values of IE and the associated correlation (r) between τ_a and r_e for the defined regions. The gradients are calculated for τ_a between 0.13 and 0.4 with r_e averaged over τ_a increments of 0.03, accounting for the standard error of the measurements in each size bin. Values of $\tau_a > 0.4$ are noisy, due to few observations above this threshold, with the exception of southern Africa where aerosol loading during the burning season is much greater than in other regions; consequently we calculate IE for between 0.35 and 1.5 for DJF and JJA.

[18] A physical condition of the assumed relationship between N_d and N_a is $\alpha \leq 1$ so that $0 \leq IE \leq 0.33$. On a global scale, GRAPE data yields seasonal mean IE values between 0.10 and 0.16 corresponding to values of α ranging from 0.30 to 0.48. The theoretical value of IE $= 0.23$ (assuming $\alpha = 0.7$) is based only on the physical relationship between aerosol number

and cloud droplet number, disregarding other important physical processes including aerosol size distribution and updraft velocity [Feingold et al., 2001]. Previous studies have shown a similar range of IE values when using this assumption [Feingold et al., 2003].

[19] Over the western North Atlantic, IE is strongest in JJA when continental outflow is greatest. Over the western North Pacific the strongest IE is not observed during the period of maximum outflow (MAM) when mineral dust is prevalent [Kim et al., 2007] but during DJF/SON when dust does not dominate the outflow. Over the eastern South Atlantic we find evidence of the IE duing DJF, JJA, and SON; there is only a small amount of active burning during MAM [ESA, 2004]. During JJA, we find the IE is 0.51, implying an unphysical value of $\alpha > 1$. The high correlation coefficient (-0.85) associated with this season suggests that the observed relationship is not due to noisy data. In regions of high aerosol loading using the assumption $N_d \approx N_a^{\alpha}$ may be an oversimplification. Feedback mechanisms associated with drizzle suppression at the base of the cloud result in increased air entrainment from above the cloud. Aerosol entrainment and activation may be enhanced depending on the humidity of air above the cloud and the consequent effect on the LWP [Ackerman et al., 2004]. During DJF we use the equatorial region to study African burning outflow as noted above. Significant IE is found both here and in the adjacent outflow region downwind of the Sahara desert, and we conclude that it is difficult to separate dust and burning outflow in this region although burning is more likely responsible for the IE in this season. A weak IE is seen in the adjacent Saharan region during JJA.

[20] There are of course limitations to the theory outlined in *Twomey* [1974] and the analysis approach we adopt in this paper, which we outline below. Recent work has highlighted that the Twomey theory describes only the physical relationship between aerosol number and cloud microphysics [Feingold et al., 2001, 2003]. Other physical effects are not taken into account, most notably aerosol size distribution, which is estimated to describe $\sim 80\%$ of the variability in aerosol activation [Dusek et al., 2006]. Although thought to take a secondary role, aerosol chemical composition is also important in determining α and hence IE [Dusek et al., 2006]. Aerosols must be hygroscopic in order to act as CCN; hydrophobic aerosol types such as desert dust need to obtain a hydrophilic coating (eg. sulphur or organics). Smaller aerosols from industrial sources and biomass burning that contain organic species tend to be hygroscopic and more immediately

effective as CCN [Seinfeld and Pandis, 1998].

[21] The Twomey hypothesis is based on the assumption that the cloud layer has a homogenous LWC. Over the spatial scales measured by the satellite these assumptions are unlikely to be valid: cycling between stratus layers and cumuli clouds will lead to inhomogeneity [Paluch and Lenschow, 1991]. Air circulation within the cloud, possibly modified by aerosol feedback mechanisms, will also result in changing LWC [Ackerman et al., 2004]. The uncertainties in the derived IE values in Table 2.1 are likely to be underestimated because we do not account for variations in LWC over the spatial scales studied. Despite the many assumptions we have made our results are quantitatively consistent with theory at a global scale, and regionally consistent during period of high continental outflow.

[22] **Acknowledgements.** CEB is supported by NERC DARC studentship NER/S/D/2006/14345, and via additional support from the Rutherford Appleton Laboratory. The Oxford authors wish to acknowledge NERC funding NER/T/2001/00205 and NE/B503933/1.

2.6 Supplementary Material - Extended Discussion

Given the formatting requirements for the submission of this paper to Geophysical Research Letters the discussion section of the paper was limited in length so here I expand on some of the details that I was unable to include in the paper. Figure 2.3 and Figure 2.4 show monthly plots of r_e against τ_a over the globe and across the Saharan region, and from these data the IE in Table 2.1 is calculated. The African data is only for the upper analysis box (1a) for the Saharan region (shown in Figure 2.1), and consequently there is no evidence of the IE during DJF in this plot. Across the globe there is an inverse relationship between τ_a and r_e during every month. Over Africa this relationship shows more seasonal variation, being most significant during June and July, and during JJA we find an unphysical IE value of 0.51 +/- 0.16. We also see data with higher τ_a than in other regions explaining the shift in the τ_a range over which IE is calculated for this region. As stated in the main paper, a lower limit of τ_a = 0.13 was placed on the calculation of IE. From the global data it can be seen that this value is a critical threshold below which τ_a is not inversely correlated with r_e. The reason for this is unclear from the work undertaken here but may be related to moisture availability in the cloud. For low τ_a, there may be enough available

moisture to activate new droplets without the competition for water that occurs during the first indirect effect, reducing cloud droplet size.

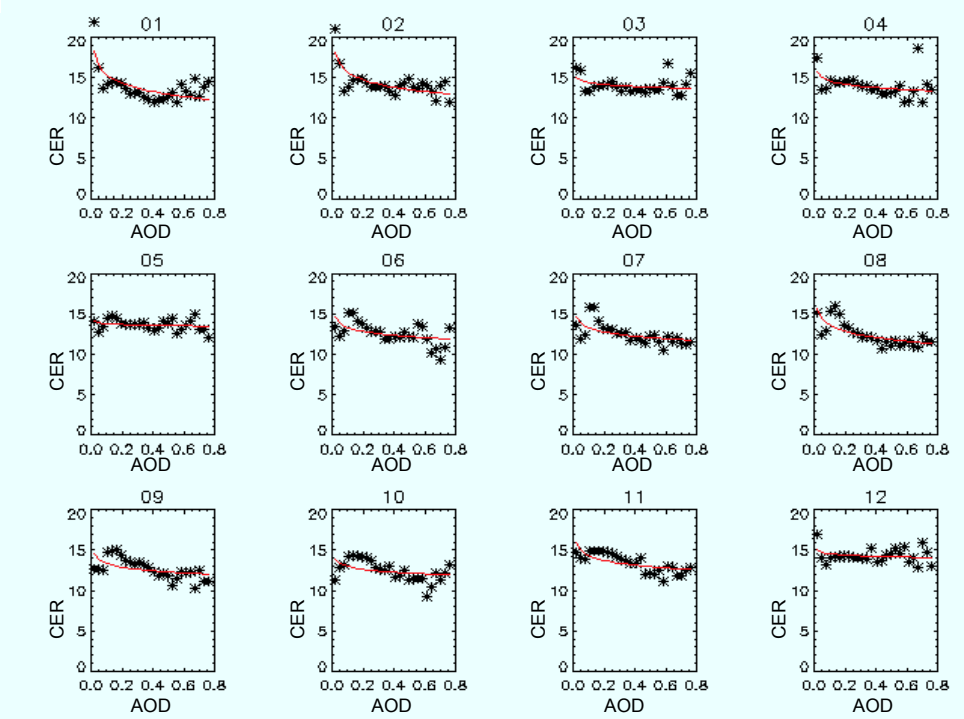

Figure 2.3: Monthly correlation between cloud effective radius (r_e) and aerosol optical depth (τ_a) across the globe during 1997.

Another important factor discussed only briefly in the paper is LWC. Although droplet activation is dependent upon aerosol particle size and chemical composition, the number of new cloud droplets created cannot exceed the number of aerosol particles available as suggested by the unphysical IE value seen over Africa during JJA. It should be noted that r_e is correlated against τ_a, which is a proxy for aerosol amount rather than a direct measure of the number concentration. However, the reason for this unphysical measure of IE is likely to be related to meteorological feedbacks as a function of the aerosol-cloud interaction. A reduction in cloud droplet size caused by aerosol could inhibit precipitation [Albrecht, 1989], which may in turn increase air entrainment from above the cloud [Ackerman et al., 2004]. This air may also contain aerosol and lead to further cloud droplet activation increasing the apparent magnitude of the IE when evaluated

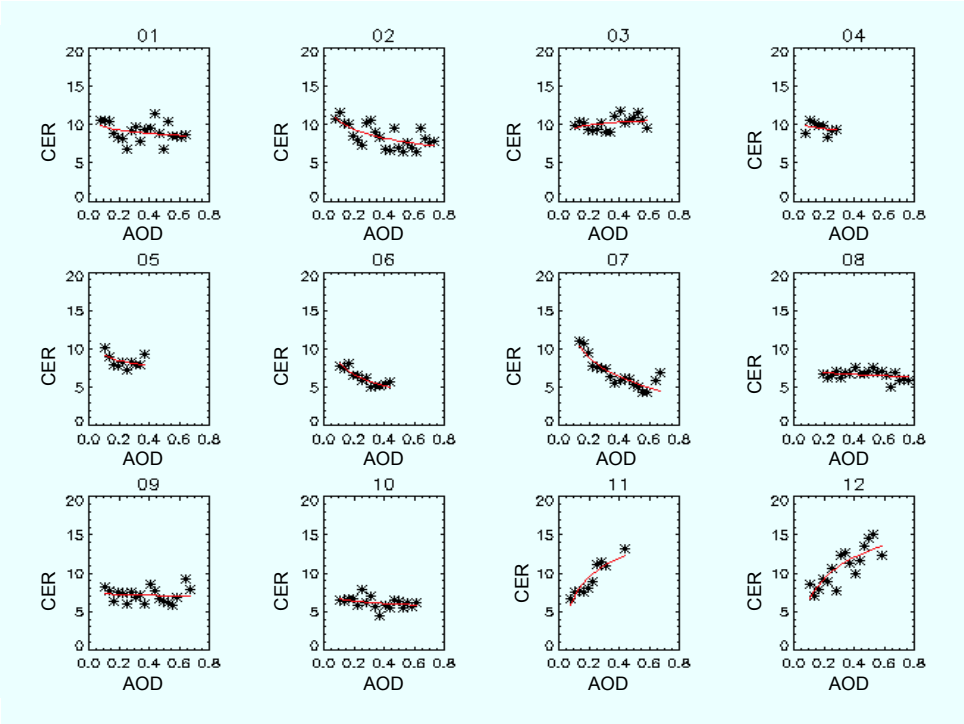

Figure 2.4: Monthly correlation between cloud effective radius (r_e) and aerosol optical depth (τ_a) across the the Sahara (box 1a only) during 1997.

over these spatial and temporal scales. Enhanced air entrainment could be identified by changes in the LWC which is assumed to remain constant in the definition of the Twomey indirect effect. LWC data was available from the GRAPE dataset, but as I was evaluating monthly mean values it would not capture immediate changes in cloud LWC in response to aerosol loading making it difficult to test this hypothesis. Studies using data from other research platforms, particularly aircraft campaigns, would be necessary to fully investigate the response of cloud LWC to aerosol loading, which would be dependent on the aerosol size distribution, loading, chemical composition and local meteorology.

Chapter 3

Quantifying the Response of the ORAC Aerosol Optical Depth Retrieval for MSG SEVIRI to Aerosol Model Assumptions[1]

3.1 Declaration

With the exception of the comparison between the SEVIRI ORAC retrieval and AERONET data from the Cape Verde and Ascension Island sites, which was carried out by Andy Sayer, the work done in this chapter is all my own. Paul Palmer, Chris Merchant and Richard Siddans are all acknowledged as my supervisors, and Chris Merchant for his work in developing the Saharan Dust Index. Richard Siddans, Caroline Poulsen, Gareth Thomas, Andy Sayer, Elisa Carboni and Roy Grainger have all been involved in the development of the ORAC retrieval algorithm. Siegfried Gonzi wrote the code used to compare GEOS-Chem carbon monoxide profiles with TES observations, and Ellie Highwood and Claire Ryder were involved in gathering data during the DODO aircraft campaign.

[1] Claire E. Bulgin, Paul I. Palmer, Christopher J. Merchant, Richard Siddans, Siegfried Gonzi, Caroline A. Poulsen, Gareth E. Thomas, Andrew M. Sayer, Elisa Carboni, Roy G. Grainger, Ellie J. Highwood, Claire L. Ryder - Accepted for publication by the Journal of Geophysical Research Atmospheres, May 2010.

3.2 Abstract

We test the response of the Oxford-RAL Aerosol and Cloud (ORAC) retrieval algorithm for MSG SEVIRI to changes in the aerosol properties used in the dust aerosol model, using data from the Dust Outflow and Deposition to the Ocean (DODO) flight campaign in August 2006. We find that using the observed DODO free tropospheric aerosol size distribution and refractive index compared with the dust aerosol properties from the Optical Properties of Aerosol and Cloud (OPAC) package, increases simulated top of the atmosphere radiance at 0.55 μm assuming a fixed aerosol optical depth of 0.5 by 10–15 %, reaching a maximum difference at low solar zenith angles. We test the sensitivity of the retrieval to the vertical distribution of the aerosol and find that this is unimportant in determining simulated radiance at 0.55 μm. We also test the ability of the ORAC retrieval when used to produce the GlobAerosol dataset to correctly identify continental aerosol outflow from the African continent and we find that it poorly constrains aerosol speciation. We develop spatially and temporally resolved prior distributions of aerosols to inform the retrieval which incorporates five aerosol models: desert dust, maritime, biomass burning, urban and continental. We use a Saharan Dust Index and the GEOS-Chem chemistry transport model to describe dust and biomass burning aerosol outflow, and compare AOD using our speciation against the GlobAerosol retrieval during January and July 2006. We find AOD discrepancies of 0.2–1 over regions of intense biomass burning outflow, where AOD from our aerosol speciation and GlobAerosol speciation can differ by as much as 50 - 70 %.

3.3 Introduction

The magnitude and distribution of radiative forcing from aerosols represents one of the largest uncertainties in understanding Earth's climate [Forster et al., 2007]. Aerosols affect climate directly by scattering and absorbing solar radiation, and indirectly by modifying cloud microphysical properties. They have a diverse range of natural and anthropogenic sources including desert dust, sea salt, and incomplete fuel combustion leading to different optical properties for each aerosol type. The atmospheric lifetime of these aerosols, determined by size (gravitational settling and uplift size distribution), hygroscopicity (rainout and washout), chemical reactivity (heterogenous chemistry), and meteorology, is of the order of several days. The resulting large spatial and tem-

poral variations in the loading and chemical composition of aerosols are sampled only sparsely by surface and aircraft measurements but are of significant climatic importance. We focus here on aerosol observed by the Spinning Enhanced Visible and InfraRed Imager (SEVIRI), dominated by dust and biomass burning outflow from the African continent. These aerosols have direct and indirect effects on climate, altering the radiative balance and cloud properties which can lead to a reduction in precipitation and sea surface temperature [Huang et al., 2009; Foltz and McPhaden, 2008]. Dust deposited over the ocean can also stimulate phytoplankton production [Mills et al., 2004]. Satellite observations provide global measurements of aerosol optical properties (e.g., aerosol optical depth) which are invaluable for improving global quantitative understanding of aerosols and their climate impacts. However, current instruments do not provide enough information to fully constrain aerosol properties eg. size and absorption capability and thus aerosol retrievals rely heavily on *a priori* assumptions [Kokhanovsky et al., 2010].

Aerosol optical properties are retrieved from satellites by fitting simulated radiances to observed radiances. Simulated radiances are determined using a radiative transfer model that makes prior assumptions about the surface and atmospheric state (e.g., surface reflectance, aerosol types and associated size distributions). We examine aerosol optical depths (AODs) retrieved from the Spinning Enhanced Visible and Infrared Imager (SEVIRI) aboard the geostationary Meteosat Second Generation-2 (MSG-2) satellite centred over Africa. We retrieve AOD using the Oxford-Ral Aerosol and Cloud (ORAC) optimal estimation scheme (described in section 3.4), and use these data to understand continental outflow of aerosols over the Atlantic. In recognition of the fact that the assumed aerosol type will affect the retrieved AOD, the ORAC scheme performs retrievals for each scene for a range of different aerosol types. To assign a “best-type” a number of type-specific quality control measures are applied including the quality of fit to the observed radiance (ie. the cost function). However it was recognised that the skill of this method in distinguishing aerosol type (especially those with similar optical properties) would be limited. Here, we develop a temporally and spatially resolved speciation to inform the ORAC retrieval.

The results we present are split into two complementary sections: a) in section 3.5 we use detailed aircraft observations to evaluate the aerosol size distribution shape, refractive index, and aerosol vertical distribution assumed by ORAC in Saharan dust outflow over the Atlantic and

quantify the impact of these assumptions and solar geometry on the simulated radiance and resulting AOD retrievals; and b) in section 3.6 we develop a new seasonal aerosol speciation using the brightness temperatures from SEVIRI to provide information about dust, and output from a chemistry transport model to provide information on the transport of biomass burning aerosol outflow. We quantify the impact of these new speciation distributions on retrieved AOD in section 3.7 and conclude the paper in section 3.8.

3.4 SEVIRI Instrument and ORAC Algorithm Description

3.4.1 SEVIRI

SEVIRI aboard the MSG-2 satellite was launched at the end of 2005 in an equatorial geostationary orbit centred over Africa and makes observations every fifteen minutes. SEVIRI measures reflected solar and emitted infrared radiation in eleven spectral channels centred near 0.6, 0.8, 1.6, 3.9, 6.2, 7.3, 8.7, 9.7, 10.8, 12, and 13.4 μm, with a spatial resolution of 3×3 km in the nadir which gets coarser with distance from the nadir [Schmetz et al., 2002]. SEVIRI also has a broadband high resolution visible channel covering the 0.5 – 0.9 μm spectral band giving data with a spatial resolution of 1×1 km in the nadir.

3.4.2 The ORAC Retrieval Scheme

ORAC retrieves AOD, aerosol effective radius and surface albedo using the 0.6, 0.8 and 1.6 μm SEVIRI radiances. It uses an optimal estimation approach, varying all retrieved parameters simultaneously, to calculate the retrieved state with the maximum probability, whilst accounting for both measurements and *a priori* data and uncertainties in both [Rodgers, 2000]. It uses the DIScrete Ordinances Radiative Transfer model (DISORT) [Stammes et al., 1988] to calculate top of the atmosphere (TOA) radiance as a function of the properties of a plane parallel aerosol or cloud layer with an assumed height distribution. The retrieval scheme was originally developed for clouds [Watts et al., 1998] and applied to data from the Along Track Scanning Radiometer (ATSR), and later extended to aerosol retrievals from ATSR [Marsh et al., 2004] and other instruments. A full description of the ORAC retrieval scheme can be found in Thomas et al. [2009a].

The ORAC forward model, **F**, consists of four separate elements: 1) a model of aerosol scattering and absorption; 2) a model of atmospheric gas absorption; 3) a model of atmospheric radiative transfer; and 4) a model of surface reflectance [Thomas et al., 2007], which uses aerosol optical properties calculated offline to interpret the observed radiances. The optical properties used in the aerosol model (aerosol phase function, extinction and scattering coefficients) are calculated using Mie theory from prior information about aerosol size distributions and refractive indices from observations and modelling studies [Hess et al., 1998; Dubovik et al., 2002]. These properties are calculated as a function of aerosol effective radius, ranging between 0.01 – 10 μm, by varying the mixing ratio of the different components within each aerosol type. These are collected together within the model in a series of look-up tables (LUTs) describing atmospheric transmission and reflectance, for radiance and AOD calculations.

The forward model is fitted to the observed radiances by minimising a cost function J(**x**) which describes the quality of fit between the observed radiances (the measurement vector **y**) and modelled radiances, the state vector **x** and the *a priori* state vector $\mathbf{x}_a$:

$$\mathrm{J}(\mathbf{x}) = (\mathbf{F}(\mathbf{x}) - \mathbf{y})\mathbf{S}_y^{-1}(\mathbf{F}(\mathbf{x}) - \mathbf{y})^{\mathrm{T}} + (\mathbf{x} - \mathbf{x}_a)\mathbf{S}_a^{-1}(\mathbf{x} - \mathbf{x}_a)^{\mathrm{T}} \tag{3.1}$$

where $\mathbf{S}_y$ and $\mathbf{S}_a$ are the error covariance matrices for the measurement vector and the *a priori* state vector, respectively. *A priori* and measurement errors are assumed to be normally distributed with zero mean, and variance determined by measurement and forward model noise ($\mathbf{S}_y$) and *a priori* error ($\mathbf{S}_a$) [Thomas et al., 2007]. ORAC uses the Levenberg-Marquardt algorithm to minimise the cost function and subsequently identify the state vector that is most consistent with $\mathbf{x}_a$, **y**, $\mathbf{S}_y$, and $\mathbf{S}_a$ [Thomas et al., 2009a]. T denotes a matrix transpose. The problem is moderately non-linear with the number of required iterations generally below the upper limit of 25, a number indicative of a failed retrieval [Thomas et al., 2009b].

We limit our analysis of AOD to ocean scenes where low surface albedo at wavelengths of interest make it easier to separate surface reflectance from the aerosol signal in the retrieval and we use a fixed spectral shape to describe ocean reflectance [Thomas et al., 2005]. Cloudy scenes are removed prior to fitting using the EUMETSAT cloudmask derived using reflectance, temperature,

snow and ice tests at the full SEVIRI spatial resolution [Thomas et al., 2005], and a spatial coherence test is used to remove spatially isolated high AOD under the assumption that this is cloud.

The ORAC scheme uses five aerosol models: continental, urban, maritime, desert dust and biomass burning. Each model is constructed from a number of lognormally distributed aerosol components with different modal radii and spread. The mixing ratios of each component of the aerosol *a priori* are varied to allow aerosol effective radius to range between 0.01 and 10 μm in the retrieval. Desert dust, maritime, urban and continental aerosol are defined using refractive index and component size distribution data from the Optical Properties of Aerosols and Clouds (OPAC) package [Hess et al., 1998]. For biomass burning aerosol, these properties are defined from three years of in situ data from the AErosol RObotic NETwork (AERONET) [Dubovik et al., 2002].

The retrieval assumes spherical particles for all aerosol classes and aerosol optical properties are derived using Mie theory. Previous research has shown that this assumption is unlikely to be correct for dust particles eg. [Otto et al., 2009; Zhao et al., 2003], although dust particle shape is at present poorly constrained and the information content of current retrievals is often insufficient to distinguish between spherical and non-spherical particles [Wang et al., 2003]. The assumption of spherical dust particles was used in the GlobAerosol product (Section 3.4.3) and provides consistency with the derivation of aerosol optical properties from DODO measurements. It is also used in most other well-known aerosol retrieval schemes for instruments such as the Moderate Resolution Imaging Spectroradiometer (MODIS) [Remer et al., 2006], with the exception of Multiangle Imaging Spectroradiometer (MISR) which has the ability to resolve scattering at multiple angles [Diner et al., 2008].

3.4.3 GlobAerosol Data Product

GlobAerosol was a project to develop a merged global AOD dataset between 1995–2007 using instruments on a number of European satellite platforms; ATSR-2, the Advanced Along Track Scanning Radiometer (AATSR), the Medium Resolution Imaging Spectrometer (MERIS) and SEVIRI. The SEVIRI AOD is derived using the ORAC retrieval algorithm on a 10×10 km equal-area sinusoidal grid. GlobAerosol uses the retrieved aerosol optical properties for each of the five

aerosol models included in the ORAC retrieval because there is not sufficient information in the retrieval to unambiguously identify aerosol type. The "best" retrieved aerosol type is determined by the smallest retrieval cost following quality control, as defined above. Costs for different aerosol classes can be similar thereby compromising this approach.

In Section 3.5 we test the sensitivity of the retrieval to the defined aerosol *a priori*, a requirement for evaluating the robustness of long-term datasets used to define aerosol radiative forcing. Other well-known retrieval schemes for instruments including MODIS and MISR take a similar approach to ORAC using predefined aerosol models and prior climatological probabilities [Diner et al., 1999, 2008] or a mixture of coarse and fine mode particles [Remer et al., 2006] to model retrieved radiance. Our work therefore has a wider application beyond the ORAC scheme to many satellite retrieval schemes.

3.5 Sensitivity of ORAC to A Priori Optical Properties and Viewing Geometry

The purpose of this section is to test the robustness of the assumptions about dust aerosol used in the ORAC scheme, including size distribution, refractive index, phase function and vertical distribution; and how sensitive the simulated radiance is to changing these assumptions. Previous studies have highlighted the importance of particle size distribution and refractive index to simulated top of the atmosphere (TOA) radiance and retrieved aerosol optical depth [Liao and Seinfeld, 1998; Durant et al., 2009; Martonchick et al., 2002]. Retrieval sensitivity to these parameters is dependent on the aerosol model assumption used and needs to be evaluated independently for any algorithm from which aerosol forcing is to be calculated. We achieve this for the ORAC scheme using relatively sparse but detailed data from the Dust Outflow and Deposition to the Ocean (DODO) aircraft campaign described below. We also assess the sensitivity of the retrieved AOD to the viewing geometry, and compare the DODO AOD and aerosol effective radius with data from the retrieval.

3.5.1 Brief Description of the DODO Aircraft Campaign Data

The DODO aircraft campaign took place over Western Africa and the Eastern tropical Atlantic during February and August 2006 with the aim of quantifying iron deposition to the ocean, and was affiliated with the African Monsoon Multidisciplinary Analysis (AMMA) project [McConnell et al., 2008; Rajot et al., 2008]. We use data collected during August 2006 when the FAAM BAe146 aircraft was based in Dakar, Senegal, making in-situ and remote airborne measurements of dust aerosol. Aerosol size distribution was measured using the Passive Cavity Aerosol Spectrometer Probe (PCASP) and the Cloud Droplet Probe (CDP) and we refer the reader elsewhere for a more detailed description of the data collection [McConnell et al., 2008].

We use DODO aircraft measurements of aerosol properties averaged across horizontal flight paths (referred to as 'runs' abbreviated to 'R') covering between 30–200 km, or as vertical profile data (abbreviated to 'P') extending from $\sim$50 m to a maximum altitude of 6 km, above which aerosol concentrations were negligible. Data from the PCASP and CDP instruments together provide aerosol size distributions at 0.55 μm over the 0.05–20 μm radius size interval in both the horizontal runs and vertical profiles. We also use refractive indices from DODO, inferred from Mie scattering calculations, which are only available at 0.55 μm [McConnell et al., 2008, 2010]. We use the size distributions and refractive indices in offline Mie scattering calculations to generate aerosol optical properties including aerosol effective radii, phase function and extinction coefficients from both the horizontal run and vertical profile data. The largest uncertainties with the measured size distribution will relate to coarse mode aerosol as data from the CDP is less well validated [McConnell et al., 2008]. At visible wavelengths these particles are likely to be predominantly scattering and these measurement errors may affect the magnitude of the forward scattering peak in the phase function but should have a small impact on the radiance calculation.

For this paper, we use data from three flying days during the DODO campaign and focus first on the horizontal run data. Flights are labelled with a prefix 'b' and a flight number. We use data from flight b237 (22nd August, 2006) runs R1, R3, R4, R5, R6, R7; flight b239 (24th August, 2006) runs R1, R2-4, R5, R6; and flight b241 (25th August, 2006) R2. All flights sampled free tropospheric aerosol between 800–500 hPa, with the exception of flight b237 runs R4 and R5, which sampled boundary layer aerosol at approximately 1000 hPa. From this point on we will

distinguish between the free troposphere (FT) and boundary layer (BL) data. Further details of the flight tracks are given by McConnell et al. [2008].

3.5.2 Aerosol Size and Mass Distribution

Figure 3.1 (a) shows observed FT and BL aerosol size distributions, and (b) mass distributions calculated assuming a dust density of 2.65 g cm^{-3} [Tegen and Fung, 1995], on 22nd August 2006 during DODO. The aerosol modal radii in the FT is $<$0.1 μm, above which number concentration decreases with increasing aerosol radius. BL concentrations of fine mode aerosol ($<$0.1 μm radius) are five times larger than those in free tropospheric air; there are also more large particles (2.5–4 μm radius) present in the BL number although total aerosol number concentrations are greater in the FT. Figure 3.1b shows that BL aerosol mass distribution peaks below 0.2 μm radius and between 2–5.5 μm radius; in contrast, most of the FT aerosol mass is between 0.02–2 μm radius. Coarse mode aerosol ($>$1μm radius) is lost from the FT due to gravitational settling. Observed variations in aerosol distribution may also reflect different source regions. Ten-day back trajectories from the location of the DODO flights using the NOAA HYSPLIT model [Draxler and Rolph, 2010] (not shown), and five day back trajectories using the NAME model [McConnell et al., 2010] indicate that sampled air masses over the Atlantic have a range of potential geographical sources including Libya, Algeria, Mauritania and the Western Sahara.

Figure 3.1c compares typical observed DODO and ORAC aerosol model size distributions in the FT and BL matched using the DODO aerosol number concentration and effective radius. Effective radius is not fixed in the retrieval; however the lognormal distribution $n(r)$ for each of the components in the assumed aerosol model is defined as:

$$n(r) = \frac{N_0}{\sqrt{2\pi}} \frac{1}{ln(s)} \frac{1}{r} \exp\left[-\frac{(ln(r) - ln(r_m))^2}{2ln^2(s)}\right], \tag{3.2}$$

where N_0 is the total number concentration, r_m the median radius of the aerosol, and s is the spread of the distribution, where $\sigma(ln(\mathbf{r})) = ln(\mathbf{s})$). We find that the observed DODO number distributions at radii $>$0.05 μm, based on data from a FT and a BL flight, are greater than the ORAC aerosol models. The ORAC dust and maritime aerosol size distributions are similar, whilst the biomass burning aerosol is characterised by fewer fine mode particles ($<$ 0.045 μm) and higher number concentrations between 0.045–0.3 μm radius. We acknowledge that the lower detection

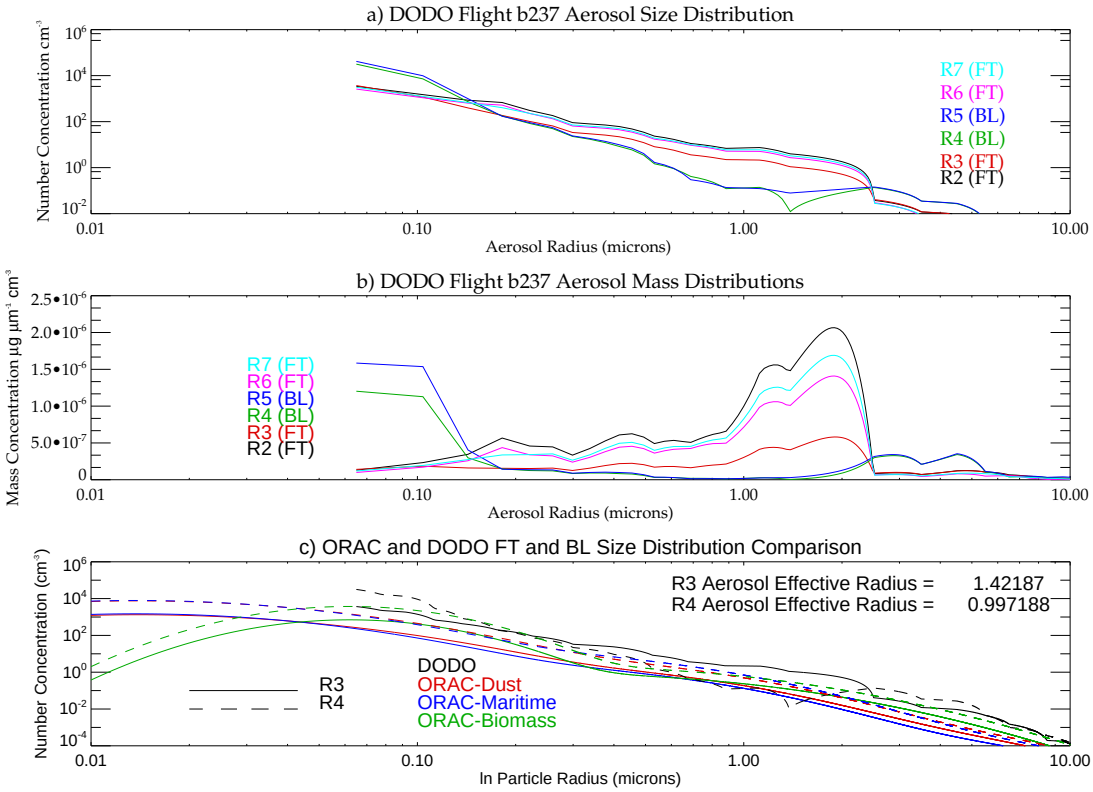

Figure 3.1: Observed a) aerosol number (cm^{-3}) and b) mass distributions (μg μm^{-1} cm^{-3}) as a function of aerosol radius (μm) for DODO flight b237, 22nd August 2006; and c) observed aerosol size distributions for typical boundary layer and free troposphere conditions during DODO, with the corresponding OPAC model values for dust (red), maritime (blue), and biomass biomass burning (green) aerosol. OPAC aerosol model data are matched to the DODO data using the DODO aerosol effective radii and number distribution.

limit of 0.05 μm radius in the DODO data may bias these comparisons as they are based on the total aerosol number concentration.

3.5.3 Scattering Phase Functions

Figure 3.2 compares aerosol phase functions calculated using the DODO size distributions and refractive index, and the ORAC dust model, matched using the DODO aerosol effective radius. They have been compared for aerosol effective radii from two flights indicative of FT and BL data at 0.55 μm. We accept that FT and BL aerosol properties cannot be distinguished between in the retrieval and only column values can be determined, but separating these data here gives a range of observed size distributions to test retrieval sensitivity. In the FT, ORAC and DODO phase functions are almost identical except at near-backscattering angles (160° –180°) where DODO data shows a double peak in scattered light intensity with a maximum difference in magnitude of 0.3. The additional observed peaks in the phase function may reflect the noisier distribution of aerosol

particles with radii <0.1 μm than described by the ORAC distribution. DODO backscattered radiation intensity may also be limited by the lower observation limit of 0.05 μm radius. In the BL, a similar feature is seen a near-backscattering angles. DODO data also shows greater scattering between 50–100° with an absolute difference of 0.1, and a sharper forward scattering peak observed between 0–8° compared with 0–15° for the DODO data. We also find that the DODO observations have a significantly higher single scattering albedo (0.94–0.98) than the ORAC model (0.87–0.89) which is taken from OPAC [Hess et al., 1998]. We recalculate the phase function using the DODO size distribution and the ORAC complex refractive index (not shown). For both distributions the real part of the refractive index is the same with a value of 1.53. We find that the discrepancy in the single scattering albedo can be attributed to the much lower DODO imaginary refractive index (0.0018(R3), 0.0003(R4)) compared to 0.0055 in the ORAC model. In the retrieval the dust aerosol is assumed to be more absorbing than the dust sampled during DODO and other aircraft campaigns [McConnell et al., 2008; Osborne et al., 2007].

3.5.4 Viewing Geometry

Observed aerosol radiances are influenced by the sun-instrument geometry because the aerosol phase function is dependent on the angle of observation. Here we use the ORAC forward model (section 3.4.2) to test the sensitivity of the simulated radiance to scattering angle as a function of solar zenith angle (SZA). Figures 3.3 and 3.4 show TOA model radiances simulated using DODO observations and the ORAC dust aerosol model between 0800–1745 local time. We match the ORAC aerosol effective radius to the observed DODO effective radius and assume a fixed aerosol optical depth of 0.5. We compare the difference in simulated TOA radiance between the ORAC and DODO models using the DODO size distribution and DODO refractive index (Figure 3.3), and the DODO size distribution with the ORAC refractive index (Figure 3.4). Radiances are calculated in a pseudo 0.55 μm channel, generated to match DODO observations with the ORAC model, as SEVIRI does not make observations at this wavelength. Profiles of atmospheric temperature, water vapour and ozone for each retrieval are taken from the European Centre for Medium-range Weather Forecasting (ECMWF). In both cases, simulated radiances peak between 1200–1400 local time at a scattering angle of $\sim$150°, which is as expected given that the phase function intensity peaks at near-backward scattering angles.

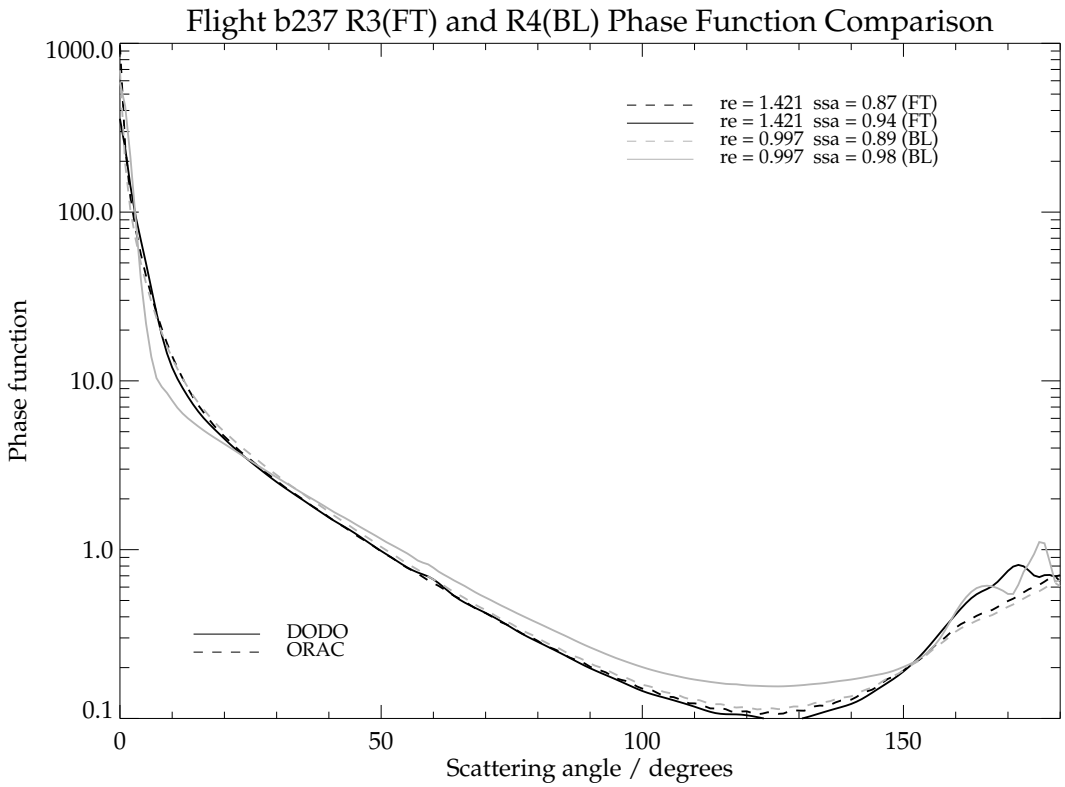

Figure 3.2: Phase functions at 0.55 μ m derived from DODO observations (solid line) and ORAC dust model (dashed line) phase functions on the 22nd August 2006, which is representative of the conditions found for the boundary layer and the free troposphere during the DODO aircraft campaign. The model correspondence to the data is determined by the observed aerosol effective radii. The single scattering albedo is given for the DODO and ORAC data.

Figure 3.3 shows that radiances simulated using the DODO size distribution and refractive index are generally larger than those derived using the ORAC dust model. In the FT, the DODO observations are $\sim$10% higher than ORAC values before midday and after 1400, increasing to $\sim$15% between those times. In the BL, the bias is $\sim$25% during the morning and afternoon, decreasing to $\sim$20% when the sun is overhead. FT phase function differences between DODO and ORAC are most pronounced at near-backscattering angles. BL data shows greater scattering by DODO aerosol between 100°–150° as well as between 160°–180° explaining the larger DODO radiances throughout the day. We find that this difference in retrieved radiance is sensitive to changes in AOD, increasing by $\sim$ 2-4 % between an optical depth of 0.4–0.6. We acknowledge that Mie code assuming spherical particles may not define the dust phase function correctly and suggest that variance in modelled radiance with SZA using this regime should not be over-interpreted.

From the comparison using the ORAC refractive index with the DODO size distribution (Figure 3.4) we find that the systematic high bias in the DODO simulated radiance can be attributed to the lower imaginary refractive index. When we use the ORAC refractive index we find that TOA radiance is similar for both size distributions in the FT data. Differences are less marked at high scattering angles as we find that combining the ORAC refractive index with the DODO size distribution data lowers the phase function at near backscattering angles to values comparable with the ORAC dust model (not shown). In the BL, the DODO aerosol retains its larger scattering feature between 100°–150° and flatter diurnal response to changes in SZA.

We assess the sensitivity of the simulated radiances in the retrieval to changes in the assumed vertical distribution of aerosol by comparing the ORAC extinction coefficient profile shape and the observed DODO extinction coefficient profile. The ORAC dust profile assumes that most of the dust aerosol is concentrated below 2 km altitude with a linear decrease in aerosol burden between 2–3 km to zero above 3 km. In dusty regions in summer months this is a poor assumption as dust laden air from the BL is frequently lofted to 4–6 km [Liu et al., 2008b,a]. When we test the forward model using both vertical profiles we find a difference of <1 % in simulated radiance at 0.55 μm. At other wavelengths the vertical distribution of aerosol may be more important, particularly in the 0.8 μm channel where absorption by water vapour in the BL may enhance or dampen the aerosol signal depending on the relative location of the aerosol.

3.6 Development of Seasonal Information to Constrain Aerosol Type

We described previously the approach taken in the ORAC retrieval for the GlobAerosol dataset to determine aerosol speciation (section 3.4.3). Without making assumptions about aerosol *a priori* it is not possible to infer aerosol optical properties from current satellite retrievals. The work we showed in section 3 clearly indicates that accurate details of aerosol type and optical properties are critical to making an informed interpretation of aerosol properties from measured radiance. Here we test the ability of the ORAC retrieval to accurately classify aerosol type by choosing the correct aerosol model, given no prior information about aerosol spatial distribution, ie. using the retrieval cost function to decide after applying quality control criteria to each aerosol type. We use

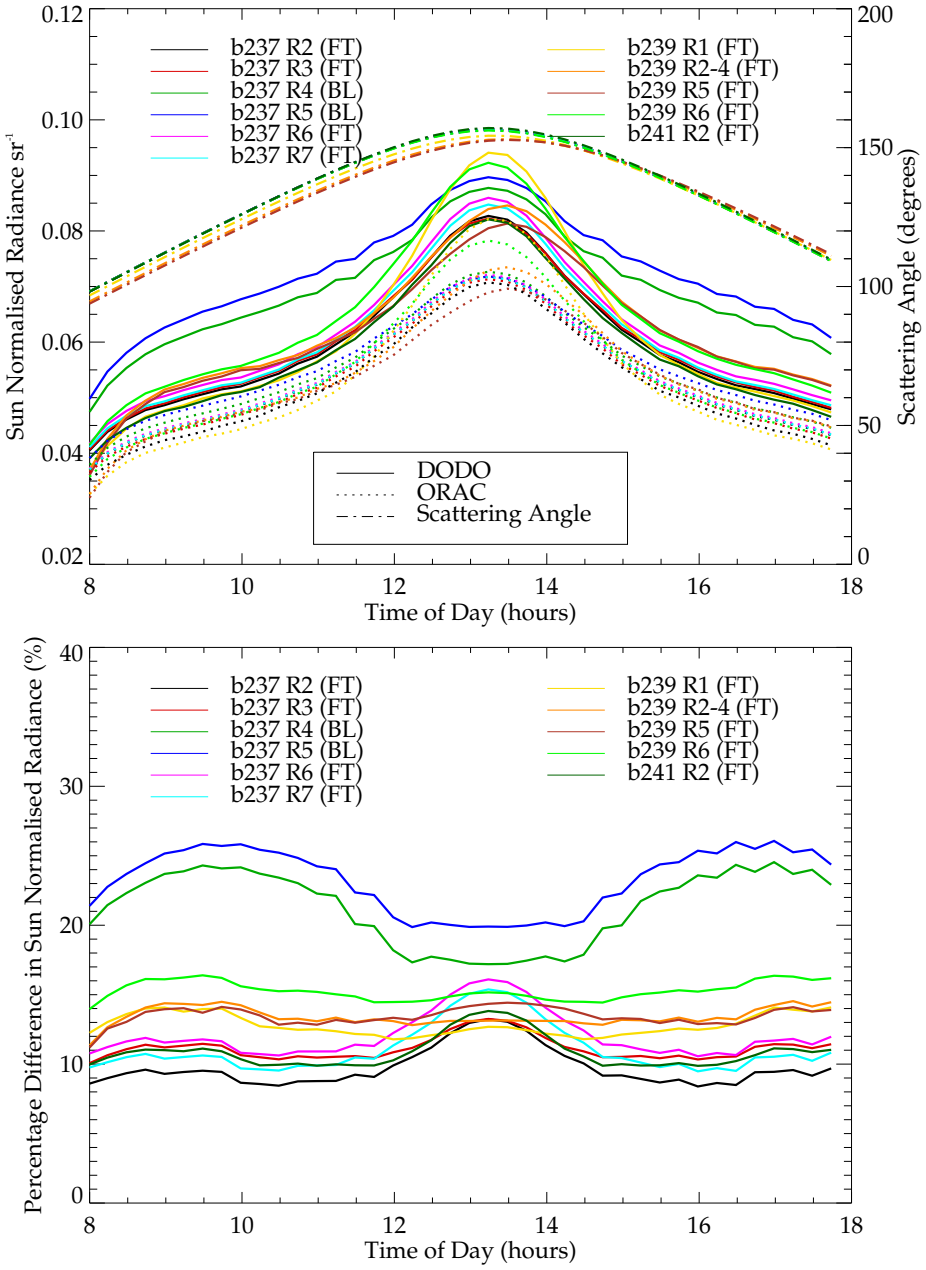

Figure 3.3: a) Forward model TOA sun normalised radiances (sr^{-1}, an approximation of the spectral bi-directional reflectance) corresponding to DODO (solid line) and ORAC dust (dashed line) *a priori*, matched according to aerosol effective radius and using DODO and ORAC refractive indices described as a function of time of day with corresponding scattering angles; b) their percentage difference. Radiances are shown for different flights and for the free troposphere (FT) and the boundary layer (BL). All calculations assume an aerosol optical depth of 0.5. Radiance is calculated at the location of the DODO flight and time is given as local time.

a Saharan Dust Index (SDI) and the GEOS-Chem chemistry transport model as tools to describe distributions of dust and biomass burning aerosol and assess the response of the retrieved AOD to

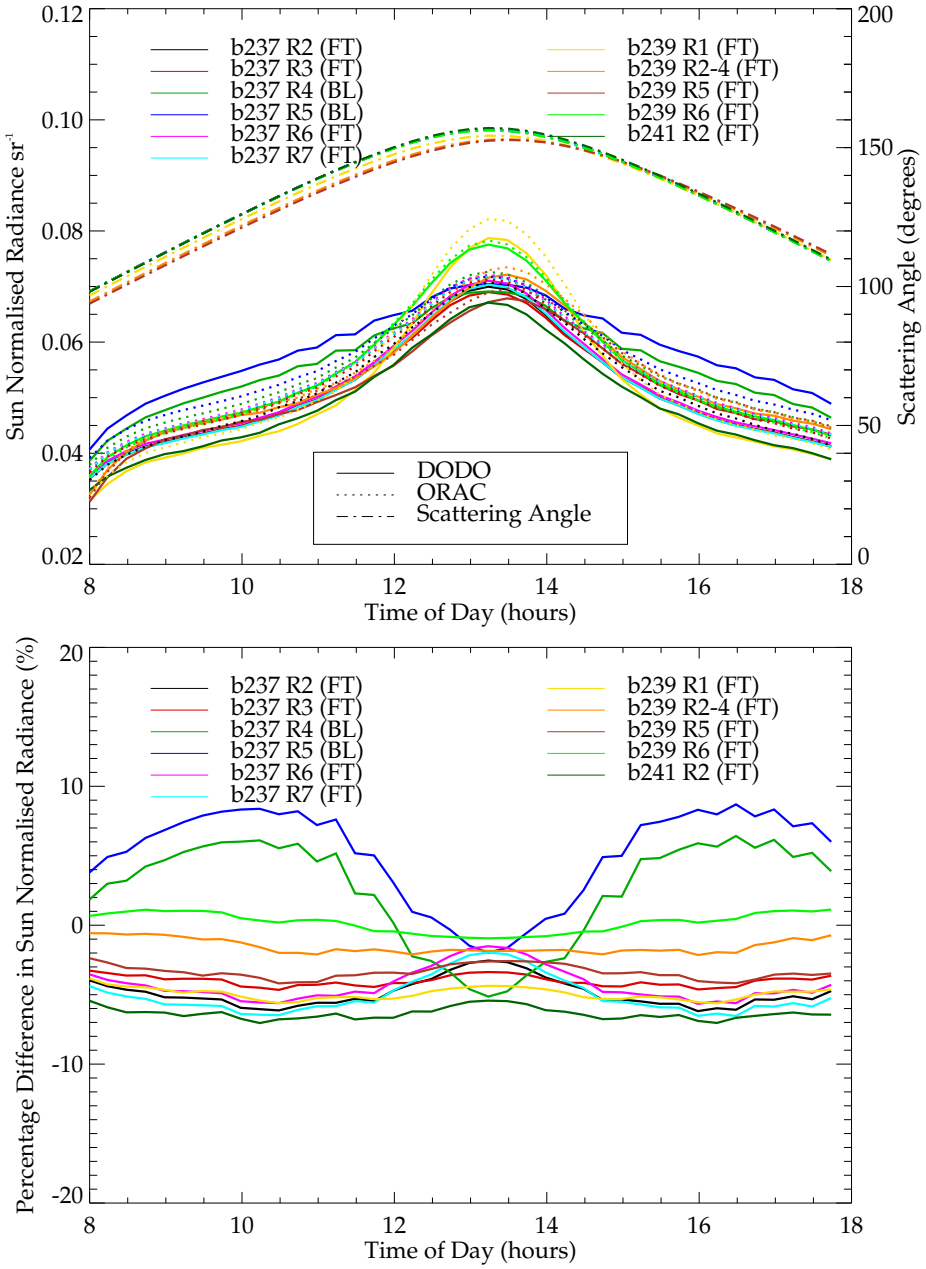

Figure 3.4: a) Forward model TOA sun normalised radiances (sr^{-1}, an approximation of the spectral bi-directional reflectance) corresponding to DODO (solid line) and ORAC dust (dashed line) *a priori*, matched according to aerosol effective radius and using only ORAC refractive indices described as a function of time of day with corresponding scattering angle; b) their percentage difference. Radiances are shown for different flights and for the free troposphere (FT) and the boundary layer (BL). All calculations assume an aerosol optical depth of 0.5. Radiance is calculated at the location of the DODO flight and time is given as local time.

the assumed aerosol speciation. The three major aerosol types observed across the SEVIRI field of view are marine aerosol over the ocean, and dust and biomass burning emissions both over the

African continent and advected across the Atlantic. We examine dust and biomass burning aerosol in turn below.

3.6.1 Desert Dust Aerosol

Desert dust aerosol is a mixture of minerals lofted into the atmosphere by the action of wind over arid regions [Haywood and Boucher, 2000]. We use a Saharan Dust Index (SDI), originally developed to identify aerosol contamination in nighttime sea surface temperature retrievals [Merchant et al., 2006], to determine dust distributions as a function of season and time of day. The SDI is calculated at the native SEVIRI spatial resolution of 3×3 km using data supplied by EUMETSAT [EUMETSAT, 2009].

The SDI uses variance in 3D brightness temperature difference space to indicate dust in satellite retrievals. Nighttime SDI values are calculated through principal component analysis (PCA) of brightness temperatures in different channels (3.9–8.7 μm, 3.9–12 μm and 11–12 μm), separating the variance caused by changing atmospheric variables such as water vapour identified along PC1, from variance induced by aerosol presence identified by PC2 [Merchant et al., 2006]. During the daytime this algorithm has to be adapted because the 3.9 μm channel is contaminated by solar radiation. We do this by using a local regression between daytime radiance in the three available channels and nighttime SDI values. The regression coefficients for estimating SDI without this channel are found to be valid over a length scale of ∼200 km and time scale of ∼ 1 day; beyond which they are decorrelated [Merchant, 2006]. To calculate SDI during the day we split the 0000 UTC SEVIRI nighttime image into 3364 boxes (∼192×192 km resolution in the nadir) to generate these local regression constants between observed brightness temperatures in the 8.7, 11 and 12μm channels and the calculated nighttime SDI for cloud-free pixels. We interpolate this information to the higher resolution retrieval grid (3×3 km in the nadir). We perform the daytime SDI calculation using the local regression constants from the 0000 hours nighttime SDI from the preceding and succeeding days to generate two distributions. The SDI for any intervening hour is calculated from these two distributions and is weighted according to the time of day. The SDI is scaled for convenience to be comparable to observed AOD so that dust is identified when SDI is in the range 0.25–2.0. Further details of the SDI derivation can be found in Merchant et al. [2006] and Merchant [2006].

We identify cloud-free scenes using the EUMETSAT cloudmask [EUMETSAT, 2009]. Optically thin cirrus cloud or cloud edges incorrectly classified as aerosol can result in erroneous SDI values. To reduce the cloud edge error we extend the cloudmask one pixel in each direction. To remove noisy scenes indicative of contamination due to isolated sub-pixel or incorrectly classified cloud, we discard scenes where the local standard deviation in the SDI over a moving 3×3 pixel window, on the 3×3 km grid, exceeds 0.2 for nighttime values and 0.1 for daytime values, as aerosol properties are coherent over relatively long spatial scales in clear skies in comparison with clouds. The local regression tends to dampen extreme values reducing data noise, hence the lowered daytime threshold value for discarding noisy scenes.

We calculate the probability of dust aerosol as the fraction of SEVIRI clear-sky scenes where the calculated SDI is between 0.25–2.0. For these calculations, we use hourly SDI values between 0800–1600 every day during 2006, which is limited by measurement availability only on a few days. To reduce contamination from persistent cloud we discard pixels where fewer than 20 % of the total scenes are clear. Figure 3.5 shows the seasonal probability of dust aerosols during the morning (0800–1000 UTC), midday (1100–1300 UTC), and afternoon (1400-1600 UTC), with local time at all longitudes across theSEVIRI disk falling within +/- 3 hours of these values.. Figure 3.5 shows that the SDI captures the seasonal variation in dust outflow over the Atlantic, Mediterranean and Red sea, peaking in JJA [Engelstaedter and Washington, 2007] and that there is little variation with time of day. The data shows that dust emissions migrate northward with the Intertropical Convergence Zone from DJF to JJA. We also find persistent dust emissions around the south west African coast likely originating from the Namibian and Kalahari deserts. Our analysis indicates that the flux of dust aerosols across the Atlantic shows no diurnal dependence. High dust probabilities in the polar regions are likely to be an artefact of the high viewing zenith angle.

3.6.2 Biomass Burning Aerosol

Biomass burning generates black carbon (BC), a highly absorbing aerosol via incomplete combustion (eg. Haywood and Boucher [2000]). We use the BC tracer in the GEOS-Chem chemistry transport model (CTM, described in Appendix 3.9) to identify the distribution of biomass burning

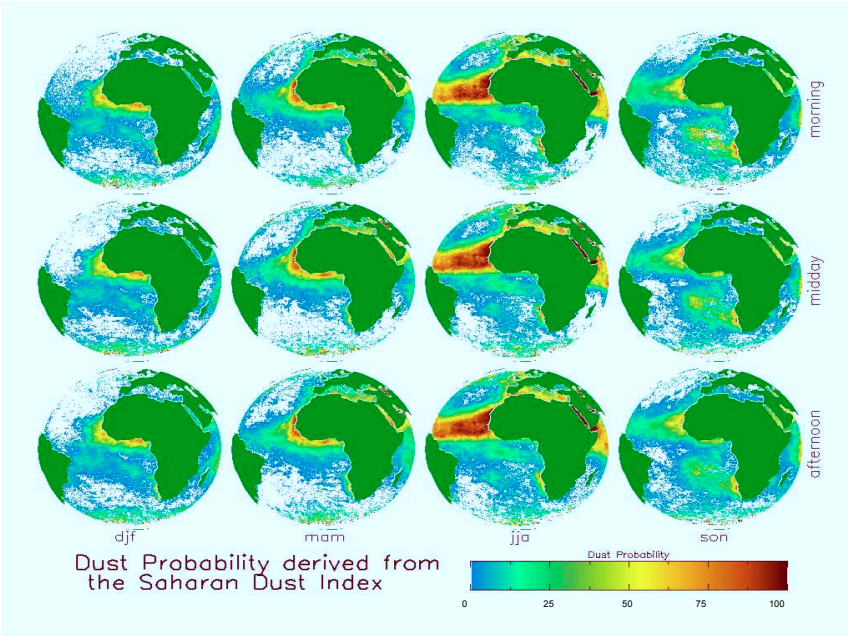

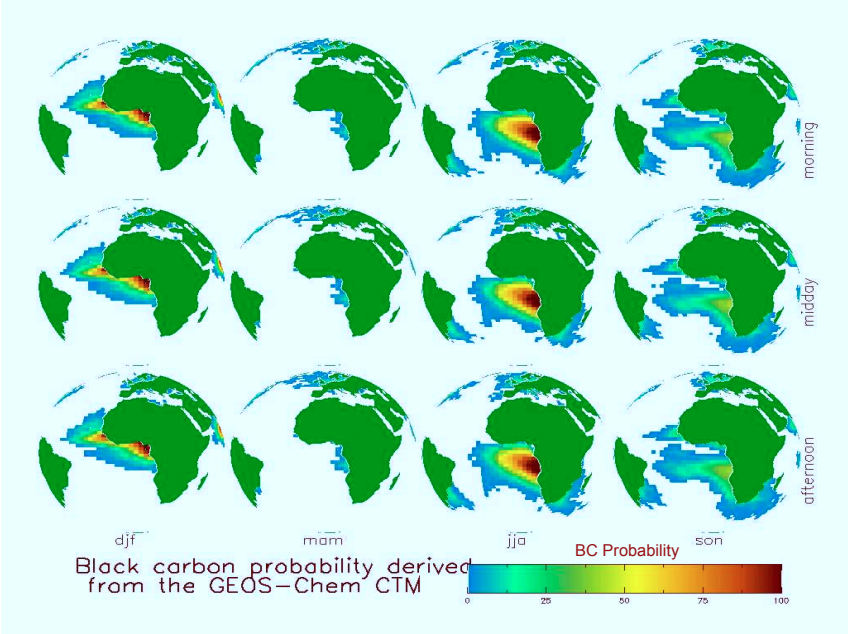

Figure 3.5: The independent seasonal probability of a) dust, and b) black carbon, during the morning (0800–1000), midday (1100–1300), and afternoon (1400–1600) for 2006. The probability of dust aerosols was determined by the SDI; and the probability of black carbon determined by the GEOS-Chem chemistry transport model form the fraction of total scenes in which each aerosol type was observed. SDI is calculated at the native SEVIRI resolution of 3×3 km in the nadir. GEOS-Chem simulations are at 2 x 2.5° resolution. White areas denote a zero probability of the given aerosol class.

aerosol, using model carbon monoxide (CO), another tracer of incomplete combustion, to help evaluate BC transport in the model. CO and BC are emitted primarily through incomplete combustion processes and share many similar sources, including biomass burning, and show similar distributions. First, we evaluate the global model CO using column observations from the NASA Tropospheric Emission Spectrometer (TES). The model captures 45–81 % of monthly variation in CO observed by TES, with the exception of JJA, where the correlation is < 0.6. We include a more detailed description of GEOS-Chem, TES, and their comparison including evaluation of CO and BC distributions and model performance in Appendix 3.9.

We calculate the probability of BC emissions using a column optical depth threshold of 0.015 to identify BC aerosol within the troposphere, accounting for aerosol transport from the surface layer. We acknowledge that this threshold may seem low for identifying enhanced aerosol loading but is appropriate given the optical depth output from the model. A similar probability measure is used to identify CO emissions where concentrations in an individual layer exceed background levels of 200 ppbv [Sinha et al., 2003]. Figure 3.6 shows CO and BC fields sampled from the model at midday (1100-1300 UTC). There is little variation within each season in the CO and BC distribution with time of day. The distributions of CO and BC are similar, as expected, but there are differences which reflect the different residence times of CO and BC. We find a strong near-source relationship between CO and BC reflecting the commonality of their source. BC is removed from the atmosphere more rapidly than CO which has a lifetime of 1 - 4 months, removed primarily through oxidation by the OH radical. Figure 3.5 shows the seasonal probability distributions of BC for morning (0800–1000 UTC), midday (1100 - 1300 UTC), and afternoon (1400 - 1600 UTC) calculated from hourly samples corresponding to the timings used in the SDI calculation. The seasonal distribution describes the southward migration of African fires as the year progresses, consistent with firecount data [Randerson et al., 2007]. Similar calculations were done for organic carbon (not shown), another possible proxy for biomass burning, but we found less agreement with CO than BC due to widespread non-combustion organic carbon sources.

3.6.3 Combined Aerosol Classification

Figure 3.7 shows "best type" SEVIRI AOD for 1012, 1312, and 1612 GMT on the 22nd, 24th, and 25th August 2006, corresponding to flights from the DODO aircraft campaign (described in

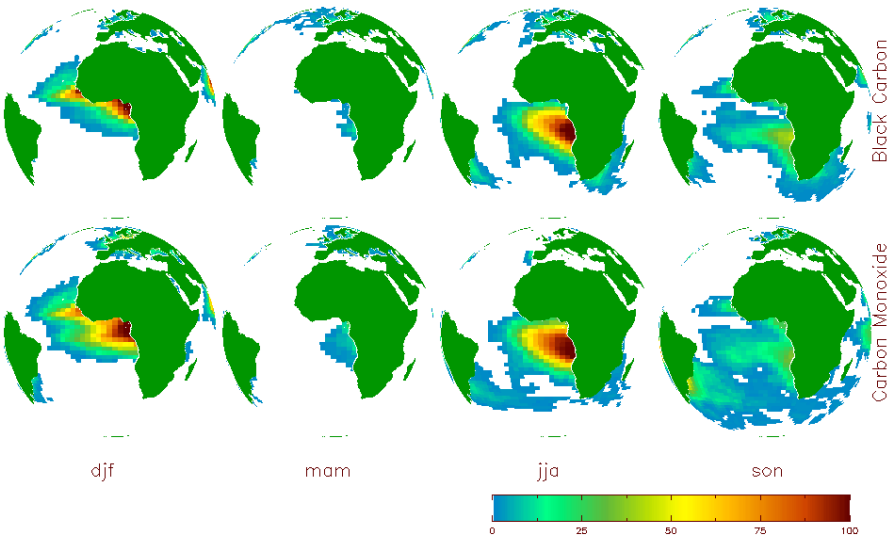

Figure 3.6: The independent seasonal probability of the presence of CO and black carbon aerosols between 1100–1300 for 2006. The probability, determined by the GEOS-Chem model, is evaluated on the $2\times2.5°$ model grid.

section 3.5.1). According to GlobAerosol the "best type" aerosol over the majority of the Atlantic is dust, despite JJA being the peak burning season over southern Africa [Randerson et al., 2007] fuelling transport of biomass burning aerosol across the Atlantic.

As shown above the SDI and GEOS-Chem model predict a distinct seasonal variation of the distribution of aerosol over the Atlantic. Figure 3.7 shows no evidence of the coherent dust or biomass burning plumes expected during JJA in the retrieval which contains no spatially or temporally resolved prior information about aerosol type and distribution. We suggest here a new approach to selecting aerosol type, using this information from the SDI and GEOS-Chem to inform the ORAC retrieval. We combine the individual probabilities from the desert dust and biomass burning aerosol distributions described above to give a conditional probability given the aerosol is present, of each single aerosol type or combination as a function of location, season and time of day. We use one minus the total probability of all other aerosol classes to determine where 'no aerosol' is most likely. In these regions we assume that background marine aerosol is present and that the maritime aerosol model should be used in the retrieval.

Figure 3.8 shows the most likely aerosol class constructed from the probabilities across the SEVIRI disk as a function of season. In DJF we find that the biomass burning aerosol plume over

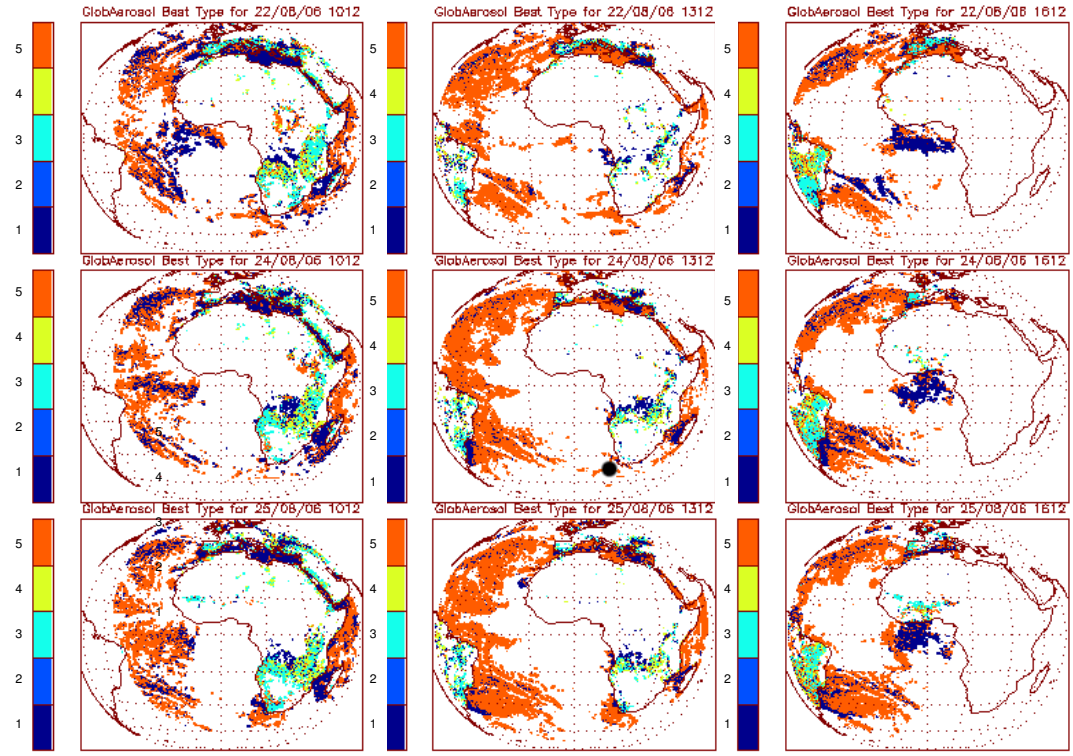

Figure 3.7: GlobAerosol "best aerosol type" for SEVIRI radiances at 3×3 km resolution at 1012, 1312, and 1612 on the 22nd, 24th, and 25th August, 2006, corresponding to the days of data collection during the DODO campaign. The "best type" is determined from the retrieval cost following quality control for different aerosol types: maritime (1), urban (2), continental (3), biomass burning (4), and desert dust (5).

the eastern equatorial Atlantic is commonly co-located with dust. In MAM, dust is the dominant aerosol outflow from the African continent. In JJA dust and biomass burning aerosol outflow form two distinct plumes. In SON aerosol outflow from the African continent is significantly reduced. This information could be used to inform the retrieval and reduce the number of aerosol models processed for each pixel. We suggest that these distributions along with their associated error could be used as a statistical constraint in the ORAC retrieval for a Bayesian inference of aerosol optical properties from observed radiance. In this approach the cost function may be used to help differentiate between aerosol classifications with similar probabilities.

In DJF we find a region where dust and biomass burning aerosol are consistently co-located just off the west African coast. We have no evidence to suggest that these aerosol types are directly mixed and they would likely be found at different altitudes as observed during the Dust and Biomass Experiment (DABEX) campaign [Johnson et al., 2008]. In this instance a two layer model is

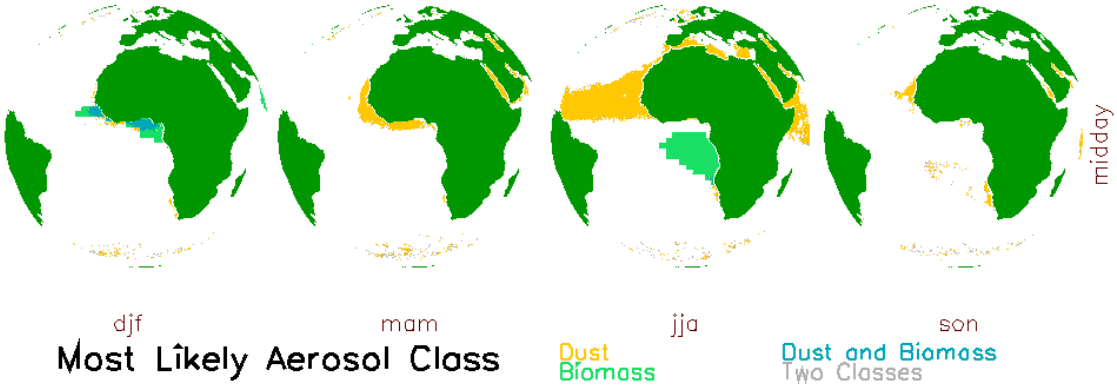

Figure 3.8: Aerosol type or combination with the highest probability as a function of season for 2006. White areas indicate background marine aerosol. Two classes refers to instances where two individual aerosol classifications share a maximum probability.

needed to accurately simulate the radiative transfer of the aerosol present which is not currently available in the SEVIRI ORAC retrieval. We acknowledge that this figure does not indicate how close the probability of the most likely class is to that of other classes and whether the additional information from the cost function would be needed to distinguish between aerosol class, but this is available for inclusion in the retrieval.

3.7 Retrieval Sensitivity to Constraining Aerosol Type

We test here the sensitivity of the ORAC AOD retrieval to aerosol speciation, comparing selection based on the cost function as implemented in the GlobAerosol retrieval, with aerosol selection based on our speciation maps. As described above, our aerosol classification contains an additional aerosol class, ‘dust and biomass burning’ which is not currently included in the GlobAerosol retrieval. To make a comparison at present between the two schemes, where dust and biomass burning are co-located in our speciation we assign no aerosol class and no retrieval is made. At 1312, the retrieval time used for this comparison this region often coincides with regions of sunglint where no aerosol retrieval can be made. We assign a marine aerosol classification to areas classified as neither dust nor biomass burning aerosol.

Figure 3.9 shows comparisons of monthly mean AOD in January and July 2006 which shows that background AOD is similar, independent of the aerosol classification used. In January we find AOD is generally 0.2–1 higher off the west coast of northern Africa when using the new aerosol

classification, and in July a similar discrepancy is observed further south. In these regions the GlobAerosol retrieval underestimates by 50–70 % the total AOD observed using our speciation. Both of these regions correspond to areas of biomass burning outflow (Figure 3.5) suggesting that this is not captured well in the current GlobAerosol SEVIRI AOD. In July, evidence of dust transport across the Atlantic towards South America observed in the SDI data (Figure 3.5) is evident in both classifications and from this we determine that the ORAC dust and maritime aerosol models are similar enough to capture dust advection even if the wrong classification is made. This occurs because the refractive indices for the marine and dust OPAC aerosol models are similar.

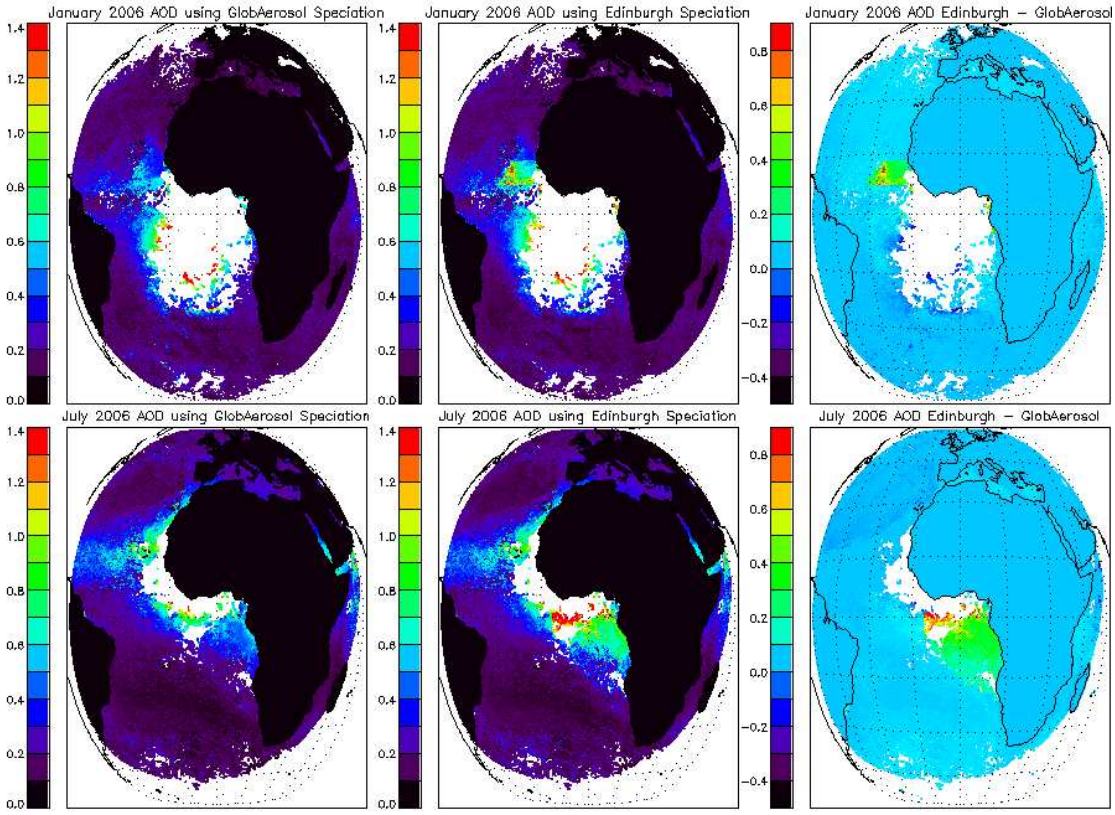

Figure 3.9: Monthly mean AOD in January and July 2006 retrieved from speciation assigned using prior prescribed by the GlobAerosol algorithm assigned using retrieval cost and other quality control tests, and speciation assigned using our aerosol distribution maps, and the difference between the monthly mean. White areas denote persistent cloud or sunglint where no retrieval is made. Continents where we are not examining the aerosol retrieval are coloured black.

We also compare the satellite AOD and Angström Exponent over Ascension Island (7S, 14W) and Cape Verde (16N, 22W) with Aerosol RObotic NETwork (AERONET) data [Holben et al., 1998] between January 2004 and January 2008. Table 1 shows comparative statistics between the satel-

Table 3.1: Statistics comparing the satellite Angström Exponent observations using lowest cost speciation (LC) and our new speciation (NEW), against level 2 AERONET ground based observations between Jan 2004 - Jan 2008 over Ascension Island and Cape Verde. Retrieved daily mean Angström Exponent is averaged over a 0.25 degree box centred on the AERONET location.

Location	Speciation	Correlation	RMS	Mean Difference (Retrieval - AERONET)	Mean Absolute Difference
Ascension Island	LC	0.26	0.46	0.07	0.37
Ascension Island	NEW	0.40	0.45	0.17	0.36
Cape Verde	LC	0.13	0.48	0.30	0.35
Cape Verde	NEW	-0.10	0.33	0.22	0.29

lite observations using our speciation, the lowest cost speciation and AERONET data. We exclude globaerosol retrievals where AOD > 2, indicative of cloud shadowing, and where the convergence cost is > 10. To ensure no cloud contamination we only include days with more than ten observations, and an AOD standard deviation below 0.2. The statistics are generated from daily mean values.

Over Ascension Island we find that the Angström Exponent is more consistent with AERONET data when using our new speciation (r = 0.4 compared with r = 0.26). The AERONET Angström exponent is indicative of biomass burning aerosol during summer months which is rarely selected using the GlobAerosol 'best type.' We also find that our speciation increases the AOD correlation from 0.52 to 0.55 (not shown). Over Cape Verde there is poor correlation between the satellite observations and AERONET values using both speciations. In this case using our speciation does not improve the Angström Exponent correlation, but does improve the root mean square and mean difference statistics. Introducing our speciation prior has the greatest impact in regions of biomass burning aerosol where the aerosol properties are significantly different from those in other classes (eg. dust and maritime aerosol). Over Cape Verde, improvements using our speciation are less marked as the OPAC descriptions of maritime and desert dust aerosol are similar. We acknowledge that comparing satellite and ground based observations is difficult given their different spatial scales. Significant work still remains to improve the correlation between satellite and ground-based observations of AOD reinforcing the statement that some caution must be exerted when using long-term satellite records of aerosol optical properties to determine aerosol forcing.

3.8 Summary and Concluding Remarks

We used detailed observations from the DODO flight campaign in August 2006 to test the sensitivity of the ORAC dust retrieval to prior assumptions about aerosol size distribution, refractive index, and vertical distribution. We find that implementing the DODO size distribution and refractive index data into the retrieval at 0.55 μm with a fixed AOD of 0.5 increases simulated radiance by 10–20 % with a larger bias observed at low solar zenith angles. We find that this discrepancy can be largely attributed to differences in the complex refractive index in the DODO and ORAC data, particularly within the FT. We test the sensitivity of the retrieval to the shape of the aerosol vertical distribution and find that given a fixed AOD this is unimportant in determining simulated radiance at 0.55 μm.

We also provide time dependent information to describe dust and biomass burning outflow from the African continent which we test in the ORAC retrieval during January and July 2006. We find similar background AOD but find discrepancies of 0.2–1 in AOD in regions of biomass burning outflow, where selecting the aerosol speciation based on the minimum cost function results in an underestimation of AOD by as much as 50–70 % in the standard ORAC retrieval in comparison to our version. This indicates the importance of assumed aerosol composition for an accurate estimate of the AOD retrieval. Despite poorly identifying the "best type" in a given scene, GlobAerosol partially addresses this problem by providing optical depths for each of its assumed aerosol models, so that better approaches to identifying type can be applied post-hoc. However, the extent to which such an approach can be successful is of course limited by the applicability of the assumed set of types. In particular, we find that biomass burning aerosol and dust often co-exist in DJF meaning that none of the types in GlobAerosol may be appropriate, and AOD in such scenes with multiple aerosol layers cannot be correctly resolved.

From the two pieces of complementary research presented above we conclude that satellite AOD retrievals are extremely sensitive to the properties assumed in the aerosol model, particularly the refractive index. We test a new method for classifying aerosol speciation, and suggest that our seasonal aerosol speciation could be included in a Bayesian retrieval which could use our probabilities, in conjunction with other information in the retrieval, to distinguish between aerosol classes with similar probabilities. This would improve the ability of the retrieval to capture con-

tinental aerosol outflow, which we have shown is particularly important for calculating AOD in regions of biomass burning.

We acknowledge that this study is limited geographically and highlight the importance of field campaigns such as DODO to accurately measure aerosol properties to inform satellite retrievals. Further research is necessary to quantify retrieval sensitivity to *a priori* for other aerosol types and retrievals, and this is of fundamental importance given the widespread use of satellite data by the scientific community to determine aerosol forcing. Future missions with instruments capable of both AOD and trace gas retrievals, for example CO, could help to better constrain the *a priori* data used in AOD retrievals.

3.9 Appendix: Description and Evaluation of GEOS-Chem Model CO Columns

We use the GEOS-Chem CTM (v08.02.01), driven by assimilated GEOS-5 meteorology from the NASA Global Modelling and Assimilation Office (GMAO) at a $2\times2.5^\circ$ horizontal resolution. Our calculations use 47 vertical levels, extending from the Earth's surface to an altitude of 80 km, 29 of which are below 10 km, and assumed to be within the troposphere. Here, we describe only the details pertinent to the CO evaluation and refer the reader to more comprehensive model descriptions in Le Sager et al. [2008]. In this model, monthly CO and BC emissions from biomass burning are from the Global Fire Emission Database version 2 (GFEDv2) [Randerson et al., 2007] and anthropogenic emissions of CO from the Emission Database for Global Atmospheric Research (EDGAR). We spin-up the model for 6 months from July 2005 to January 2006, taking initial conditions from a full-chemistry run of the model.

We use the Tropospheric Emission Spectrometer (TES) to evaluate GEOS-Chem CO columns from which we evaluate the spatial distribution of BC aerosol, as described in the main paper. The TES instrument, aboard the NASA Aura satellite, was launched in July 2004 in a near-polar sun-synchronous orbit with an equator overpass time of 1345, resulting in global coverage every 26 hours. TES CO has been found to agree within 5-10 % with in-situ observations between 200 - 700 hPa where it is most sensitive to CO concentrations [Lopez et al., 2008]. Here, we evaluate

GEOS-Chem CO columns on the $2\times2.5^{\circ}$ model grid between 1200–1500 local time. To directly compare GEOS-Chem column CO with TES data we sample the model at the time and location of the TES retrieval and interpolate the GEOS-Chem profile onto the TES pressure grid (GEOS). We then apply a scene-dependent averaging kernel (A), which accounts for the vertical sensitivity of the TES instrument and the TES *a priori* (y_a) to give a model profile (y_{model}) as shown below:

$$y_{model} = y_a + \mathbf{A}(GEOS - y_a) \tag{3.3}$$

Figure 3.10 shows monthly comparisons of CO columns over the African continent, between TES observations and y_{model} measurements. Globally TES and GEOS-Chem show good agreement with GEOS-Chem (not shown) capturing 45–81 % of the variation in TES CO in all but JJA when the correlation coefficient (r) is < 0.6, capturing < 36 % of the variability with a positive bias in GEOS-Chem CO. In order to check the representation of biomass burning emissions in our region of interest we reduce the comparison domain to focus on fire emissions from the African continent across the Atlantic (Figure 3.10), and find that the correlation increases between June and August (r = 0.71 - 0.88) but decreases significantly (r = 0.14 - 0.24) in September and October. In these months we find GEOS-Chem underestimates total column CO in this region but does show CO levels elevated above background values enabling us to use the model to describe the spatial distribution of biomass burning emissions. Underestimation of CO emissions in the GFED database seems the most likely cause of this discrepancy as the transport and chemistry in the model is sufficient to give high CO correlations in other months.

Acknowledgements. CEB is supported by NERC DARC studentship NER/S/D/2006/14345, and via additional support from the Rutherford Appleton Laboratory.

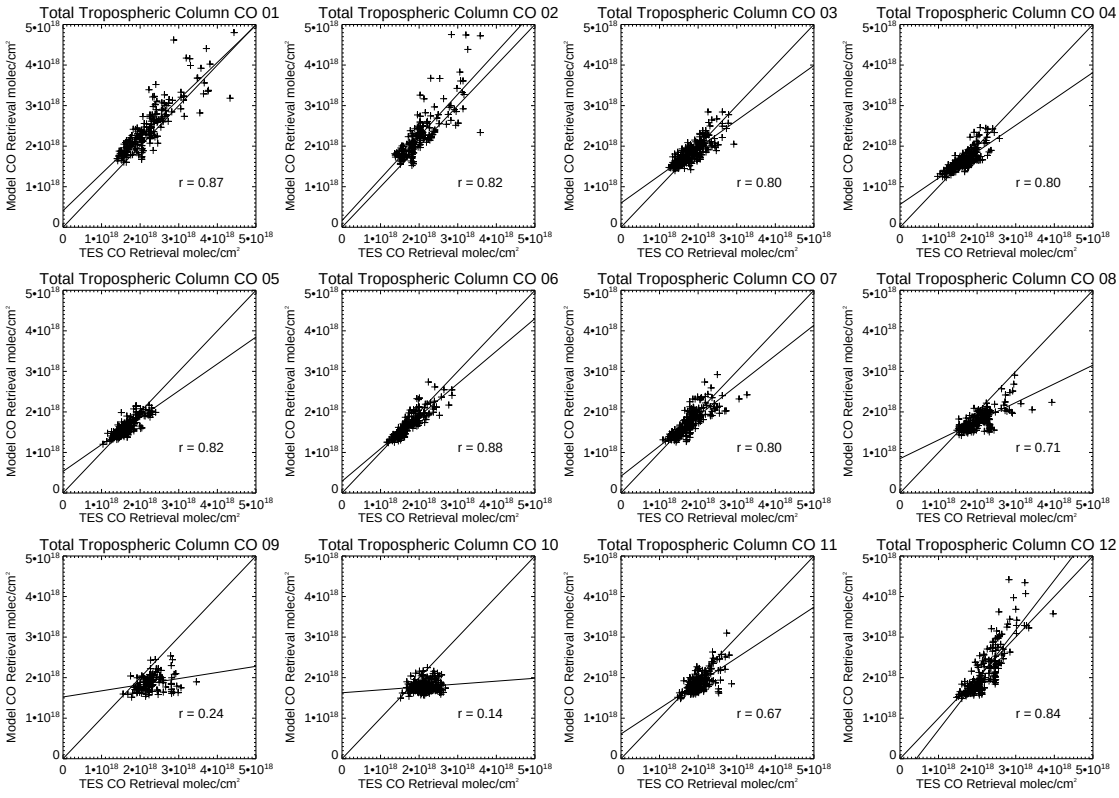

Figure 3.10: Monthly mean scatterplot of GEOS-Chem model and TES carbon monoxide column concentrations (molec cm^{-2}) during 2006 over the African continent (5N–20S, 10E–35W) compared on the model $2\times2.5^\circ$ grid. The correlation coefficient (r), the 1:1 line, and the line that best fits the data are shown inset into each panel. The top panel is January–April, the middle panel May–Aug and the bottom panel Sept–Dec.

Chapter 4

Saharan Dust Effects on Marine Stratocumulus Cloud

I use satellite observations of aerosol optical depth and cloud fraction from the MSG SEVIRI instrument to investigate the semi-direct effect of Saharan dust aerosol on marine stratocumulus cloud cover over the Atlantic during July 2006. I first use these data to study the spatial autocorrelation of aerosol optical depth and find that they are correlated over a lag of 0.1° (roughly 10 km at low latitudes) beyond which they rapidly decorrelate. During periods of high dust loading (AOD $>$ 0.5) I find a 15 % higher cloud fraction compared with periods of low dust loading (AOD $<$ 0.5). Under conditions of high dust loading cloud fraction increases with local static stability. I attribute this tentatively to aerosol solar shielding enhancing longwave cloud top radiative cooling which drives marine stratocumulus convection.

4.1 Introduction

Defining aerosol radiative forcing from all aerosol, both natural and anthropogenic, is the largest remaining challenge in closing the radiative budget when modelling the Earth's climate. With the exception of marine aerosol, dust is the single largest aerosol source, mainly natural in origin advected by wind from desert surfaces. Satellite and model studies have shown the Sahara to be one of the largest dust sources emitting between 170–1114 Tg yr^{-1} of the 500–5000 Tg yr^{-1} global dust budget [Goudie and Middleton, 2001; Engelstaedter et al., 2006]. Saharan mineral dust is typically comprised of elements such as calcium, aluminium and sulphur although the exact composition is source specific [Formenti et al., 2003; McConnell et al., 2008] giving minerals of different chemical composition, important in determining their optical properties and radiative

forcing. Saharan dust frequently undergoes long-range transport, with numerous studies tracking dust emissions across the tropical North Atlantic towards central and South America [McKendry et al., 2007; Ansmann et al., 2003; Liu et al., 2008b]. The large dust source is dominated by natural processes, mainly wind advection, but also includes some anthropogenic emissions due to land use change. The wide spatial extent of emissions from the Sahara make them a significant contributor to the total aerosol radiative budget which is at present poorly understood.

Dust both absorbs and scatters incoming shortwave (SW) solar radiation depending on particle size and chemical composition, altering both top of the atmosphere and surface radiative forcing. This is particularly important over the oceans where dust has a much higher albedo than the underlying ocean surface [Christopher and Jones, 2007]. Dust radiative effects are also important in the infrared as longwave (LW) radiation is absorbed and re-emitted by dust, potentially at much cooler temperatures than that emitted at the Earth's surface. Longwave radiative effects of dust are dependent on the altitude of the dust [Mallet et al., 2009], overlying atmospheric opacity and the local temperature profile. The LW contribution to net dust radiative forcing is estimated to be around 20% [Yang et al., 2009].

Dust and cloud interactions are also important in determining the dust radiative effect. Dust is generally hydrophobic but may become coated in soluble material such as sulphate making the aerosols effective cloud condensation nuclei (CCN) [Haywood and Boucher, 2000]. Evidence for the first indirect aerosol effect where CCN reduce cloud effective radius have been observed in a number of studies over dusty regions [Bulgin et al., 2008; Quaas et al., 2008; Bréon et al., 2002].

Another important pathway for dust interaction with clouds is through semi-direct effects [Huang et al., 2006; Su et al., 2008]. Traditionally, the term semi-direct effect has been used to describe the impact of absorptive aerosol such as black carbon overlying low-level cloud, on cloud cover. These aerosols absorb SW radiation, warming the atmosphere locally which may sufficiently reduce local relative humidity to induce cloud burn-off. Aerosols may also cause a local temperature inversion inhibiting cloud top radiative cooling, preventing air entrainment at the cloud base and reducing cloud cover [Ackerman et al., 2000a; Su et al., 2008; Huang et al., 2006]. These processes are represented schematically in Figure 4.1.

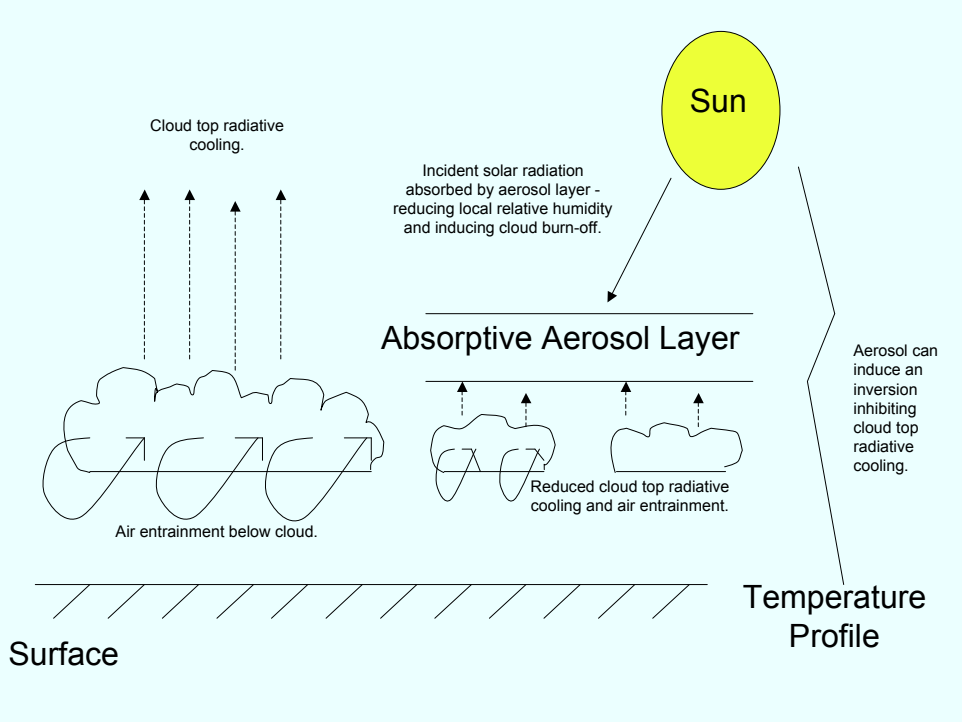

Figure 4.1: Semi-direct effects of predominantly absorbing aerosol overlying low-level cloud.

Dust is less readily absorptive of incoming solar radiation than black carbon and here I propose that it may have a semi-direct effect on clouds through the process of solar shielding, enhancing cloud cover. By reflecting incoming solar radiation, dust would cool the atmosphere locally enhancing cloud top longwave radiative cooling helping to maintain in-cloud air circulation [Ackerman et al., 2004]. This mechanism is shown schematically in Figure 4.2. A couple of studies using model data also suggest that absorbing aerosol above low-lying cloud can increase cloud cover by inducing an increase in temperature but also specific humidity increasing cloud fraction [Johnson et al., 2004; Perlwitz and Miller, 2010], but this effect is not well understood at present.

Here, I use satellite observations of aerosol optical depth from the Spinning Enhanced Visible and Infrared Imager (SEVIRI) derived using the ORAC retrieval algorithm as part of the GlobAerosol dataset [Thomas et al., 2009a], coupled with SEVIRI cloud fraction and cloud top height data from EUMETSAT [EUMETSAT, 2007; Lutz, 1999b] to test the hypothesis that Saharan dust advected over the tropical Atlantic ocean affects cloud cover via semi-direct aerosol effects. I use

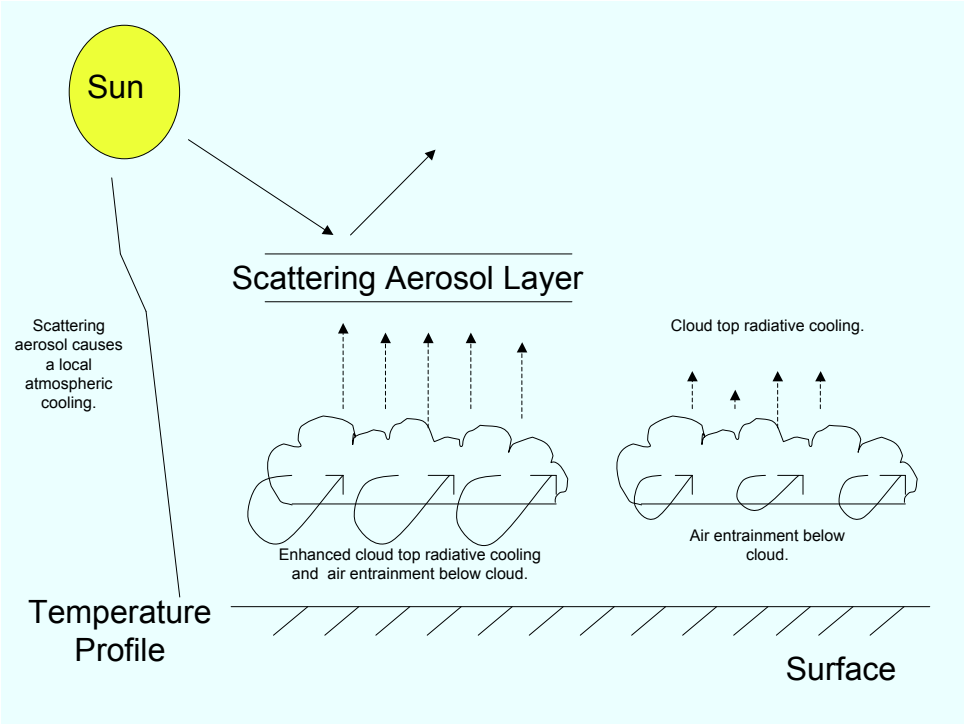

Figure 4.2: Semi-direct effects of predominantly scattering aerosol overlying low-level cloud.

additional information generated using the UK Universities Global Atmospheric Modelling Programme (UGAMP) offline trajectory model [Methven, 1997] to provide information about aerosol age and the local atmospheric stability.

4.2 Data

The Spinning Enhanced Visible and InfraRed Imager (SEVIRI) is aboard Meteosat Second Generation 2 (MSG2) and observes reflected and thermal radiance in twelve spectral channels; 0.6, 0.8, 1.6, 3.9, 6.2, 7.3, 8.7, 9.7, 10.8, 12, 13.4 μm and a broadband high resolution visible (HRV) channel. SEVIRI is in geostationary orbit centred over Africa and makes observations at fifteen minute intervals, with a resolution of 3 $\times$ 3 km in the nadir. Geostationary data at this spatial resolution enables us to make detailed observations of diurnal changes in aerosol and cloud properties. Aerosol optical depth (AOD) and the Angström exponent are retrieved as part of the GlobAerosol data product using the Oxford-Ral Aerosol and Cloud (ORAC) optimal estimation

retrieval scheme initially developed for clouds [Watts et al., 1998] and later extended to aerosols [Marsh et al., 2004]. ORAC fits the radiance in the 0.6, 0.8 and 1.6 μm channels, calculating top of the atmosphere radiance as a function of the properties of a plane parallel aerosol layer whilst accounting for aerosol *a priori* information. Satellite observations are not particularly well suited to aerosol process studies as they rely on aerosol models based on poorly constrained data from limited observations, but SEVIRI data has the key benefit of almost continuous coverage of the tropical Atlantic at a fine spatial resolution. Extensive discussion of the retrieval and its response to changes in the assumed aerosol model can be found in Bulgin et al. [2010] (accepted for publication by the Journal of Geophysical Research - chapter 3), and in this analysis I use the Edinburgh aerosol speciation generated in this research (chapter 3) to determine AOD. The Angström exponent is the ratio of AOD at two wavelengths: 0.6 μm and 0.8 μm and is inversely proportional to particle size.

I use a Saharan Dust Index (SDI) to identify dusty scenes, which was developed initially to detect dust contamination in sea surface temperature retrievals [Merchant et al., 2006]. Dust is identified by variance in 3D brightness temperature difference space using differences in the following channels (3.9–8.7 μm, 3.9–12 μm and 11–12 μm). During the day a local regression is performed against nighttime SDI values when retrievals in the 3.9 μm channel are contaminated by solar radiation [Merchant, 2006]. Clear pixels are identified using the EUMETSAT SEVIRI cloud mask which I extend by one pixel in each direction when calculating the SDI to minimise the possibility of cloud contamination. A more detailed description of the SDI can be found in chapter 1.

The SDI is scaled to be roughly comparable to AOD, and SDI values between 0.25–2 are indicative of dust. The EUMETSAT cloud mask is derived using up to 34 threshold tests based on retrieved radiance in all but the 9.7 μm and HRV channels [EUMETSAT, 2007] and from this I derive cloud fraction. When identifying clear scenes I extend the cloudmask by one pixel in each direction as with the SDI, and then remove these data at cloud edges where the cloudmask is potentially ambiguous. I use the EUMETSAT cloud top height product derived from the cloud masking tests and meteorological data which has a 300 m resolution in the vertical, and a 9×9 km spatial resolution in the nadir, to isolate low-level cloud below 1.3 km within the boundary layer.

As discussed in chapter 1, accurate cloud masking of satellite data is still a significant challenge under some atmospheric conditions, particularly along cloud edges or in the presence of dust. To account for this I sacrifice some data by extending the EUMETSAT cloudmask by one pixel in each direction in order to remove ambiguous data at cloud edges and only calculate the SDI for the remaining clear scenes. Within the SDI, sub-pixel cloud may be erroneously classified as dust as discussed in chapter 3. In this study the local SDI standard deviation was not used to identify variation induced by sub-pixel cloud but this could be a useful constraint in future work.

I calculate additional information about aerosol age and atmospheric stability using data from the UGAMP offline trajectory model [Methven, 1997]. Trajectories are calculated using 6–hourly ECMWF ERA-40 T159 reanalysis data, running backwards in time over a 10 day period to determine air mass origin. Here, I run the code at one degree resolution across the domain of interest (13°–35° N, 17°–40° W) at 800 and 850 hPa. Boundary layer static stability has been found to be positively correlated with cloud fraction [Klein and Hartmann, 1993], where higher static stability indicates more stable conditions and more cloud. Local static stability above the cloud layer is important in determining cloud top longwave radiative cooling and local convection which drives stratocumulus cloud formation. I filter the cloud data for cloud top height below 1.3 km and calculate local static stability using, static stability = $\theta_{800\text{hPa}} - \theta_{850\text{hPa}}$ where θ is the potential temperature. I chose the pressure range 800–850 hPa immediately above the cloud layer, where static stability values range from 2–6 with 6 indicating high static stability. I classify aerosol age by identifying 'touchdown' points where the air parcel trajectory descends below 900 hPa, into the boundary layer over the African Continent (13°–26° N, 15° W–35° E). The range 800–850 hPa is selected to represent the air layer above the cloud. The altitude at 850 and 800 hPa is calculated using:

$$z_2 - z_1 = -\frac{R\overline{T}}{g} ln \frac{p_2}{p_1} \tag{4.1}$$

where z and p are altitude and pressure respectively at two levels ($_1$ and $_2$), R is the gas constant for air, $\overline{T}$ is the mean temperature and g is acceleration due to gravity. Assuming a surface pressure of 1000 hPa and mean temperature of 293.15 K gives an altitude of 1.4 km at 850 hPa and 1.5 km at 800 hPa, above the 1.3 km filter on cloud top height data.

The available data are gridded at different spatial resolutions so I create super pixels of 0.16° latitude by 0.16° longitude in which I calculate the average AOD, Angström exponent, cloud fraction and cloud top height. To determine boundary layer stability, local stability and aerosol age, I average values from the surrounding $1^\circ \times 1^\circ$ box as these data are calculated at a coarser spatial resolution. I place a 60% threshold on the data classification where $> 60\%$ of the cloud-free scenes in a given super pixel must be identified as having a high dust loading before a dust classification is made; a similar threshold for low dust loading scenes is used to remove any ambiguous data points. For the high dust case I only use data where the air masses between 800–850 hPa can be traced back to the African continental boundary layer indicating that the aerosol is likely to be located directly above the low-level cloud rather than elsewhere in the column. Pixels with low-dust loading are constrained by a maximum AOD of 0.5.

4.3 Results

I process data in the region 13°–35° N, 17°–61° W, throughout July 2006, during the peak season for dust outflow from the Sahara, focusing on SEVIRI retrievals at 1012 and 1312 UTC for which AOD and the Angström exponent are retrieved as part of the GlobAerosol data product (described in detail in chapter 3). Data at 1612 UTC are also calculated as part of this product but the area of interest is substantially affected by sunglint at this time and these data are not included in my analysis. One inherent difficulty in using satellite data to quantify aerosol and cloud interaction is that aerosol and cloud retrievals are not coincident. Many studies have averaged cloud and aerosol properties over spatial domains of typically $1^\circ \times 1^\circ$ [Quaas et al., 2008; Nakajima et al., 2001; Bulgin et al., 2008] whilst others have used back trajectories [Bréon et al., 2002] or tracer transport models [Avey et al., 2007] to link retrievals. I determine the spatial autocorrelation (ρ) of all (n) points (x_i, y_i) separated by a given lag, where m_x, m_y are the mean and σ_x, σ_y, the standard deviation of the x and y pairings using:

$$\rho = \frac{\frac{1}{n}\Sigma_{i=1}^{n}(\mathrm{x}_i - \mathrm{m}_x)(\mathrm{y}_i - \mathrm{m}_y)}{\sigma_x \sigma_y} \tag{4.2}$$

Figure 4.3 shows aerosol autocorrelation over a spatial lag ranging from of 0.1°–1° (approximately 10–100 km at low latitudes). I find reasonable correlation at a spatial lag of 0.1° (approximately

10 km^2) where r = 0.74, quickly diminishing to r $<$ 0.28 at 0.2°, a distance much smaller than that over which aerosol properties have been assumed consistent in other studies. These spatial autocorrelations are consistent with time of day.

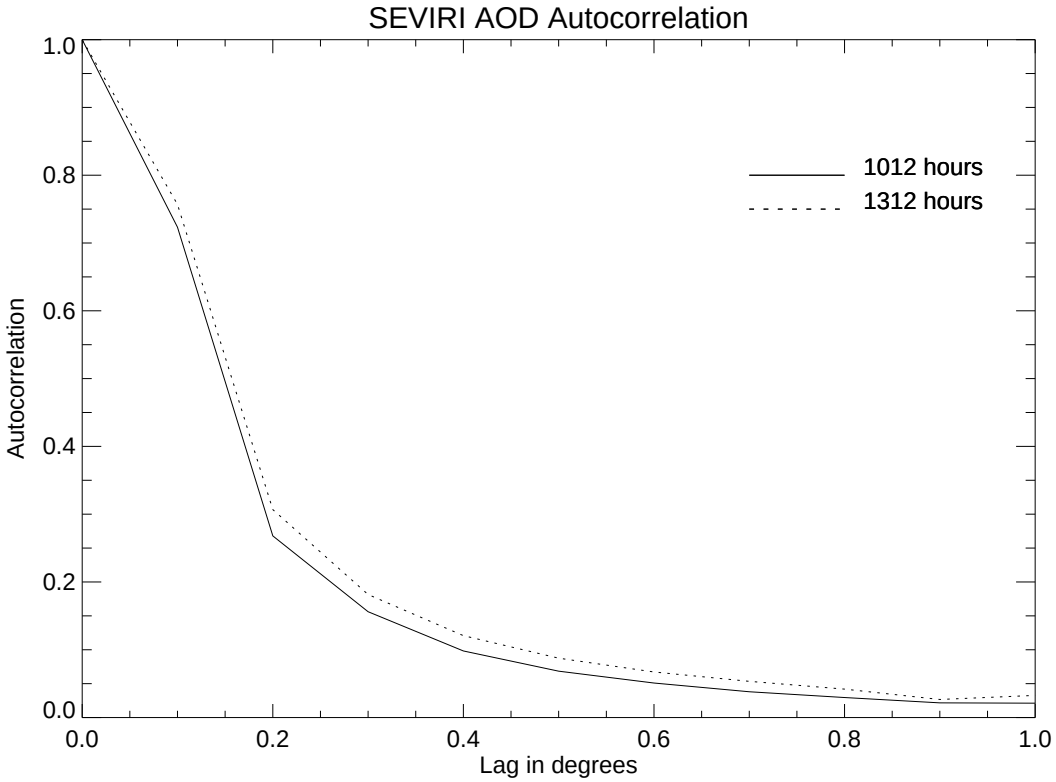

Figure 4.3: Aerosol optical depth spatial autocorrelations with lags of 0.1°–1°, observed at 13°–35° N and 17°–61° W during July 2006 at 1012 and 1312 UTC. AOD data comes from the ORAC retrieval as part of the GlobAerosol project, with the aerosol speciation selected according to the Edinburgh aerosol classification [Bulgin et al., 2010] (chapter 3, accepted for publication by the Journal of Geophysical Research). Spatial autocorrelation is calculated in latitudinal and longitudinal directions only, giving the same number of comparison points at each spatial lag.

Figure 4.4 shows the change in cloud fraction as a function of local stability under both high and low dust loadings. Here I have reduced the longitudinal boundary to 17–40W to focus on the main region of dust outflow. Standard errors in cloud fraction (standard deviation (σ) / number of observations (n)) are superimposed on the data points but are close to zero. Data points in each local stability bin exceed 100 in all cases and typically exceed 1000 in the high dust case. There is a decrease in cloud fraction in both cases between 1012 and 1312 UTC which is consistent with previous observations of a diurnal cycle in low-level stratocumulus cloud in tropical regions, driven by solar absorption with a maximum around 1000 hours local time [Wood et al., 2002].

Across this region (17–40 W) the variation in local time from UTC time is a maximum of minus 2 hours making these results consistent with those observed by [Wood et al., 2002]. In the high dust case the cloud fraction is consistently 15% higher than in the low dust loading case, and is positively correlated with local static stability ($r > 0.92$), whilst in the low dust case there is no correlation between cloud fraction and local static stability ($r < 0.26$).

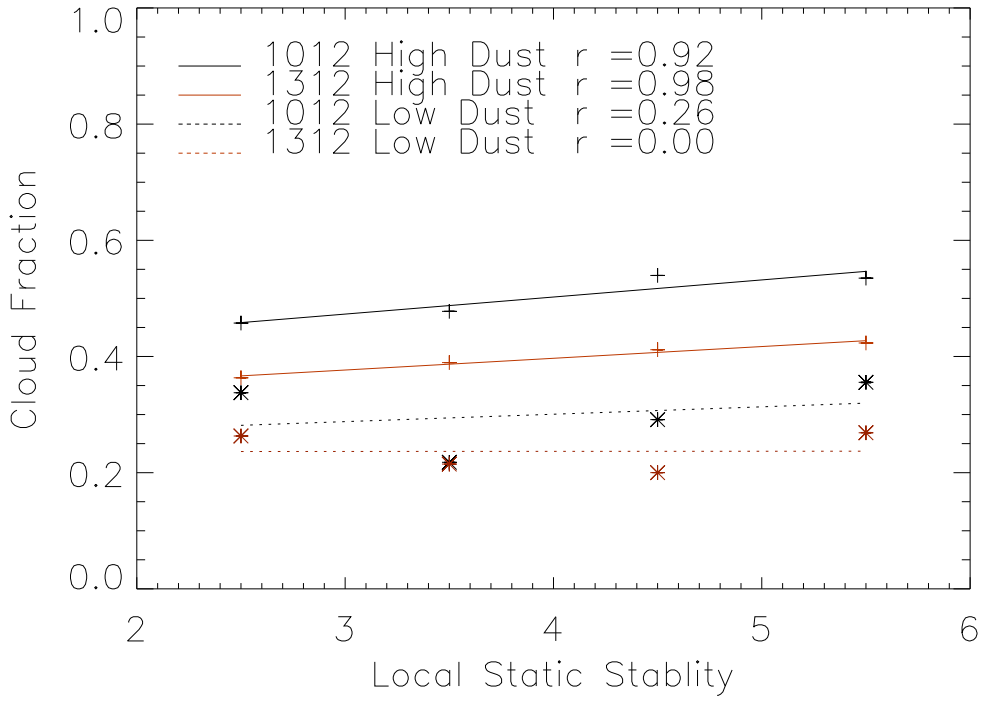

Figure 4.4: Cloud fraction derived from EUMETSAT cloudmask data as a function of local static stability under both dust and clear conditions. Data at $0.16° \times 0.16°$ resolution are averaged between 13°–35° N and 17°–40° W throughout July 2006. Standard errors in cloud fraction (σ/n) are superimposed on the data points but are close to zero. Data points in each local stability bin exceed 100 in all cases and typically exceed 1000 in the dust case.

These data indicate that there is a dust effect impacting cloud cover in this region. Figure 4.5 shows cloud fraction as a function of static stability for the high dust and low dust cases indexed according to AOD, the Angström exponent and aerosol age. For the high dust case, cloud fraction shows a weak positive correlation with AOD (r = 0.26–0.34), and the local static stability increases between 1012 and 1312 UTC. This indicates a local warming of the atmosphere above the cloud suggesting that some of the dust aerosol above the cloud is absorbing SW radiation and increasing local stability. In the case of high dust loading cloud fraction increases and this may be attributed

to solar shielding of the cloud below through both scattering and absorption of SW radiation. Solar shielding would increase cloud top LW radiative cooling driving convection in stratocumulus cloud maintaining the cloud layer [Ackerman et al., 2004].

Although there is evidence for both absorption and scattering of incoming solar radiation here, the increase in cloud fraction suggests that the scattering processes are dominant (as in Figure 4.2). The increase in cloud fraction may also be attributed to the counter feedback of the traditional semi-direct effect where aerosol warming increases specific humidity which in turn increases cloud fraction [Perlwitz and Miller, 2010; Johnson et al., 2004]. This possibility could be investigated using specific humidity data from ECMWF reanalysis. Analysis of this nature would be more informative when aerosol is routinely assimilated into the ECMWF forecast model as it is currently prescribed by an aerosol climatology. Similarly, this assimilation could be important in more accurately defining static stability changes in regions of aerosol outflow.

In the low dust loading case there is a decrease in local static stability between 1012 and 1312 UTC (Figure 4.5). Under this regime there is less aerosol to absorb the solar radiation and less cloud. Solar heating will increase convection and deepen the boundary layer during the morning reducing local stability. In both cases there is a decrease in the Angström exponent between 1012 and 1312 UTC indicating an increase in aerosol particle size. The reduction of cloud fraction by solar absorption during the diurnal cycle may explain this change as this would generate large, humidified aerosols [Koren et al., 2007]. Figure 4.5c indicates that aerosol age is not an important factor governing this aerosol-cloud interaction, as it shows no variation with cloud fraction or local static stability.

One difficulty in using satellite data to examine aerosol-cloud interaction is determining aerosol altitude given only a column retrieval of aerosol optical properties. Here I isolate cases where aerosol is present directly above clouds through the use of back trajectories but this does not preclude aerosol also being present within the cloud. Under these conditions the aerosol may also act as cloud condensation nuclei further increasing cloud cover by reducing cloud droplet size and inhibiting precipitation [Albrecht, 1989].

4.4 Concluding Remarks

I have used satellite data on a finer spatial and temporal scale than previously available to study the effect of dust on marine stratocumulus cloud fraction over the tropical northern Atlantic in July 2006. I find an increase in cloud cover during dust events which I attribute tentatively to solar shielding of the cloud by aerosol, enhancing cloud top LW radiative cooling. There are a range of potential feedback mechanisms under these conditions where aerosol overlies low-level cloud. Further studies of satellite data at this spatial and temporal resolution coupled with aircraft observations of aerosol properties both above and below cloud would be beneficial in attempting to untangle the range of possible feedback mechanisms.

4.5 Implications of the AOD autocorrelation for the spatial averaging used in chapter 2

The work examining the spatial autocorrelation length scale in this chapter has implications for the spatial averaging used in chapter 2 to study aerosol indirect effects. The work in chapter 2 has a different focus as it is looking at long-term correlations between aerosol and cloud properties (τ_a and r_e) over monthly and seasonal time periods. However, it makes the assumption that aerosol properties are correlated over $1 \times 1\,^{\circ}$ spatial domains. The averages used here may have dampened the signal between aerosol and cloud properties, and the signal may be stronger than suggested previously by studies of this nature [Nakajima et al., 2001; Bréon et al., 2002]. Although useful for obtaining a global overview of aerosol-cloud interactions there is an increasing recognition within the scientific community that aerosol and cloud observations need to be more closely linked [Bréon et al., 2002; Avey et al., 2007]. The results presented here suggest that smaller scale studies evaluating aerosol-cloud interactions in response to changing meteorology are critical to understanding the radiative impact of aerosols under different climatic regimes.

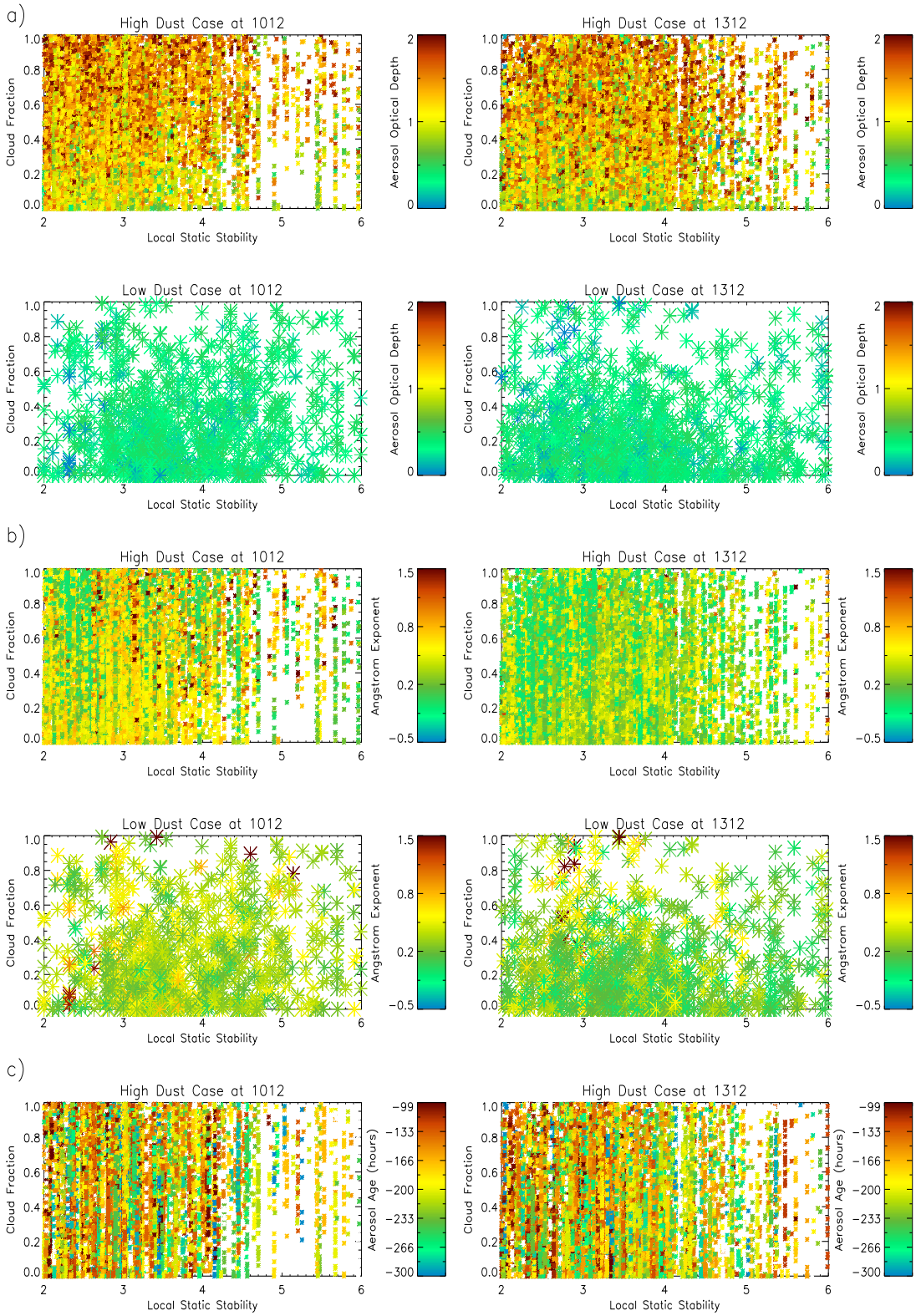

Figure 4.5: Cloud fraction as a function of local static stability throughout July 2006 between 13°–35° N and 17°–40° W. Data are indexed as a function of a) aerosol optical depth, b) the Angström exponent and c) aerosol age for high dust (AOD $>$ 0.5) and low dust (AOD $>$ 0.5) scenes. I only calculate aerosol age for dusty scenes. Data points for the high dust cases exceed 10^4 observations and for the low dust cases 10^3 observations.

Chapter 5

Discussion and Concluding Remarks

In my introduction I outlined three research questions that I aimed to address through the work in this thesis: 1) The Twomey [1974] hypothesis outlines aerosol forcing through the cloud albedo effect but is this sufficient to parameterise aerosol forcing via the first indirect effect on a global scale? 2) To what extent can we rely on satellite retrievals constrained by simplistic aerosol models to accurately define aerosol optical properties which show significant spatial and temporal heterogeneity? 3) Dust is widely considered as hydrophobic and consequently does not readily act as cloud condensation nuclei but to what extent does it exert a radiative forcing through semi-direct aerosol-cloud interactions?

The over-arching question in aerosol science is: how do aerosols modify the radiation budget through scattering and absorption of radiation and through interaction with clouds? The questions I pose in this thesis are all interrelated, contributing to our understanding of aerosol forcing. Within the wider context of climate science this question is critical to closing the radiative budget when modelling the Earth system [Trenberth and Fasullo, 2010]. This has an important application when projecting future climate change in response to different anthropogenic emission scenarios.

Aerosol research now spans a number of decades but we are still unable to quantify aerosol forcing, resolve the issues of aerosol-cloud interaction, and fully understand the processes involved. A global parameterisation of aerosol forcing for inclusion in climate modelling has been much sought after, but as postulated in a recent review we would be best served to study aerosol-cloud interaction at a regional level [Stevens and Feingold, 2009]. As evidenced in the work in chapter 2, to adopt a global parameterisation of the Twomey [1974] indirect effect in models would mask much of the regional and seasonal variation in aerosol forcing [Bulgin et al., 2008]. Localised studies have shown that aerosol forcing is regime dependent [Stevens and Feingold, 2009].

Aerosol forcing is governed by both 'external' factors including local meteorology and 'internal' factors including aerosol size distribution, loading, chemical composition and mixing. Regional parameterisation of aerosol and clouds in global climate models is typically poor [Stevens and Feingold, 2009] but these need to be resolved to improve climate projections. Local changes in aerosols and clouds will feed back into other parts of the climate system including the hydrological cycle and be important in determining regional temperature and precipitation.

With the development of passive remote sensing technology, satellite observations have become increasingly important in aerosol research [Bulgin et al., 2008; Quaas et al., 2004; Nakajima et al., 2001; Bréon et al., 2002], providing global data at better spatial and temporal resolution than available from sparse ground-based observation networks or aircraft campaigns. Aerosol process studies use retrievals of aerosol and cloud properties to infer aerosol-cloud interaction but these data are often limited [Stevens and Feingold, 2009]. There are several inherent difficulties in using satellite observations to quantify aerosol-cloud forcing: aerosol and cloud retrievals are not coincident and aerosol altitude cannot be determined through passive remote sensing. A commonly used approach to address the first problem has been to average retrieved aerosol and cloud properties over a large spatial domain typical $1^\circ \times 1^\circ$ (approximately 100 km^2 at low latitudes). In calculating the spatial autocorrelation of Saharan dust AOD from the ORAC SEVIRI retrieval (chapter 4) I find that these observations become decorrelated over spatial scales greater than approximately 10 km. Averaging aerosol properties over a wider spatial scale may dampen the aerosol forcing as we observe when taking a global average [Bulgin et al., 2008] emphasising the point that we need to study aerosol processes at a local regime level.

Satellite observations of cloud-top height enable us to isolate low-level cloud but in many studies no constraints are placed on aerosol altitude [Bulgin et al., 2008; Bréon et al., 2002]. The assumption that aerosol will be located at the same altitude as the cloud may not always be valid as aerosol injection height varies, and observations have shown that Saharan dust over the Atlantic is frequently lofted to altitudes between 4–6 km within the Saharan air layer [Liu et al., 2008a,b]. To address this problem in my study of Saharan dust forcing (chapter 4), I release single back trajectories at a $1^\circ \times 1^\circ$ spatial resolution to determine whether the air mass at the altitude of interest is likely to contain aerosols (as in chapter 4). This method could be improved by releasing clusters

rather than single particles [Brankov et al., 1998] at a finer spatial resolution, or releasing clusters of particles from each scene identified as meeting the other analysis criteria to determine whether aerosol is present at the given altitude. This would also give a better estimate of aerosol age to include in process studies.

Satellite data therefore suffer from a number of weaknesses that need to be acknowledged and addressed in future process studies. The satellite retrieval itself is also subject to error as the retrieved radiance is interpreted using radiative transfer code which includes an aerosol model constrained by limited global data on aerosol characteristics [Bulgin et al., 2010]. The ORAC retrieval, the focus of this research, is sensitive to changes in aerosol refractive index, aerosol size distribution, and solar zenith angle [Bulgin et al., 2010], and there are significant differences between the dust aerosol model assumed in the retrieval, based on values from the Optical Properties of Aerosols and Clouds (OPAC) database [Hess et al., 1998], and observations made during the DODO flight campaign [McConnell et al., 2008]. The ORAC scheme uses an optimal estimation approach enabling all retrieved parameters to vary simultaneously to best fit the simulated radiance to the observed radiance. Consequently differences in simulated radiance induced by a poorly constrained aerosol model could be manifested in any of the retrieved variables. These errors within the retrieval must be quantified and accounted for when using these data in process studies.

This work has highlighted the need to draw on and integrate data from different sources to study aerosol processes. This process is often non-trivial as each dataset has a different spatial and temporal resolution and associated error. I have shown the value of this approach in this thesis, using data from GEOS-Chem to constrain the ORAC retrieval (chapter 3) and combining ECMWF data with satellite retrievals of aerosol optical properties to study Saharan dust forcing (chapter 4).

With respect to the research questions posed at the beginning of this thesis a more detailed discussion of the individual studies is presented in chapters 2–4 as these are written in the format of journal articles. Here I summarise the main points.

1) Although satellite data can be used to generate a global parameterisation of the Twomey [1974]

indirect effect, taking this approach masks many region and seasonal variations. In the region of biomass burning aerosol emissions from the African continent during the peak burning season (June–August) I find that the Twomey [1974] parameterisation is insufficient to explain the response in cloud effective radius in relation to changes in AOD. This suggests that this relationship based on aerosol number concentration alone is too simplistic, and other factors need to be accounted for including aerosol size and chemical composition [Dusek et al., 2006] and changes in liquid water content [Ackerman et al., 2004].

2) Selection of aerosol speciation is poorly constrained in the ORAC model and simulated radiance is sensitive to changes in the size distribution and refractive index of the assumed aerosol model, and is also sensitive to viewing geometry. The retrieval is also only capable of resolving scenes containing a single aerosol layer and type. These findings should cause the scientific community to exert some caution when using these data in process studies until these errors can be fully quantified and accounted for.

3) In regions of high Saharan dust loading across the Atlantic in July 2006, I find evidence for increased cloud cover through the process of aerosol solar shielding. This is the first study to provide evidence for semi-direct forcing of Saharan dust and further work is necessary to quantify the magnitude of this forcing and whether it occurs at other times of year.

The outcomes of this research have generated a number of further questions that we need to address in our attempts to quantify aerosol forcing. These include: what other processes are governing the relationship between aerosol optical depth and cloud effective radius off the west coast of Africa where the Twomey [1974] parameterisation does not explain aerosol forcing, apart from aerosol number concentration? Are these processes important in other regions of aerosol outflow? Does dust shielding of low-level cloud occur during other months of the year? Are dust aerosols also present at the altitude of the cloud and if so, are they acting as cloud condensation nuclei? How closely does the ORAC retrieval replicate aerosol optical depth observations during the DODO campaign and can we use this as ‘truth’ to test the retrieval? Does the bias in retrieved radiance using the DODO and ORAC models vary with other changes in viewing geometry and is their any seasonal dependence? Can these discrepancies be quantified and accounted for in the retrieval?

The following paragraphs take some of these questions and outline three future research projects that would make a valuable contribution to increasing our quantitative understanding of aerosols and aerosol processes. To address the question of what other aerosol processes are important in determining cloud microphysical properties in regions of biomass burning outflow across the Atlantic, I would propose using detailed observations of aerosol and cloud properties from the SEVIRI satellite instrument which provides data at a much finer temporal resolution in this region than ATSR-2. AOD and Angström exponent data from the ORAC retrieval could be coupled with EUMETSAT retrievals of cloud properties including cloud top height, cloud effective radius and cloud fraction in a similar approach to the one used to study the semi-direct effects of Saharan dust. ECMWF reanalysis could be used in combination with these data to quantify the feedbacks between aerosol, cloud and local meteorology. Back trajectories coupled with ATSR firecounts would also be beneficial to trace aerosol origin and age, and cloud evolution. A synthesis of the available data in this region from different data sources would provide a more comprehensive understanding of aerosol-cloud interactions.

Dust aerosol is predominantly hydrophobic and does not readily act as cloud condensation nuclei unless it obtains a hydrophilic coating but can still exert semi-direct radiative forcing. This is poorly understood and needs further research to be quantified for inclusion in global models. The Saharan dust plume across the Atlantic is extensive during summer months, and its interaction with low-level marine stratocumulus is potentially a significant component of the aerosol radiative budget. Synthesis of data from other satellite instruments with the data gathered from SEVIRI and the UGAMP back trajectories in chapter 4 could provide valuable insights into aerosol-cloud interaction in this region. The Cloud-Aerosol Lidar Infrared Pathfinder Satellite Observation (CALIPSO) could provide more detailed data on aerosol altitude in relation to cloud which could only be inferred using back trajectory method employed in chapter 4. The Multi-angle Imaging SpectroRadiometer (MISR) could also be used to determine further aerosol properties including aerosol composition and size. The data domain could also be extended across the Atlantic to approximately 60° W to study the changes in aerosol-cloud interactions as a function of dust aerosol age.

The ORAC retrieval, as with other aerosol retrievals, is dependent on both the assumed aerosol type and aerosol model characteristics. Aerosol chemical composition, size distribution and refractive index are source dependent. At present, the aerosol models used in the ORAC retrieval are based on data from the OPAC model [Hess et al., 1998]. Aerosol properties have been measured in a number of flight campaigns in different regions of the globe [Singh et al., 2006; Rauber et al., 2007; Lu et al., 2007; Johnson et al., 2008] and from these it may be possible to construct regional aerosol models for use in the retrieval. Further development of the radiative transfer code is also necessary to enable it to simulate radiance in regions where two aerosol layers of different types exist. In conjunction with this it would be interesting to assess the sensitivity of the Angström exponent retrieved as part of the ORAC retrieval to aerosol vertical distribution. The Angström exponent is derived through the ratio of AOD at 0.6 and 0.8 μm. Although at 0.55 μm I find that the aerosol vertical distribution is unimportant in determining retrieved AOD, in the 0.8 μm channel it may be sensitive to the distribution of aerosol in relation to water vapour within the boundary layer, which may affect the Angström exponent calculation.

This work has made an important contribution to the field of aerosol science in testing the sensitivity of satellite retrievals now widely used in aerosol process studies, to assumed aerosol properties. These sensitivities need to be acknowledged in aerosol-process studies using these data. It has also emphasised the need to study aerosol-cloud interaction on a regional scale, highlighting regions of biomass burning and Saharan dust outflow from the African continent as regimes in which we do not fully understand the aerosol-cloud processes, and in which we cannot use current parameterisations to characterise aerosol forcing. Further research is necessary to quantify aerosol forcing in these regions.

Bibliography

A. S. Ackerman, O. B. Toon, D. E. Stevens, A. J. Heymsfield, V. Ramanathan, and E. J. Welton. Reduction of Tropical Cloudiness by Soot. *Science*, 288(5468):1042–1047, 2000a.

A. S. Ackerman, O. B. Toon, J. P. Taylor, D. W. Johnson, P. V. Hobbs, and R. J. Ferek. Effects of Aerosols on Cloud Albedo: Evaluation of Twomey's Parameterization of Cloud Susceptibility using Measurements of Ship Tracks. *Journal of the Atmospheric Sciences*, 57(16):2684–2695, 2000b.

A. S. Ackerman, M. P. Kirkpatrick, D. E. Stevens, and O. B. Toon. The impact of humidity above stratiform clouds on indirect aerosol climate forcing. *Nature*, 432(23):1014 – 1017, 2004.

B. A. Albrecht. Aerosols, Cloud Microphysics, and Fractional Cloudiness. *Science*, 245:1227–1230, 1989.

B. A. Albrecht, C. S. Bretherton, D. Johnson, W. H. Scubert, and A. S. Frisch. The Atlantic Stratocumulus Transition EXperiment (ASTEX). *Bulletin of the American Meteorological Society*, 76(6):889–904, 1995a.

B. A. Albrecht, M. P. Jensen, and W. J. Syrett. Marine boundary layer structure and fractional cloudiness. *Journal of Geophysical Research Atmospheres*, 100(D7):14,209–14,222, 1995b.

M. O. Andreae, C. D. Jones, and P. M. Cox. Strong present-day aerosol cooling implies a hot future. *Nature*, 435, 2005. doi:10.1038/nature03671.

A. Ansmann, J. Bösenberg, A. Chaikovsky, A. Comerón, S. Eckhardt, R. Eixmann, V. Freudenthaler, P. Ginoux, L. Komguem, H. Linné, M. A. L. Márquez, V. Matthias, I. Mattis, V. Mitev, D. Müller, S. Music, S. Nickovic, J. Pelon, L. Sauvage, P. Sobolewsky, M. K. Srivastava, A. Stohl, O. Torres, G. Vaughan, U. Wandinger, and M. Wiegner. Long-range transport of Saharan dust to northern Europe: The 11-16 October 2001 outbreak observed with EARLINET. *Journal of Geophysical Research Atmospheres*, 108(D24):4783, 2003.

L. Avey, T. J. Garrett, and A. Stohl. Evaluation of the aerosol indirect effect using satellite, tracer transport model, and aircraft data from the International Consortium for Atmospheric Research on Transport and Transformation. *Journal of Geophysical Research Atmospheres*, 112, 2007. D10S33, doi:10.1029/2006JD007581.

A. Birks. Improvements to the AATSR IPF relating to Land Surface Temperature Retrieval and Cloud Clearing over Land. Technical report, Rutherford Appleton Laboratory, Chilten, Didcot, Oxfordshire, U.K., 2007.

O. Boucher. Air traffic may increase cirrus cloudiness. *Nature*, 397:30–31, 1999.

O. Boucher, J. Haigh, D. Hauglustaine, J. Haywood, G. Myhre, T. Nakajima, G. Y. Shi, and S. Solomon. *Radiative Forcing of Climate Change, Section: 6.7.5, in Climate Change 2001: The Scientific Basis. Contribution of Working Group I to the Third Assessment Report of the Intergovernmental Panel on Climate Change*. Cambridge University Press, 2001.

E. Brankov, S. Trivikrama Rao, and P. S. Porter. A Trajectory-Clustering-Correlation Methodology for Examining the Long-Range Transport of Air Pollutants. *Atmospheric Environment*, 32(9): 1525–1534, 1998.

F. M. Bréon, D. Tanré, and S. Generoso. Aerosol Effect on Cloud Droplet Size Monitored from Satellite. *Science*, 295(5556):834–838, 2002.

V. Brovkin, V. Petoukhov, M. Claussen, E. Bauer, D. Archer, and C. Jaeger. Geoengineering climate by stratospheric sulfur injections: Earth system vulnerability to technological failure. *Climatic Change*, 92(3-4):243–259, 2009.

C. E. Bulgin, P. I. Palmer, G. E. Thomas, C. P. G. Arnold, E. Campmany, E. Carboni, R. G. Grainger, C. Poulsen, R. Siddans, and B. N. Lawrence. Regional and seasonal variations of the Twomey indirect effect as observed by the ATSR-2 satellite instrument. *Geophysical Research Letters*, 35, 2008. L02811,doi:10.1029/2007GL031394.

C. E. Bulgin, P. I. Palmer, C. J. Merchant, R. Siddans, S. Gonzi, C. A. Poulsen, G. E. Thomas, A. M. Sayer, E. Carboni, R. G. Grainger, E. J. Highwood, and C. L. Ryder. Quantifying the sensitivity of aerosol optical depths retrieved from msg-seviri to a priori data. *Journal of Geophysical Research Atmospheres*, 2010. Accepted for Publication.

P. R. Buseck and M. Pósfai. Airborne minerals and related aerosol particles: Effects on climate and the environment. *Proceedings of the National Academy of Science*, 96:3372–3379, 1999.

R. J. Charlson, J. E. Lovelock, M. O. Andreae, and S. G. Warren. Oceanic phytoplankton, atmospheric sulphur , cloud albedo and climate. *Nature*, 326:655–661, 1987.

S. A. Christopher and T. Jones. Satellite-based assessment of cloud-free net radiative effect of dust aerosols over the Atlantic Ocean. *Geophysical Research Letters*, 34, 2007. L02810, doi:10.1029/2006GL027783.

S. A. Christopher, B. Johnson, T. A. Jones, and J. Haywood. Vertical and spatial distribution of dust from aircraft and satellite measurements during the GERBILS field campaign. *Geophysical Research Letters*, 36, 2009. L06806, doi:10.1029/2008GL037033.

S. H. Chung and J. H. Seinfeld. Global distribution and climate forcing of carbonaceous aerosols. *Journal of Geophysical Research Atmospheres*, 107(D19):4407, 2002. doi:10.1029/2001JD001397.

M. Collaud Coen, E. Weingartner, D. Schaub, C. Hueglin, C. Corrigan, S. Henning, M. Schwikowski, and U. Baltensperger. Saharan dust events at the Jungfraujoch: Detection by wavelength dependence of single scattering albedo and first climatology analysis. *Atmospheric Chemistry and Physics*, 4:2465–2480, 2004.

P. J. Crutzen. Albedo enhancement by stratospheric sulfur injections: A contribution to resolve a policy dilemma? *Climatic Change*, 77(3-4):211–220, 2006. Editorial essay.

D. Diner, W. A. Abdou, H. R. Gordon, R. A. Kahn, Y. Knyazikhin, J. V. Martonchik, D. McDonald, S. McMuldroch, R. Myneni, and R. A. West. Level 2 Ancillary Products and Datasets Algorithm Theoretical Basis, 1999.

D. J. Diner, W. A. Abdou, T. P. Ackerman, K. Crean, H. R. Gordon, R. A. Kahn, J. V. Martonchik, S. McMuldroch, S. R. Paradise, B. Pinty, M. M. Verstraete, M. Wang, and R. A. West. Level 2 Aerosol Retrieval Algorithm Theoretical Basis, 2008.

M. Doyle and S. Dorling. Visibility trends in the UK 1950-1997. *Atmospheric Environment*, 36 (19):3161–3172, 2002.

R. R. Draxler and G. D. Rolph. HYSPLIT (HYbrid Single-Particle Lagrangian Integrated Trajectory model, 2010. http://ready.arl.noaa.gov/HYSPLIT.php.

O. Dubovik, B. Holben, T. F. Eck, A. Smirnov, Y. J. Kaufman, M. D. King, D. Tanre, and I. Slutsker. Variability of absorption and optical properties of key aerosol types observed in worldwide locations. *Journal of the Atmospheric Sciences*, 59(3):590–608, 2002.

A. J. Durant, S. P. Harrison, I. M. Watson, and Y. Balkanski. Sensitivity of direct radiative forcing by mineral dust to particle characteristics. *Progress in Physical Geography*, 33(1):80–102, 2009.

U. Dusek, G. P. Frank, L. Hildebrandt, J. Curtius, J. Schneider, S. Walter, D. Chand, F. Drewnick, S. Hings, D. Jung, S. Borrmann, and M. O. Andreae. Size Matters More Than Chemistry for Cloud-Nucleating Ability of Aerosol Particles. *Science*, 312:1375–1378, 2006.

S. Engelstaedter and R. Washington. Atmospheric controls on the annual cycle of North African Dust. *Journal of Geophysical Research Atmospheres*, 112, 2007. D03103, doi:10.1029/2006JD007195.

S. Engelstaedter, I. Tegen, and R. Washington. North African dust emissions and transport. *Earth Science Reviews*, 79(1-2):73–100, 2006.

ESA. ATSR World Fire Atlas, 2004. http://dup.esrin.esa.it/ionia/wfa/index.asp.

EUMETSAT. Cloud Detection for MSG - Algorithm Theoretical Basis Document. Technical report, EUMETSAT, Am Kavalleriesand 31, D-64295 Darmstadt, Germany, 2007. EUM/MET/REP/07/0132.

EUMETSAT. EUropean organisation for the exploitation of METeorological SATellites Unified Meteorological Archive and Retrieval Facility (U-MARF) online ordering, 2009. http://archive.eumetsat.int/umarf/.

G. Feingold, L. A. Remer, J. Ramaprasad, and Y. J. Kaufman. Analysis of smoke impact on clouds in Brazilian biomass burning regions: An extension of Twomey's approach. *Journal of Geophysical Research Atmospheres*, 106(D19):22,907–22,922, 2001.

G. Feingold, W. L. Eberhard, D. E. Veron, and M. Previdi. First measurements of the Twomey indirect effect using ground-based remote sensors. *Geophysical Research Letters*, 30(6):1287, 2003.

G. R. Foltz and M. J. McPhaden. Impact of Saharan dust on tropical North Atlantic SST. *Journal of Climate*, 21(19):5048 – 5060, 2008.

P. Formenti, W. Elbert, W. Maenhaut, J. Haywood, and M. O. Andreae. Chemical composition of mineral dust aerosol during the Saharan Dust Experiment (SHADE) airborne campaign in the Cape Verde region, September 2000. *Journal of Geophysical Research Atmospheres*, 108 (D18):8576–8592, 2003.

P. Forster, V. Ramaswarmy, P. Artaxo, T. Berntsen, R. Betts, D. W. Fahey, J. Haywood, J. Lean, D. C. Lowe, G. Myhre, J. Nganga, R. Prinn, G. Raga, M. Schluz, and R. Van Dorland. *Changes in Atmospheric Constituents and in Radiative Forcing in: Climate Change 2007: The Physical Science Basis. Contribution of Working Group I to the Fourth Assessment Report of the Intergovernmental Panel on Climate Change*. Cambridge University Press, 2007.

S. Fuzzi, M. O. Andreae, B. J. Huebert, M. Kulmala, T. C. Bond, M. Boy, S. J. Doherty, A. Guenther, M. Kanakidou, K. Kawamura, V. M. Kerminen, U. Lohmann, L. M. Russell, and U. Pöschl. Critical assessment of the current state of scientific knowledge, terminology, and research needs concerning the role of organic aerosols in the atmosphere, climate, and global change. *Atmospheric Chemistry and Physics*, 6:2017 – 2038, 2006.

D. M. Giles and B. N. Holben. AERONET Data Display Interface, 2010. http://aeronet.gsfc.nasa.gov/cgi-bin/type_piece_of_map_opera_v2_new?level=3.

S. L. Gong, L. A. Barrie, and M. Lazare. Canadian Aerosol Module (CAM): A size-segregated simulation of atmospheric aerosol processes for climate and air quality models 2. Global sea-salt aerosol and its budgets. *Journal of Geophysical Research Atmospheres*, 107(D24):4779, 2002.

A. S. Goudie and N. J. Middleton. Saharan dust storms: nature and consequences. *Earth Science Reviews*, 56:179–204, 2001.

M. Hallquist, J. C. Wenger, U. Baltensperger, Y. Rudich, D. Simpson, M. Claeys, J. Dommen,

N. M. Donahue, C. George, A. H. Goldstein, J. F. Hamilton, H. Herrmann, T. Hoffmann, Y. Iinuma, M. Jang, M. E. Jenkin, J. L. Jimenez, A. Kiendler-Scharr, W. Maenhaut, G. McFiggans, Th. F. Mentel, A. Monod, A. S. H. Prévot, J. H. Seinfeld, J. D. Surratt, R. Szmigielski, and J. Wildt. The formation, properties and impact of secondary organic aerosol: current and emerging issues. *Atmospheric Chemistry and Physics*, 9:5155 – 5236, 2009.

Q. Han, W. B. Rossow, J. Chou, and R. M. Welch. Global Survey of the Relationships of Cloud Albedo and Liquid Water Path with Droplet Size using ISCCP. *Journal of Climate*, 11:1516–1528, 1998.

J. Haywood and O. Boucher. Estimates of the Direct and Indirect Radiative Forcing Due to Tropospheric Aerosols: A Review. *Reviews of Geophysics*, 38(4):513–543, 2000.

M. Hess, P. Koepke, and I. Schult. Optical Properties of Aerosols and Clouds: The Software Package OPAC. *Bulletin of the American Meteorological Society*, 79(5):831–844, 1998.

B. N. Holben, T. F. Eck, I. Slutsker, D. Tanre, J. P. Buis, A. Setzer, E. Vermote, J. A. Reagan, Y. Kaufman, T. Nakajima, F. Lavenu, I. Jankowiak, and A. Smirnov. AERONET - A federated instrument network and data archive for aerosol characterization. *Remote Sensing of Environment*, 66:1–16, 1998.

H. Horvath. Atmospheric visibility. *Atmospheric Environment*, 15(10/11):1785–1796, 1981.

J. Huang, B. Lin, P. Minnis, T. Wang, X. Wang, Y. Hu, Y. Yi, and J. Kirk Ayers. Satellite-based assessment of possible dust aerosols semi-direct effect on cloud water path over East Asia. *Geophysical Research Letters*, 33, 2006. L19802, doi:10.1029/2006GL026561.

J. Huang, C. Zhang, and J. M. Prospero. Large-scale effect of aerosols on precipitation in the West African Monsoon region. *Quarterly Journal of the Royal Meteorological Society*, 135 (164):581–594, 2009.

J. G. Hudson. Variability of the relationship between particle size and cloud-nucleating ability. *Geophysical Research Letters*, 34, 2007. L08801, doi:10.1029/2006GL028850.

M. Z. Jacobson. *Fundamentals of Atmospheric Modelling*. Cambridge University Press, 2005. Second Edition.

B. T. Johnson, K. P. Shine, and P. M. Forster. The semi-direct aerosol effect: Impact of absorbing aerosols on marine stratocumulus. *Quarterly Journal Royal Meteorological Society*, 130:1407 – 1422, 2004.

B. T. Johnson, S. R. Osborne, J. M. Haywood, and M. A. J. Harrison. Aircraft measurements of biomass burning aerosol over West Africa during DABEX. *Journal of Geophysical Research Atmospheres*, 113, 2008. D00C06, doi:10.1029/2007JD009451.

Y. J. Kaufman and R. S Fraser. The Effect of Smoke Particles on Clouds and Climate Forcing. *Science*, 277:1636–1639, 1997.

A. Keil and J. M. Haywood. Solar radiative forcing by biomass burning aerosol particles during SAFARI 2000: A case study based on measured aerosol and cloud properties. *Journal of Geophysical Research Atmospheres*, 108(D13):8467, 2003.

D. W. Keith. Geoengineering the climate: History and prospect. *Annual Review of Energy and the Environment*, 25:245–284, 2000.

J. T. Kiehl and H. Rodhe. *Aerosol Forcing of Climate: Modeling geographical and seasonal forcing due to aerosols*. Wiley, New York, 1995.

S-W. Kim, S-C. Yoon, J. Kim, and S-Y. Kim. Seasonal and monthly variations of columnar aerosol optical properties over east Asia determined from multi-year MODIS, LIDAR, and AERONET Sun/sky radiometer measurements. *Atmospheric Environment*, 4(8):1634–1651, 2007.

S. A. Klein and D. L. Hartmann. The seasonal cycle of low stratiform clouds. *Journal of Climate*, 6:1587–1606, 1993.

A. A. Kokhanovsky, F-M. Bréon, A. Cacciari, E. Carboni, D. Diner, W. Di Nicolantonio, R. G. Grainger, W. M. F. Grey, R. Höller, K-H. Lee, Z. Li, P. J. R. North, A. Sayer, G. Thomas, and W. Hoyningen-Huene. Aerosol remote sensing over land: A comparison of satellite retrievals using different algorithms and instruments. *Atmospheric Research*, 85(3-4):372–394, 2007.

A. A. Kokhanovsky, J. L. Deuzé, D. J. Diner, O. Dubovik, F. Ducos, C. Emde, M. J. Garay, R. G. Grainger, A. Heckel, M. Herman, I. L. Katsev, J. Keller, R. Levy, P. R. J. North, A. S. Prikhach, V. V. Rozanov, A. M. Sayer, Y. Ota, D. Tanré, G. E. Thomas, and E. P. Zege. The inter-comparison of major satellite aerosol retrieval algorithms using simulated intensity and

polarization characteristics of reflected light. *Atmospheric Measurement Techniques*, 3:909–932, 2010.

I. Koren, L. A. Remer, Y. J. Kaufman, Y. Rudich, and J. V. Martins. On the twilight zone between clouds and aerosols. *Geophysical Research Letters*, 34, 2007. L08805, doi:10.1029/2007GL02953.

J. Latham, P. Rasch, C-C. Chen, L. Kettles, A. Gadian, A. Gettelman, H. Morrison, K. Bower, and T. Choularton. Global temperature stabilization via controlled albedo enhancement of low-level maritime clouds. *Philosophical Transactions of the Royal Society A*, 366:3969 – 3987, 2008.

P. Le Sager, B. Yantosca, and C. Carouge. GEOS-Chem v8-02-01 Online User's Guide, 2008. http://acmg.seas.harvard.edu/geos/doc/man/.

T. M. Lenton, H. Held, E. Kriegler, J. W. Hall, W. Lucht, S. Rahmstorf, and H. J. Schellnhuber. Tipping elements in the Earth's climate system. *Proceedings of the National Academy of Sciences*, 105(6):1786–1793, 2008.

G. Lesins, P. Chylek, and U. Lohmann. A study of internal and external mixing scenarios and its effect on aerosol optical properties and direct radiative forcing. *Journal of Geophysical Research Atmospheres*, 107(D10), 2002. 10.1029/2001JD000973.

H. Liao and J. H. Seinfeld. Radiative forcing by mineral dust aerosols: sensitivity to key variables. *Journal of Geophysical Research*, 103(D24):31,637–31,645, 1998.

H. Liao, P. J. Adams, S. H. Chung, J. H. Seinfeld, L. J. Mickley, and D. J. Jacob. Interactions between tropospheric chemistry and aerosols in a unified general circulation model. *Journal of Geophysical Research Atmospheres*, 108(D1):4001, 2003. doi:10.1029/2001JD001260.

C. Liousse, J. E. Penner, C Chuang, J. J. Walton, H. Eddleman, and H. Cachier. A global three-dimensional model study of carbonaceous aerosols. *Journal of Geophysical Research Atmospheres*, 101(D14):19,411 – 19,432, 1996.

D. Liu, Z. Wang, Z. Liu, D. Winker, and C. Trepte. A height resolved global view of dust aerosols from the first year CALIPSO lidar measurements. *Journal of Geophysical Research Atmospheres*, 113, 2008a. D16214, doi:10.1029/2007JD009776.

Y. Liu and P. H. Daum. Anthropogenic aerosols: Indirect warming effect from dispersion forcing. *Nature*, 419:580–581, 2002.

Z. Liu, A. Omar, M. Vaughan, J. Hair, C. Kittaka, Y. Hu, K. Powell, C. Trepte, D. Winker, C. Hostetler, R. Ferrare, and R. Pierce. CALIPSO lidar observations of the optical properties of Saharan dust: A case study of long-range transport. *Journal of Geophysical Research Atmospheres*, 113, 2008b. D07207, doi:10.1029/2007JD008878.

U. Lohmann and J. Feichter. Global indirect aerosol effects: A review. *Atmospheric Chemistry and Physics*, 5:715–737, 2005.

J. P. Lopez, M. Luo, L. E. Christensen, M. Loewenstein, H. Jost, C. R. Webster, and G. Osterman. TES Carbon Monoxide validation during two AVE campaigns using the Argus and ALIAS instruments on NASA's WB-57F. *Journal of Geophysical Research Atmopsheres*, 113, 2008. doi:10.1029/2007JD008811, D16547.

M-L. Lu, W. C. Conant, H. H. Jonsson, V. Varutbangkul, R. C. Flagan, and J. H. Seinfeld. The Marine Stratus/Stratocumulus Experiment (MASE): Aerosol-cloud relationships in marine stratocumulus. *Journal of Geophysical Research Atmospheres*, 112, 2007. D10209, doi:10.1029/2006JD007985.

H.-J. Lutz. Cloud Processing for METEOSAT Second Generation Technical Memorandum no. 4. Technical report, EUMETSAT, 1999a.

H-J. Lutz. Cloud processing for METEOSAT Second Generation. Technical report, EUMETSAT, AM Kavelleriesand 31, D-64295 Darmstadt, Germany, 1999b.

M. Mallet, P. Tulet, D. Serça, F. Solmon, O. Dubovik, J. Pelon, V. Pont, and O. Thouron. Impact of dust aerosols on the radiative budget, surface heat fluxes, heating rate profiles and convective activity over West Africa during March 2006. *Atmospheric Chemistry and Physics*, 9:7143–7160, 2009.

S. H. Marsh, S. M. Dean, R. G. Grainger, A. L. Quijano, G. E. Thomas, and B. N. Lawrence. An Optimal Estimation Aerosol Retrieval Scheme for ATSR-2. Technical report, Atmospheric, Oceanic and Planetary Physics, Department of Physics, University of Oxford, 2004. AOPP Memorandum 2004.2.

J. V. Martonchick, D. J. Diner, K. A. Crean, and M. A. Bull. Regional Aerosol Retrieval Results From MISR. *IEEE Transactions on Geoscience and Remote Sensing*, 40(7):1520–1531, 2002.

C. L. McConnell, E. J. Highwood, H. Coe, P. Formenti, B. Anderson, S. Osborne, S. Nava, K. Desboeufs, G. Chen, and M. A. J. Harrison. Seasonal variations of the physical and optical characteristics of Saharan dust: Results from the Dust Outflow and Deposition to the Ocean (DODO) experiment. *Journal of Geophysical Research Atmospheres*, 113, 2008. D14S05, doi:10.1029/2007JD009606.

C. L. McConnell, P. Formenti, E. J. Highwood, and M. A. J. Harrison. Using aircraft measurements to determine the refractive index of Saharan dust during the DODO Experiments. *Atmospheric Chemistry and Physics*, 10:1–18, 2010.

M. P. McCormick, L. W. Thomason, and C. R. Trepte. Atmospheric effects of the Mt Pinatubo eruption. *Nature*, 373:399 – 404, 1995.

I. G. McKendry, K. B. Strawbridge, N. T. O'Neill, A. M. Macdonald, P. S. K. Liu, K. G. Leaitch, K. G. Anlauf, L. Jaegle, T. D. Fairlie, and D. L. Westphal. Trans-Pacific transport of Saharan dust to western North America: A case study. *Journal of Geophysical Research Atmospheres*, 112, 2007. D01103, doi:10.1029/2006JD007129.

C. J. Merchant. Saharan dust and SST bias: A dust index for daytime SEVIRI imagery. Technical report, University of Edinburgh, Edinburgh, UK, 2006. OSI-SAF Associated/Visiting Scientist Project Report.

C. J. Merchant, O. Embury, P. Le Borgne, and B. Bellec. Saharan dust in nighttime thermal imagery: Detection and reduction of related biases in retrieved sea surface temperature. *Remote Sensing of Environment*, 104(1):15–30, 2006.

J. Methven. Offline trajectory package. Technical report, University of Reading, Department of Meteorology, University of Reading, PO Box 243, Earley Gate, Reading, RG6 6BB, 1997.

M. Mills, C. Ridame, M. Davey, J. La Roche, and R. J. Geider. Iron and phosphorus co-limit nitrogen fixation in the eastern tropical north atlantic. *Nature*, 429:292–294, 2004.

C. Mutlow, J. Murray, P. Bailey, A. Birks, and D. Smith. Atsr 1/2 user guide issue 1.0. Technical report, European Space Agency, 1999.

G. Myhre. Consistency between Satellited-Derived and Modelled Estimates of the Direct Aerosol Effect. *Science*, 375:187–190, 2009.

T. Nakajima, A. Higurashi, K. Kawamoto, and J. E. Penner. A possible correlation between satellite-derived cloud and aerosol microphysical parameters. *Geophysical Research Letters*, 28(7):1171–1174, 2001.

NASA. AERONET system description, 2007. http://aeronet.gsfc.nasa.gov/new_web/system_descriptions_oper

NASA. AERONET data - Version 2 AOD descriptions, AERONET inversion products, 2008. http://aeronet.gsfc.nasa.gov/new_web/data_description_AOD_V2.html, http://aeronet.gsfc.nasa.gov/new_web/Documents/Inversion_productions_V2.pdf.

NASA. Aerosol robotic network mission, 2009. http://aeronet.nasa.gov/.

NASA. Aerosol robotic network site information map interface, 2010. http://aeronet.nasa.gov/cgi-bin/site_info.

NOAA. NCEP reanalysis electronic atlas, 2007. http://www.cdc.noaa.gov/ncep_reanalysis/.

S. R. Osborne, B. T. Johnson, J. M. Haywood, A. J. Baran, M. A. J. Harrison, and C. L. McConnell. Physical and optical properties of mineral dust aerosol during the Dust and Biomass-burning experiment. *Journal of Geophysical Research Atmospheres*, 113, 2007. D00C03,doi:10.1029/2007JD009551.

S. Otto, E. Bierwirth, B. Weinzierl, K. Kandler, M. Esselborn, M. Tesche, A. Schladitz, M. Wendisch, and T. Trautmann. Solar radiative effects of a Saharan dust plume observed during SAMUM assuming spheroidal model particles. *Tellus Series B Chemical and Physical Meteorology*, 61B:270–296, 2009.

I. R. Paluch and D. H. Lenschow. Stratiform Cloud Formation in the Marine Boundary Layer. *Journal of the Atmospheric Sciences*, 48(19):2141–2158, 1991.

D. E. Parker, H. Wilson, P. D. Jones, J. R. Christy, and C. K. Folland. The impact of mount pinatubo on world-wide temperatures. *International Journal of Climatology*, 16:487–497, 1996.

J. Perlwitz and R. L. Miller. Cloud cover increase with increasing aerosol absorptivity: A counterexample to the conventional semidirect aerosol effect. *Journal of Geophysical Research Atmospheres*, 115, 2010. D08203, doi:10.1029/2009JD012637.

P. Pilewskie. Aerosols heat up. *Nature*, 448:541–542, 2007.

C. A. Pope III and D. W. Dockery. Health Effects of Fine Particulate Air Pollution: Lines that Connect. *Air and Waste Management Association*, 56:709–742, 2006.

C. Poulsen and P. Watts. Retrieval and validation of cloud properties using ATSR-2 data. Technical report, Rutherford Appleton Laboratory, 2002. EUMETSAT Meteorological Satellite Conference.

C. A. Poulsen, R. Siddans, G. E. Thomas, A. Sayer, R. G. Grainger, O. Perez-Navarro, O. Portela-Arjona, and P.-Y. Deschamps. ESA GlobAerosol: Final Validation and Intercomparison Report Version 3.2. Technical report, ESA, 2009.

J. Quaas, O. Boucher, and F. M. Breon. Aerosol indirect effects in POLDER satellite data and the Laboratoire de Météorologie Dynamique-Zoom (LMDZ) general circulation model. *Journal of Geophysical Research Atmospheres*, 109, 2004. D08205, doi:10.1029/2003JD004317.

J. Quaas, O. Boucher, N. Bellouin, and S. Kinne. Satellite-based estimate of the direct and indirect aerosol climate forcing. *Journal of Geophysical Research Atmospheres*, 113, 2008. D05204, doi:10.1029/2007JD008962.

P. K. Quinn and T. S. Bates. North American, Asian, and Indian haze: Similar regional impacts on climate? *Geophysical Research Letters*, 30(11):1555, 2003.

J. L. Rajot, P. Formenti, S. Alfaro, K. Desboeufs, S. Chevaillier, B. Chatenet, A. Gaudichet, E. Journet, B. Marticorena, S. Triquet, A. Maman, N. Mouget, and A. Zakou. AMMA dust experiment: An overview of measurements performed during the dry season special observation period (SOP0) at the Banizoumbou (Niger) supersite. *Journal of Geophysical Research Atmospheres*, 113, 2008. D00C14, doi:10.1029/2008JD009906.

J. T. Randerson, G. R. Van der Werf, Giglio. L., G. J. Collatz, and S Kasibhatla. P. Global Fire Emissions Database version 2, dataset, 2007. available online at: [http://daac.ornl.gov/].

R. M. Rauber, B. Stevens, H. T. Ochs III, C. Knight, B. A. Albrecht, A. M. Blyth, C. W. Fairall, J. B. Jensen, S. G. Lasher-Trapp, O. L. Mayol-Bracero, G. Vali, J. R. Anderson, B. A. Baker, A. R. Bandy, E. Burnet, J. L. Brenguier, W. A. Brewer, P. R. A. Brown, P. Chuang, W. R. Cotton, L. Di Girolamo, B. Geerts, H. Gerber, S. Goke, L. Gomes, B. G. Heikes, J. G. Hudson,

P. Kollias, R. P. Lawson, S. K. Krueger, D. H. Lenschow, L. Nuijens, D. W. O'Sullivan, R. A. Rilling, D. C. Rogers, A. P. Siebesma, E. Snodgrass, J. L. Stith, D. C. Thornton, S. Tucker, C. H. Twohy, and P. Zuidema. Rain in Shallow Cumulus over the Ocean: The RICO Campaign. *Bulletin of the American Meteorological Society*, 88(12):1912–1928, 2007.

D. Raynaud, J. Jouzel, J. M. Barnola, J. Chappellaz, R. J. Delmas, and C. Lorius. The ice record of greenhouse gases. *Science*, 259(5097):926–934, 1993.

L. A. Remer, D. Tanré, and Y. Kaufman. Algorithm for remote sensing of tropospheric aerosol from MODIS, 2006. Algorithm Theoretical Basis Document.

C. D. Rodgers. *Inverse Methods for Atmospheric Sounding: Theory and Practice*. World Scientific Publishing Co. Pte. Ltd., 57 Shelton Street, Covent Garden, London, WC2H 9HE, 2000. Series on Atmospheric Oceanic and Planetary Physics - Vol. 2.

S. Salter, G. Sortino, and J. Latham. Sea-going hardware for the cloud albedo method of reversing global warming. *Philosophical Transactions of the Royal Society A*, 366:3989 – 4006, 2008.

J. Schmetz, P. Pili, S. Tjemkes, D. Just, J. Kerkmann, S. Rota, and A. Ratier. An Introduction to Meteosat Second Generation (MSG). *Bulletin of the American Meteorological Society*, 83(7): 977–992, 2002.

F. Schröder, B. Kärcher, C. Duroure, J. Ström, A. Petzold, J-F. Gayet, B. Strauss, P. Wendling, and S. Borrmann. On the Transition of Contrails into Cirrus Clouds. *Journal of the Atmospheric Sciences*, 57(4):464–480, 2000.

A. Seaton, W. MacNee, K. Donaldson, and D. Godden. Particulate air pollution and acute health effects. *The Lancet*, 345:176–178, 1995.

J. H. Seinfeld and S. N. Pandis. *Atmospheric Chemistry and Physics: From Air Pollution to Climate Change*. John Wiley & Sons, Inc., United States of America, 1998.

J. H. Seinfeld and S. N. Pandis. *Atmospheric Chemistry and Physics: From Air Pollution to Climate Change*. John Wiley & Sons Inc., Hoboken, New Jersey, Second edition, 2006.

J. Shepherd. Geoengineering the climate: Science, governance and uncertainty. Technical report, The Royal Society, 2009.

H. B. Singh, W. H. Brune, J. H. Crawford, D. J. Jacob, and P. B. Russell. Overview of the summer 2004 Intercontinental Chemical Transport Experiment - North America (INTEX-A). *Journal of Geophysical Research Atmospheres*, 111, 2006. D24S01, doi:10.1029/2006JD007905.

P. Sinha, P. V. Hobbs, R. J. Yokelson, D. R. Blake, S. Gao, and T. W. Kirchstetter. Distributions of trace gases and aerosols during the dry biomass burning season in southern Africa. *Journal of Geophysical Research Atmospheres*, 108(D17):4536, 2003.

A. Smirnov, B. N. Holben, I. Slutsker, D. M. Giles, C. R. McClain, T. F. Eck, S. M. Sakerin, A. Macke, P. Croot, G. Zibordi, P. K. Quinn, J. Sciare, S. Kinne, M. Harvey, T. J. Smyth, S. Piketh, T. Zielinski, A. Proshutinksy, J. I. Goes, N. B. Nelson, P. Larouche, V. F. Radionov, P. Goloub, K. Krishna Moorthy, R. Matarrese, E. J. Robertson, and F. Jourdin. Maritime Aerosol Network as a component of Aerosol Robotic Network. *Journal of Geophysical Research Atmospheres*, 114, 2009. D06204, doi:10.1029/2008JD011257.

K. Stammes, S-C. Tsay, W. Wiscombe, and K. Jayaweer. Numerically stable algorithm for discrete-ordinate-method radiative transfer in multiple scattering and emitting layed media. *Applied Optics*, 27(12):2502–2509, 1988.

B. Stevens and G. Feingold. Untangling aerosol effects on clouds and precipitation in a buffered system. *Nature*, 461:607–613, 2009. doi:10.1038/nature08281.

L. L. Stowe, R. M. Carey, and P. P. Pellegrino. Monitoring the Mt. Pinatubo aerosol layer with NOAA/11 AVHRR data. *Geophysical Research Letters*, 19(2):159 – 162, 1992.

J. Su, J. Huang, Q. Fu, P. Minnis, J. Ge, and J. Bi. Estimation of Asian dust aerosol effect on cloud radiation forcing using Fu-Liou radiative model and CERES measurements. *Atmospheric Chemistry and Physics*, 8:2763–2771, 2008.

T. Takemura, Y. J. Kaufman, L. A. Remer, and T. Nakajima. Two competing pathways of aerosol effects on cloud and precipitation formation. *Geophysical Research Letters*, 34, 2007. L04802, doi:10.1029/2006GL028349.

I. Tegen and I. Fung. Contribution to the atmospheric mineral aerosol load from land surface modification. *Journal of Geophysical Research Atmospheres*, 100(D9,18):707–726, 1995.

G. E. Thomas, S. M. Dean, E. Carboni, R. G. Grainger, C. A. Poulsen, R. Siddans, and B. J. Kerridge. Globaerosol data user element, 2005. Aerosol Extraction Algorithm Definition ATSR-2/AATSR Algorithm Theoretical Basis Document.

G. E. Thomas, S. H. Marsh, S. M. Dean, E. Carboni, R. G. Grainger, C. A. Poulsen, R. Siddans, and B. J. Kerridge. An Optimal Estimation Aerosol Retrieval Scheme for (A)ATSR. Technical report, Department of Atmospheric, Oceanic and Planetary Physics, University of Oxford, UK, 2007. AOPP Memorandum 2007.1.

G. E. Thomas, C. A. Poulsen, R. L. Curier, G. de Leeuw, H. Marsh, E. Carboni, R. G. Grainger, and R. Siddans. Comparison of AATSR and SEVIRI aerosol retrievals over the Northern Adriatic. *Quarterly Journal of the Royal Meteorological Society*, 133(S1):85–95, 2007a.

G. E. Thomas, E. Carboni, A. M. Sayer, C. A. Poulsen, R. Siddans, and R. G. Grainger. *Oxford-RAL Aerosol and Cloud (ORAC): Aerosol retrievals from satellite radiometers*. Springer, Berlin, 2009a.

G. E. Thomas, C. A. Poulsen, A. M. Sayer, S. H. Marsh, S. M. Dean, E. Carboni, R. Siddans, R. G. Grainger, and B. N. Lawrence. The GRAPE aerosol retrieval algorithm. *Atmospheric Measurement Techniques*, 2:679–701, 2009b.

K. E. Trenberth and J. T. Fasullo. Tracking Earth's Energy. *Science*, 328:316–317, 2010.

S. Twomey. Pollution and the planetary albedo. *Atmospheric Environment*, 8:1251–1256, 1974.

J. Wang, X. Liu, S. A. Christopher, J. S. Reid, E. Reid, and H. Maring. The effects of non-sphericity on geostationary satellite retrievals of dust aerosols. *Geophysical Research Letters*, 30(24):2293, 2003.

P. D. Watts, C. T. Mutlow, A. J. Baran, and A. M. Zavody. Study on cloud properties derived from meteosat second generation observations. Technical report, EUMETSAT, Darmstadt, Germany, 1998. Rep. 97/181, Prepared by the Rutherford Appleton Laboratory.

T. M. L. Wigley. Could reducing fossil-fuel emissions cause global warming? *Nature*, 349: 503–506, 1991.

T. M. L. Wigley. A Combined Mitigation/Geoengineering Approach to Climate Stabilization. *Science*, 314(5798):452–454, 2006.

R. Wood, C. S. Bretherton, and D. L. Hartmann. Diurnal cycle of liquid water path over the subtropical and tropical oceans. *Geophysical Research Letters*, 29(23):2092, 2002. doi:10.1029/2002GL015371.

E-S. Yang, P. Gupta, and S. A. Christopher. Net radiative effect of dust aerosols from satellite measurements over Sahara. *Geophysical Research Letters*, 36, 2009. L18812, doi:10.1029/2009GL039801.

C. S. Zender, H. Bian, and D. Newman. Mineral Dust Entrainment And Deposition (DEAD) model: Description and 1990's dust climatology. *Journal of Geophysical Research Atmospheres*, 108(D14):4416, 2003.

X. P. Zhao, I. Laszio, O. Dubovik, B. N. Holben, J. Sapper, D. Tanré, and C. Pietras. A study of the effect of non-spherical dust particles on the AVHRR aerosol optical thickness retrievals. *Geophysical Research Letters*, 30:1317–1321, 2003.